HZG REPORT 2011-1 // ISSN 2191-7833

Development of Hydrogen Storage Systems using Sodium Alanate

(Vom Promotionsausschuss der Technischen Universität Hamburg-Harburg im Jahr 2010 als Dissertation angenommene Arbeit)

G. A. Lozano Martinez

wissen
schafft
nutzen

Helmholtz-Zentrum
Geesthacht
Zentrum für Material- und Küstenforschung

HZG REPORT 2011-1

Development of Hydrogen Storage Systems using Sodium Alanate

(Vom Promotionsausschuss der Technischen Universität Hamburg-Harburg im Jahr 2010 als Dissertation angenommene Arbeit)

G. A. Lozano Martinez

Helmholtz-Zentrum Geesthacht
Zentrum für Material- und Küstenforschung GmbH | Geesthacht | 2011

Die HZG Reporte werden kostenlos abgegeben.
HZG Reports are available free of charge.

Anforderungen/Requests:

Helmholtz-Zentrum Geesthacht
Zentrum für Material- und Küstenforschung GmbH
Bibliothek/Library
Max-Planck-Straße 1
21502 Geesthacht
Germany
Fax.: +49 4152 87-1717

Druck: HZG-Hausdruckerei

Als Manuskript vervielfältigt.

ISSN 2191-7833

Helmholtz-Zentrum Geesthacht
Zentrum für Material- und Küstenforschung GmbH
Max-Planck-Straße 1
21502 Geesthacht
www.hzg.de

HZG REPORT 2011-1

Development of Hydrogen Storage Systems using Sodium Alanate

(Vom Promotionsausschuss der Technischen Universität Hamburg-Harburg im Jahr 2010 als Dissertation angenommene Arbeit)

Gustavo Adolfo Lozano Martinez

132 pages with 68 figures and 16 tables

Abstract

Hydrogen storage systems based on sodium alanate are studied, modelled, and optimised, on the basis of both experimental and theoretical approaches. The experimental hydrogen sorption behaviour (kinetics, heat transfer and cycling) of small cells up to kg-scale storage tanks is compared and analysed. In particular, the effect of the size of the system, powder compaction, and addition of expanded graphite on the sorption behaviour is investigated and characterized. In order to implement simulations and further evaluations, empirical kinetic models for both hydrogen absorption and desorption of sodium alanate material are developed. The hydrogen sorption process in a storage tank is modelled on the basis of the developed kinetic equations, hydrogen transport equations and heat transfer equations. A numerical simulation is developed and validated with the experimental results previously obtained in this work. Optimisation towards the gravimetric hydrogen storage capacity of a tubular storage tank based on sodium alanate is defined and performed by means of the numerical simulation and the experimental results of this work.

Entwicklung von Natriumalanat-basierten Wasserstoffspeichertanks

Zusammenfassung

Durch experimentelle und theoretische Methoden wurden Natriumalanat-Wasserstoffspeichertanks untersucht, modelliert und optimiert. Das experimentelle Sorptionsverhalten (Kinetik, Wärmeübertragung, Zyklierung) von kleinen Zellen bis hin zu Speichertanks im kg-Maßstab ist verglichen and analysiert worden. Hierbei wurde insbesondere der Einfluss der Größe des Systems, der Materialkompaktierung, und des Zusatzes von expandiertem Graphit auf das Sorptionsverhalten erforscht und charakterisiert. Zu weiteren Evaluierungen und Simulationen wurden empirische kinetische Modelle sowohl für Absorption als auch Desorption für den Fall von Natriumalanat als Speichermaterial entwickelt. Der Wasserstoffsorptionsprozess in Speichertanks wurde mit Hilfe der entwickelten kinetischen Gleichungen, Wasserstofftransport- und Wärmeübertragungsgleichungen modelliert. Eine numerische Simulation wurde entwickelt, und durch die gefundenen experimentellen Ergebnisse dieser Arbeit validiert.
Mit Hilfe der erzielten Ergebnisse und der Simulation wurde das Design eines auf Natriumalanat basierenden Wasserstoffspeichertanks in Bezug auf die gravimetrische Kapazität optimiert.

Manuscript received / Manuskripteingang in TFP: 19. Januar 2011

Acknowledgements

To all Professors, tutors and teachers, to my colleagues, my friends and all of my family, who both directly and indirectly inspired, shared and encouraged my desire to work in this doctoral thesis, to all and every one of you my grateful acknowledgement and sincere thanks.

I want to express my thanks to Prof. Rüdiger Bormann for his guidance and advice, for the constructive periodic discussions, from which I learned how to develop a deeper phenomenological perspective and how to separate objective observations from subjective points of view.

Especially I want to express my deep gratitude to Dr. Martin Dornheim for his friendly and direct supervision and his support during all my PhD work at the Department of Nanotechnology at the GKSS Research Centre (today Helmholtz-Zentrum Geesthacht). I want to thank him for believing in my ideas, my work and my character. Thanks for promoting that pleasant work atmosphere in the department, which has achieved amazing results as it will continue for sure.

I would like to thank as well Prof. Thomas Klassen not only for his role as reviewer and evaluator of my thesis but also for his former work and energy invested in the development of the department of Nanotechnology, encouraging the research from new scientists in the field of hydrogen technology.

For all the help and collaboration during my work on modelling and simulation I would like to give a special acknowledgement to Prof. Georg Fieg, Prof. Jobst Hapke, Dr. Chakkrit Na Ranong and all the staff of the Institute of Process and Plant Engineering at the Hamburg University of Technology. I appreciate very much the collaboration of Dr. Na Ranong, the long discussion times and his invaluable feedback and friendly advice.

Many of the results of my research would not have been possible without the collaboration of the students from the Helmut Schmidt University: Stefan Walcker-Mayer, Stephan Dorn and Daniel Meyer, and from the DAAD Rise Program: Daniel Martin-Alarcon, Simon Thompson and Craig Holvey. I appreciate the financial support of the European Community in the frame of the Integrated Project “NESSHY—Novel Efficient Solid Storage for Hydrogen” and of the Helmholtz Initiative “FuncHy—Functional Materials for Mobile Hydrogen Storage”.

At the department of Nanotechnology I was lucky to work under a constant motivating and friendly atmosphere, which made every day a very nice experience. My thanks to all current and former outstanding colleagues: Ulrike Bösenberg (my phenomenal office mate), Dr. José Bellosta von Colbe (for his nice support and suggestions), Oliver Metz, Claudio Pistidda, Julian Jepsen, Christian

Bonatto-Minella, Anna Arendarska, Dr. Rapee Gosalawit, Dr. Ivan Saldan, Dr. Klaus Taube, Dr. Karina Suárez, Christian Horstmann, Dr. Michael Störmer, Dr. Gagik Barkhordarian, Julian Puszkiel, Fahim Karimi, Sabine Schrader, Liane Bellosta von Colbe and Prof. Michael Dahms. I am very thankful to Dr. Nico Eigen for the initial supervision and introduction to the topic of complex hydrides during the early stage of my thesis.

I thank my parents, Gustavo and Julia, for their commitment in my education and the freedom I enjoyed in having independent ideas. I thank also my brother and sister, Gabriel y Cristina, for their constant patience and moral support in my life.

This dissertation is dedicated above all to my lovely wife Gabriela, who is and was my inspiration and strength during all this time, who changed my life for good and whom I owe the successful and peaceful development, writing and finish of this thesis. Muchas gracias Gaby.

Geesthacht, December 2010

Contents

1 Introduction

Mankind continuously requires energy for its ongoing activities, well-being and further development. Nowadays, more than 80 % of worldwide utilized energy comes from fossil-fuel sources i.e. coal, gas and petroleum [1, 2]. Unfortunately, there are several drawbacks associated to the usage of fossil-fuels. Firstly, the energy supply reserves from fossil fuels are limited, and actually it is estimated that oil production will peak and go into sustained decline within the next years [3]. Furthermore, during fossil-fuel energy transformation to its final application, pollutants are generated and exhausted into the environment. The emissions produced from the use of fossil-fuels, mainly carbon dioxide, cause a strong negative impact on the climate, with alarming consequences for climate change if the current fossil-energy usage trend continues [4]. The imbalanced distribution of the fossil-fuel resources throughout the world is another drawback. This later issue may bring economical and political conflicts as well as instability and confrontations. The drawbacks of the fossil-fuel based energy have created the major challenge and necessity of searching for and developing alternative and sustainable energy sources.

Assuming a scenario in which there is not any fossil-fuel supply, what other primary energy source do we have at our disposal? Alternatives based on existing energy sources in the planet, like nuclear energy, have both the inherent non-sustainable character and the collateral imbalanced distribution of the resources in common with the fossil-fuels. Fortunately, there is a rich extern flow of energy that comes to the planet in a more equitable distribution: radiation from the sun.

1.1 Hydrogen as solar energy carrier

With an incoming power of 0.56 kW m^{-2} [5], one hour of sun radiation coming on Earth's surface provides the energy that the mankind consumes in one year (5×10^{20} J [1]). Solar energy comes from nuclear fusion reactions that occur deep inside the sun's core. Enough nuclear fuel in the sun is estimated to last for a further 5 billion years [5]. Thus, solar energy could cover the energy demand of mankind in a long timescale. The challenge is the transformation of the incoming solar energy and its delivery as useful energy to final applications. Solar energy can be directly and indirectly transformed into electricity by means of photovoltaic cells, hydropower, wind-powder, solar-thermal, bio-mass, etc. Due to seasonal variations and long distances, besides looking towards decentralized and mobile

applications, if electricity is not immediately used it may be stored for later transportation and usage. Efficient electricity storage is a major problem. The solar energy challenge is then redefined as electricity production, storage, and use in a final application.

In the hydrogen-based energy cycle, solar energy is transformed into electrical energy. Electrical energy is subsequently applied in an electrolyser to produce hydrogen and oxygen from water. The consumed electricity is indirectly "stored" by the production of hydrogen. The produced oxygen is released into the atmosphere while hydrogen is stored, "carrying" the consumed electricity. Solar energy may also be transformed into hydrogen through other methods (e.g. biological hydrogen production by algae). After its storing, hydrogen is brought to its final application, releasing the "stored" energy. Usage of hydrogen is envisioned mainly in a fuel-cell by reacting with oxygen from the atmosphere, producing water as the only by-product. The produced water may be reused e.g. in the initial electrolysis. Therewith the hydrogen-based energy cycle is closed and neutral to the environment. There is no other sustainable, clean and high density energy concept with the simplicity and maturity as the hydrogen-based energy cycle. Hydrogen in this clean energy concept, as it has been illustrated, offers a high potential and is considered as an ideal energy carrier. Another important advantage of using hydrogen stems from the fact that even if hydrogen is produced from fossil-fuels, the final environmental impact is reduced when compared to impact of the direct use of the fossil fuels [6].

The energy challenge is once more redefined, now into efficient hydrogen production from electricity, hydrogen storage and hydrogen reconversion into electricity. It must be stressed that the direct use of electricity has a of course higher efficiency than the pathway of the hydrogen energy cycle: hydrogen is conceived as secondary energy carrier.

1.2 Hydrogen storage: metal hydrides as high density alternative

In the hydrogen-based energy cycle, besides efficient hydrogen production and reconversion of the stored energy into electricity, hydrogen storage is a main challenge. Hydrogen storage should fulfil defined requirements, specially for mobile applications and if focusing on automobiles [7, 8]. Distinct features of the hydrogen storage systems are evaluated, such as volumetric capacity, gravimetric capacity, charging time, delivery rate, operation conditions, costs. These are mainly compared to the actual gasoline-based storage systems for automobiles. It must be pointed out that as fossil-fuels are depleted, the paradigm is likely to change and storage requirements should change too, adapting to the new available energy technologies.

On one hand, hydrogen has a gravimetric energy density (119.9 MJ kg^{-1}) higher than gasoline (44.5 MJ kg^{-1}). On the other hand, compared to gasoline, the volumetric energy density of hydrogen at normal conditions is not high enough due to its low volumetric density. Hydrogen storage systems are aimed at the enhancement of the volumetric hydrogen density while maintaining high gravimetric hydrogen densities. Compressed hydrogen gas is the most common storage system [9]. However, the required high pressures of up to 700 bar to obtain adequate storage densities are a serious safety issue. Also, as the storage pressure increases, thicker walls for the recipient are required and the gravimetric capacity of the system is therefore strongly affected. Hydrogen may be also stored as liquid at very low temperatures (20 K at 1 bar, see Fig. 1.1). Unfortunately, this latter method requires a large amount of energy necessary for the liquefaction, and continuous boil-off loses limit its usage to short-term and large scale storage applications, e.g. space applications. It must be considered that the density of molecular hydrogen is thermodynamically limited by pressure and temperature. This limitation is illustrated in the pressure-density diagram of molecular hydrogen in Fig. 1.1 (based on the data reported by Vargaftik [10]). Desired densities up to 50 kg m^{-3} at room temperature can be achieved only under pressures higher than 1000 bar. Storage at conditions under high pressure and low temperatures, e.g. 80 K and 200 bar, are interesting possible options to achieve high densities [11, 12]. In any case, this option needs to overcome simultaneously the hurdles of compressed gas (high pressures) and liquid hydrogen (energy consumption and high insulation requirements).

Solid-state storage of hydrogen is an alternative to gas and liquid molecular hydrogen storage, in which the hydrogen density can be significantly increased. The solid-state methods include physisorption, irreversible chemical hydrides and metal hydrides. Effective physisorption of hydrogen is possible in materials with very large specific surface areas like zeolites or carbon-nanotubes. Physisorption requires low temperatures and presents thus similar problems as liquid hydrogen. In the case of irreversible chemical hydrides, hydrogen is liberated by their oxidation with water. The process is not directly reversible and the chemical hydrides must be regenerated off-board. This feature restricts this storage alternative to some specific applications and makes it non-promising if reversibility (or regeneration on-board) is a key requirement.

Metal hydrides offer a safe alternative to hydrogen storage in compressed or liquid form, having higher storage capacity by volume. For instance, Mg_2FeH_6 has the highest known hydrogen volumetric density (150 kg H_2 m^{-3} [13]), which is more than twice the density of liquid hydrogen and three times that of compressed gas under 1000 bar. As consequence, metal hydride tanks do not require the high pressures of compressed gas tanks to achieve high densities and are thus much safer.

The high density hydrogen storage in metal hydrides involves a solid-gas reversible chemical reaction, between hydrogen and a metal, a metal alloy or a metal composite. A considerable amount of energy is either released during hydrogen charging or required during hydrogen discharging. The storage is in

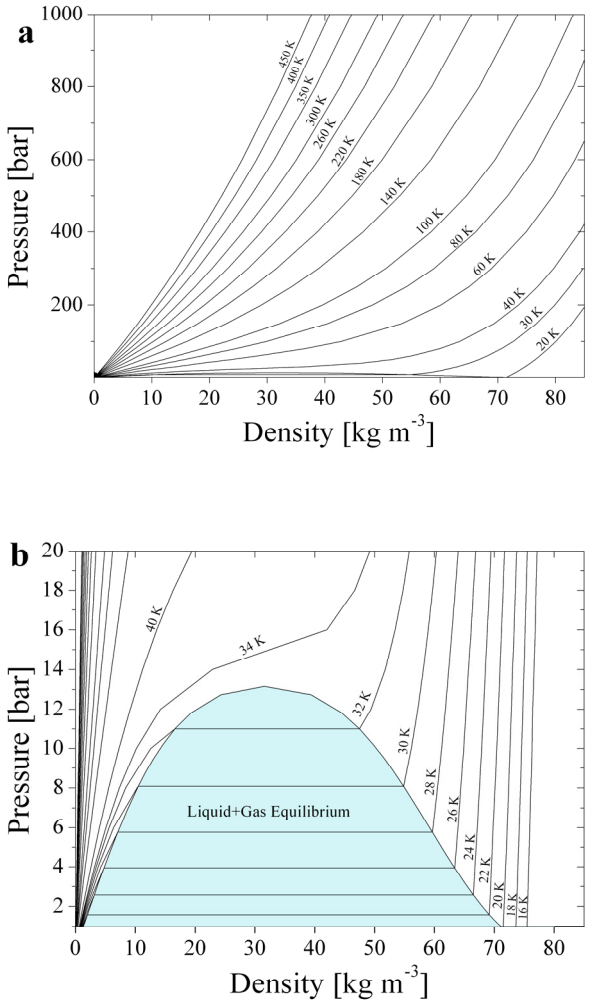

Figure 1.1: Pressure-density diagram of molecular hydrogen (based on the data reported by Vargaftik [10])

consequence regulated by temperature and pressure conditions. Unfortunately, the energy of the reaction is not accounted in the stored useful energy. Low operating temperature and pressure as well as low energy of reaction are required for practical metal hydride systems. Furthermore, the kinetics of the reaction should be fast enough in order to fulfil the requirements of the storage system concerning charging times and delivery rates. In this direction, a breakthrough was achieved by preparing nanocrystalline hydrides using high-energy ball milling and the use of suitable catalysts/additives [14-17]. The final storage system, apart of being reversible, should have high volumetric and gravimetric hydrogen capacities. All storage criteria must be taken in consideration during the evaluation of a metal hydride reacting system.

Conventional intermetallic hydrides, like $LaNi_5H_6$ and $TiFeH_2$, are advantageous, because they require low operating pressures and temperatures. The main drawback is their poor gravimetric hydrogen storage density in the order of 2 wt%. Therefore, in recent years, research has focused on light weight complex hydrides, which have a high capacity both by weight and by volume, e.g. $LiBH_4$ with about 18 wt% and a density of 121 kg H_2 m^{-3}. Nevertheless, their operational temperatures are until now too high for practical applications [18] and some other complex hydrides are even not reversible. Among complex hydrides, a good compromise between operation conditions and gravimetric capacity is $NaAlH_4$, reversibly working under moderate temperature conditions e.g. around 125 °C for charging, having a theoretical capacity of 5.6 wt% and a storage density of 70 kg H_2 m^{-3}. In a recent approach by Barkhordarian et. al. [19-21], composites of light/complex metal hydrides (reactive hydride composites) were developed, and it was demonstrated that they can reversibly absorb and desorb hydrogen with a lower hydrogen reaction enthalpy than the pure hydrides. Thus, milder conditions of pressure and temperature for the storage may be expected. Besides, the gravimetric hydrogen capacity is still interestingly high, for instance 11.4 wt% for the system $LiBH_4$+MgH_2 are theoretically possible, and 10 wt% have been demonstrated [22]. Research is in progress in order to understand their reaction mechanisms, overcome kinetics hurdles and tune them to react at the thermodynamically possible temperatures.

Hydrogen storage systems based on metal hydrides need large amounts of reacting material in practical applications, i.e. kilogram scale. Basic research and first developments of metal hydride reacting systems is performed in small (mg) scale. In order to exploit the properties of metal hydrides in suitable hydrogen storage systems, it is required to understand their performance in larger powder beds. During hydrogen sorption not only the chemical reaction takes place, but also coupled hydrogen transport and heat transfer. As it will be experimentally and theoretically shown in the present work, heat transfer is the most probable sorption limiting sub-process in practical systems. Consequently, spatial temperature and concentration profiles are developed during the hydrogen storage process. Sophisticated tools are then required for the evaluation of the sorption behaviour of metal hydride reactors. The ultimate objective is to be able to design, optimise and construct suitable high density hydrogen storage systems based on metal hydrides. Coupling material development and scale-up in larger scale systems is fundamental looking towards fulfilling the storage challenges of a hydrogen-based energy cycle with the promising potential of metal hydrides.

1.3 Scope and structure of the present work

The present investigation focuses on the development of scaled-up hydrogen storage using sodium alanate material, on the basis of both experimental and theoretical approaches.

In the experimental approach, presented in Chapter 3, first the influence of the size of the hydride bed on its hydrogen absorption behaviour is studied. In order to understand the thermal effects on the hydrogen sorption of sodium alanate material, a special cell is designed and constructed. By means of this cell hydrogenation kinetics and temperature profiles within the bed can be simultaneously followed. Moreover, the effective thermal conductivity of the material, a fundamental property for metal hydride tanks design, is estimated from the measurements of the cell. Enhancement of the effective thermal conductivity of the sodium alanate material is evaluated by additions of expanded graphite. The experimental work is complemented by the study of cycling, kinetics and heat transfer in metal hydride tanks up to kg scale. With this aim, a hydrogen tank station is designed and constructed. The absorption behaviour of alanate tanks is evaluated as well as the effect of the addition of expanded graphite to improve the effective thermal conductivity of the scaled-up reacting system. In order to implement simulations and further evaluations, empirical kinetic models for both hydrogen absorption and desorption of sodium alanate material are developed. Optimal theoretical pressure-temperature conditions for hydrogen sorption of sodium alanate material can be determined using the developed model. A new approach is proposed for the mass balance of the reactions when implementing the reacting model. It describes the material as a mixture composed of different types of reacting materials, which avoids the use of correction terms for the experimental capacities, as it is commonly done in other empirical sorption models for metal hydrides.

In the theoretical approach, presented in Chapter 4, the hydrogen sorption process of practical systems based on hydride beds is modelled for the simultaneous sub-processes of hydrogen transport, intrinsic reaction and heat transfer. Based on the modelling equations, a comparative resistance analysis is developed in order to quantify the effect of each sub-process on the overall sorption kinetics in sodium alanate beds. It is shown that large size systems of sodium alanate material are mainly heat transfer limited. On the basis of the modelling equations, a numerical simulation is developed and validated with the experimental results previously obtained in this work.

The work finishes at Chapter 5 by showing combined approaches to optimise hydrogen storage based on sodium alanate material. In the first part of the Chapter, optimisation of the volumetric hydrogen storage capacity is experimentally demonstrated by powder compaction. Interesting results are found on the sorption behaviour of these manufactured compacts. In the second part of the Chapter, a tubular tank filled with sodium alanate material is theoretically optimised towards its gravimetric hydrogen storage capacity using the simulation developed in the theoretical approach and the experimental results obtained during this investigation.

1.4 Model system: sodium alanate

Sodium alanate, $NaAlH_4$, is a medium-temperature complex hydride with a high reversible hydrogen content at moderate conditions (5.6 wt%). When compared to classical room temperature hydrides, sodium alanate offers a suitable compromise with relatively large gravimetric storage capacity at temperatures of around 125 °C. The thermal decomposition of sodium alanate, releasing hydrogen, has been known for many years. Nevertheless, the pure material shows very slow kinetics during both hydrogen absorption and desorption. In 1997 Bogdanovic and Schwickardi [17] showed that hydrogen can be reversibly stored in and released from sodium alanate if doped with titanium compounds. $NaAlH_4$ is reversibly formed in a two-step reaction within the technically suitable range of up to 125 °C, see Eqs.1.1 and 1.2. It has a theoretical gravimetric hydrogen storage capacity of 5.6 wt% based on the absorbed material, or 5.9 wt% if based on the desorbed material.

$$3NaH + Al + 1.5H_2 \leftrightarrow Na_3AlH_6 \tag{1.1}$$

$$Na_3AlH_6 + 2Al + 3H_2 \leftrightarrow 3NaAlH_4 \tag{1.2}$$

If further hydrogen release from NaH forming Na is considered, the total hydrogen content goes up to 7.4 wt%. Due to the high decomposition temperature of NaH (>400°C), for practical applications only the hydrogen stored in the reactions shown in Eqs. 1.1 and 1.2 is considered. The group of compounds taking part in these equations, which is sometimes also called Na-Al-H system, will be referred in this work as sodium alanate material.

The thermodynamic equilibrium of the reacting system was studied in detail by Bogdanovic [23]. Figure 1.2 shows the thermodynamic stable states of the reacting system depending on the p-T conditions. The equilibrium lines in Fig. 1.2 are calculated using the van 't Hoff equation with standard reference pressure of 1 bar, Eq. 1.3.

$$\ln\left(\frac{p_{eq}}{1\,\text{bar}}\right) = \frac{\Delta H_R}{RT} - \frac{\Delta S_R}{R} \tag{1.3}$$

The parameters reported in [23] for the sodium alanate reacting system are summarized in Table 1.1. According to the van 't Hoff equation with the values in Table 1.1, the equilibrium temperature at 1 bar corresponds to 30°C for the decomposition of $NaAlH_4$ forming Na_3AlH_6 and Al (Eq. 1.2), and 100°C for the decomposition of Na_3AlH_6 (Eq. 1.1). However, due to kinetic restrictions, the material shows reactivity only at temperatures above 70 °C.

Table 1.1: Enthalpy and entropy of reaction for the sodium alanate reacting system [23].

Sorption reaction	ΔH_R **[kJ mol H_2^{-1}]**	ΔS_R **[J mol H_2^{-1} K^{-1})]**
$3NaH + Al + 1.5H_2 \leftrightarrow Na_3AlH_6$	-47	-126
$Na_3AlH_6 + 2Al + 3H_2 \leftrightarrow 3NaAlH_4$	-37	-122

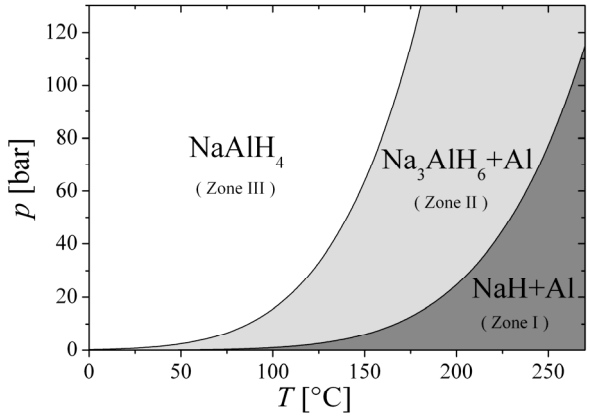

Figure 1.2: p-T diagram presenting the most stable state of the sodium alanate reacting system under H_2 pressure. At p-T conditions inside zones I, II and III, NaH+Al , Na_3AlH_6+Al, and $NaAlH_4$, respectively, are the most stable states.

2 Experimental methods

This chapter explains the method of material preparation and the applied measuring techniques in this investigation. The thermocell and the hydrogen charging station are described in detail, since they were specially constructed during this work to complement the utilized standard methods of analysis.

2.1 Material preparation

All sodium alanate material used for this work was produced in an industrial scale like milling equipment, optimised towards fast kinetics and using a titanium-based inexpensive catalyst [24-26]. The average batch of milled material weighted up to 1 kg. The raw materials were commercial NaH (95 %, Sigma Aldrich Chemie GmbH, Steinheim, Germany), aluminium (99,5 %, Johnson Matthey GmbH & Co. KG, Karlsruhe, Germany), aluminium-reduced $TiCl_4$ as catalyst precursor (Fluka Chemie GmbH, Buchs, Switzerland). Carbon powder (graphite powder, Alfa Aesar GmbH &Co. KG, Karlsruhe, Germany) was added afterwards as milling agent, expecting faster kinetics in the milled material as it was shown in several studies of hydrogen absorbing materials, including magnesium hydride and sodium alanate [24, 27-30]. All handling, including milling, was carried out in a glove box with purified argon atmosphere. Prior to milling, NaH and aluminium were pre-mixed in a rolling bank in a molar ratio of 1.08 to 1 according to the reaction.

$$\begin{aligned} &1.08\,\mathrm{NaH} + \mathrm{Al} + 0.02(\mathrm{TiCl_3} + \tfrac{1}{3}\mathrm{AlCl_3}) \\ &\rightarrow \mathrm{NaH} + 1.0067\,\mathrm{Al} + 0.08\,\mathrm{NaCl} + 0.02\,\mathrm{Ti} + 0.04\,\mathrm{H_2} \end{aligned} \tag{2.1}$$

This reaction is expected to occur during milling [31]. The ratio 1.08 to 1 was chosen considering the sodium hydride that is consumed by the catalyst precursor. Milling was carried out in a modified vibratory tube mill (ESM 236, Siebtechnik, Mühlheim a. d. R., Germany), using 30-mm hardened balls at a rotational speed of 1000 rpm and a ball-to-powder ratio (BPR) of 140:1. In order to avoid agglomeration, wet milling using cyclohexane was employed. After milling, the mill was evacuated to dry the samples. In order to investigate the influence of carbon on the hydrogenation behaviour, part of the material was prepared in the same way as described before. For this material additional 5 wt% of carbon was added after ball milling, and milled for another 30 min.

The calculated material balance and hydrogen capacities of the sodium alanate material of this investigation are presented in detail in the appendix.

2.2 Sorption kinetics

The sorption kinetics of the material was characterized volumetrically using a Sieverts' apparatus (HERA, Quebec, Canada), that works based on a pressure-volumetric method combined with differential-pressure measurements [32]. Cells with inner diameters of 2, 4.5, 10 and 15.2 mm were used, Fig. 2.1. During all the experiments the external temperature on the wall of the cells was measured. The loading of the milled material in each of the cells was done inside an argon glove box. Each cell was homogeneously loaded with the milled material and immediately weighted afterwards (mg precision scale). The weight of material in the cells was around 40 mg (2 mm cell), 150 mg (4 mm cell), 1300 mg (10 mm cell) and 5000 mg (15 mm cell).

The 15 mm diameter cell was additionally equipped with 5 thermocouples, Fig. 2.2, which further on will be called thermocell. The used thermocouples are type K, with outer diameter 1 mm and fast response grounded junction. The cell was designed to enable measurements up to temperatures of 400 °C and pressures up to 200 bar. The temperature measurements throughout the hydride bed with this cell make it possible to analyse the heat flow in the system during the reactions and to estimate the effective thermal conductivity of the bed.

Figure 2.1: Cells of different inner diameter utilized for sorption measurements in the Sieverts' apparatus. Inner diameter from left to right: 2 mm, 4.5 mm, 10 mm and 15.2 mm.

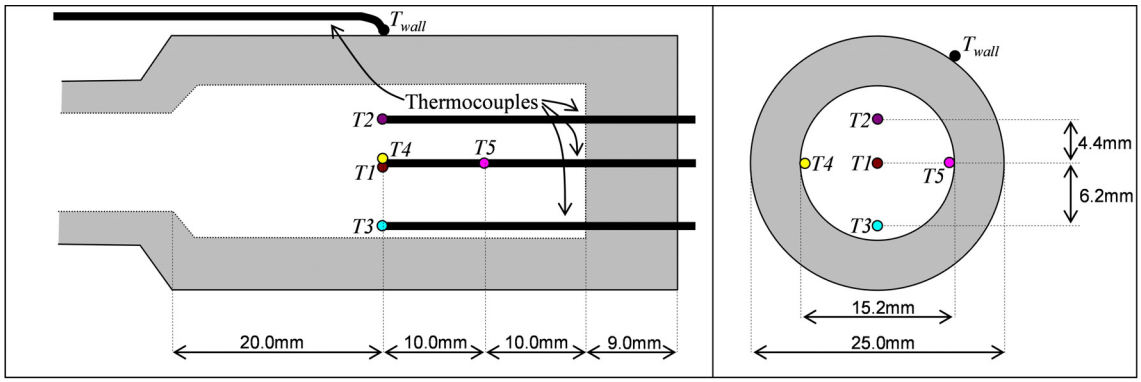

Figure 2.2: Thermocouples positions in the 15 mm diameter cell (thermocell) for heat flow analysis during absorptions and desorptions.

2.3 Hydrogen tank station

The use of a Sieverts' type apparatus for the evaluation of hydrogen sorption of large amount of material would be impractical since it would require huge reference volumes. For instance, a reference volume of 650 l would be required to measure the hydrogen sorption of 100 g of sodium alanate material, expecting a pressure change of 0.1 bar during the measurement. Therefore, in order to study cycling, kinetics and heat transfer in hydride tanks up to kg scale, a hydrogen tank station was designed and constructed. Basically, the installation allows the quantitative evaluation of the hydrogen charging (discharging) process into (from) a tank, which is filled with a metal hydride (e.g. sodium alanate). The charge (discharge) of gas into (from) the tank and the hydride is determined and controlled by measuring the temperature, pressure and the gas mass flow. A simplified process flow diagram of the installation is depicted in Fig. 2.3. In the appendix the detailed piping and instrumentation diagram (P&ID) of the installation is presented. The accessories and instruments of the installation are rated to work up to 130 bar.

The amount of hydrogen that has been absorbed by the material between two different times t_0 and t_f is calculated from the hydrogen mass balance on the gaseous phase of the tank:

$$m_{\mathrm{H}_2,abs}\Big|_{t_f} - m_{\mathrm{H}_2,abs}\Big|_{t_0} = \left(V_g \rho_{\mathrm{H}_2}(\overline{T},\overline{p})\right)\Big|_{t_0} + \left(\int_{t_0}^{t_f} \dot{m}_{\mathrm{H}_2} dt\right) - \left(V_g \rho_{\mathrm{H}_2}(\overline{T},\overline{p})\right)\Big|_{t_f} \qquad (2.2)$$

The first and third terms on the right side of the equation corresponds to the hydrogen mass present in the gaseous phase at times t_0 and t_f, respectively. The second term on the right side accounts the total

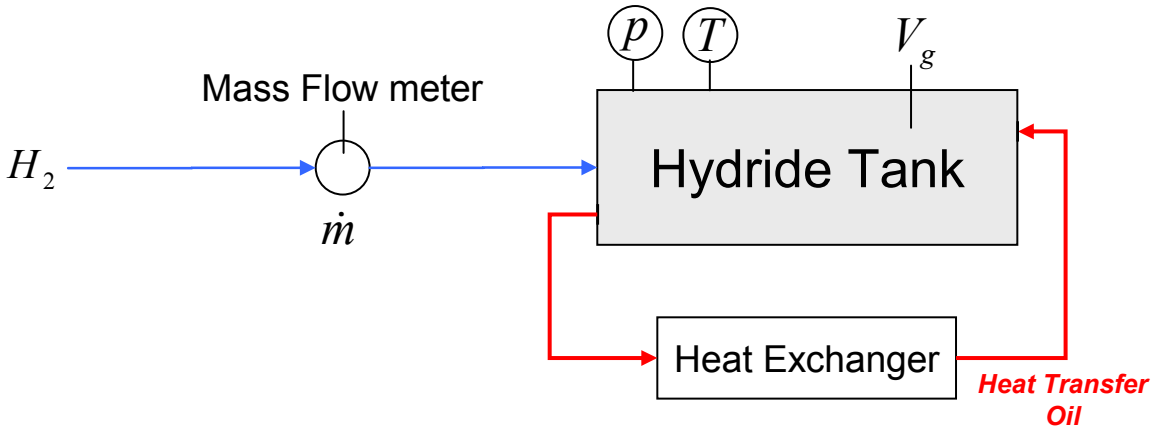

Figure 2.3: Simplified process diagram of the hydrogen tank station.

hydrogen that flowed into the system between times t_0 and t_f. Gas density, ρ, is calculated by means of the van der Waals equation at the temperature and pressure of the tank. At high levels of pressure (>50 bar), the density calculated using ideal gas law has noticeable relative error when compared to experimental density values [10].

The volume of the gaseous phase within the hydride tank, V_g, is required for the calculations. Prior to the experiments with hydrogen, this volume was calibrated using Argon, chemically inert to the hydride material. The calibration is based on the following equation (derived from Eq. 2.2 for the case of argon):

$$V_g = \frac{\int_{t_0}^{t_f} \dot{m}_{\mathrm{Ar}} dt}{\rho_{\mathrm{Ar}}(\bar{T},\bar{p})\big|_{t_f} - \rho_{\mathrm{Ar}}(\bar{T},\bar{p})\big|_{t_0}} \tag{2.3}$$

Tanks of the company Swagelok of stainless steel 316L were utilized for the scale-up measurements [33]. A schematic diagram of the tank is presented in Fig. 2.4. All handling, including the tank filling procedure with the material, was done inside a glove box with purified argon atmosphere. During measurements, the hydrogen is distributed inside the tank by a sintered metal filter. The filter was equipped with a thermocouple located in its centre, which also corresponds to the centre of the hydride bed. A second thermocouple enters into the hydride from the other end of the tank. Its measuring tip is located in a non-defined position in the bed of material.

On one hand, during the hydrogen absorption heat is released and should be removed to maintain the required driving force for the absorption. During hydrogen desorption, on the other hand, heat should be supplied. In the charging station an external oil circuit regulates this heat management. The hydride

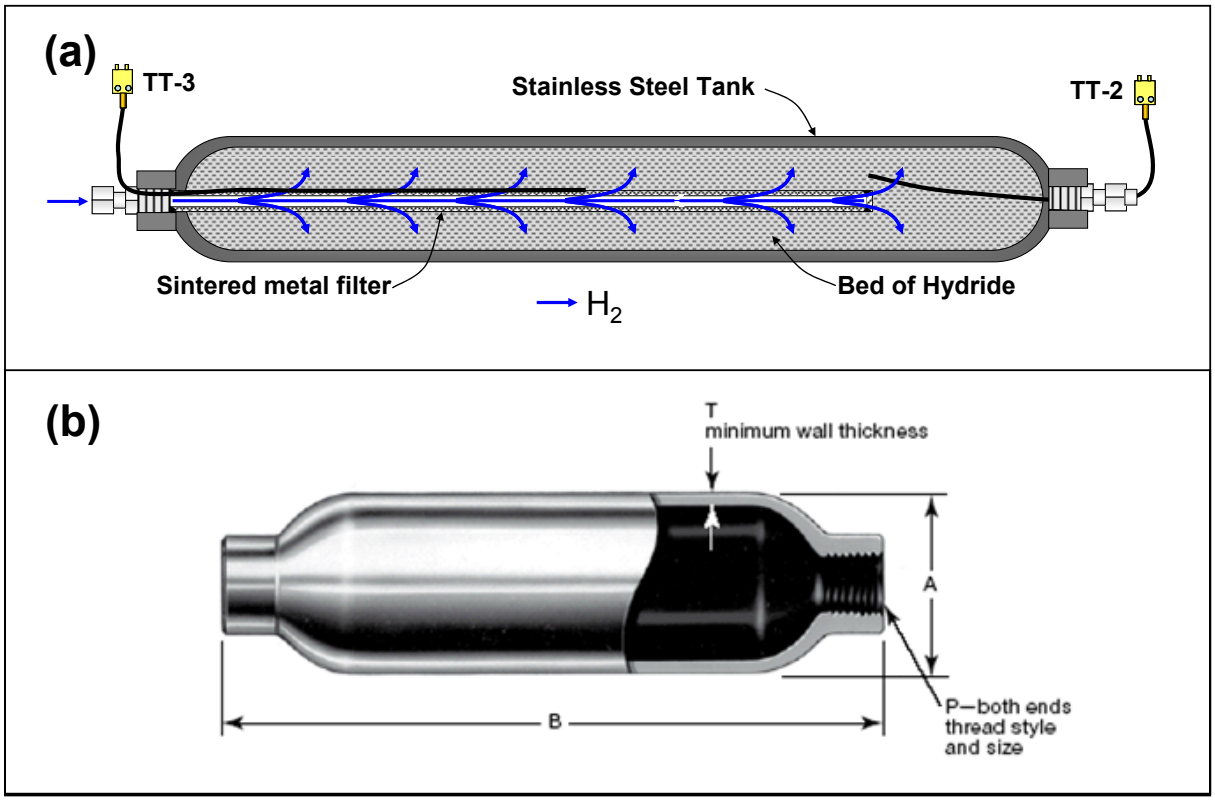

Figure 2.4: Tanks of stainless steel 316L for scale-up measurements. (a): Schematic profile of the tank, sinter metal filter and thermocouples. The filter is equipped with the thermocouple TT-3 located in the centre of the hydride bed. A second thermocouple TT-2 enters into the hydride from the other end of the tank. Its measuring tip is located in a non-defined position in the bed of material. (b): Dimensions of the tanks as presented in the Swagelok catalogue [33]. For the 300 ml tank and pressure rating until 300 bar: T= 6.1 mm, A= 48.2 mm, B= 368 mm, P=¼ inch NPT thread. For the 500 ml tank and pressure rating until 100 bar: T= 2.4 mm, A= 50.8 mm, B= 351 mm, P=¼ inch NPT thread.

tank is placed inside a plastic shell made of PEEK (polyether ether ketone), a polymer which has good mechanical properties at temperatures up to 250 °C and a relative low density (approx. 1.3 g ml^{-1}). The set-up of hydride tank and shell is similar to a heat exchanger of "double pipe" type configuration, Fig. 2.5. The outer annular channel is part of the oil circuit. A high-temperature thermostat (T max 400 °C from LAUDA GmbH) pumps the oil in the circuit and also regulates its temperature by means of heating resistances and an additional cooling system. The employed heat transfer oil was Ultra 350 (dibenziltoluene, LAUDA GmbH). This oil was used to minimize the risk associated with a possible leak, since it is non-reactive to sodium alanate material.

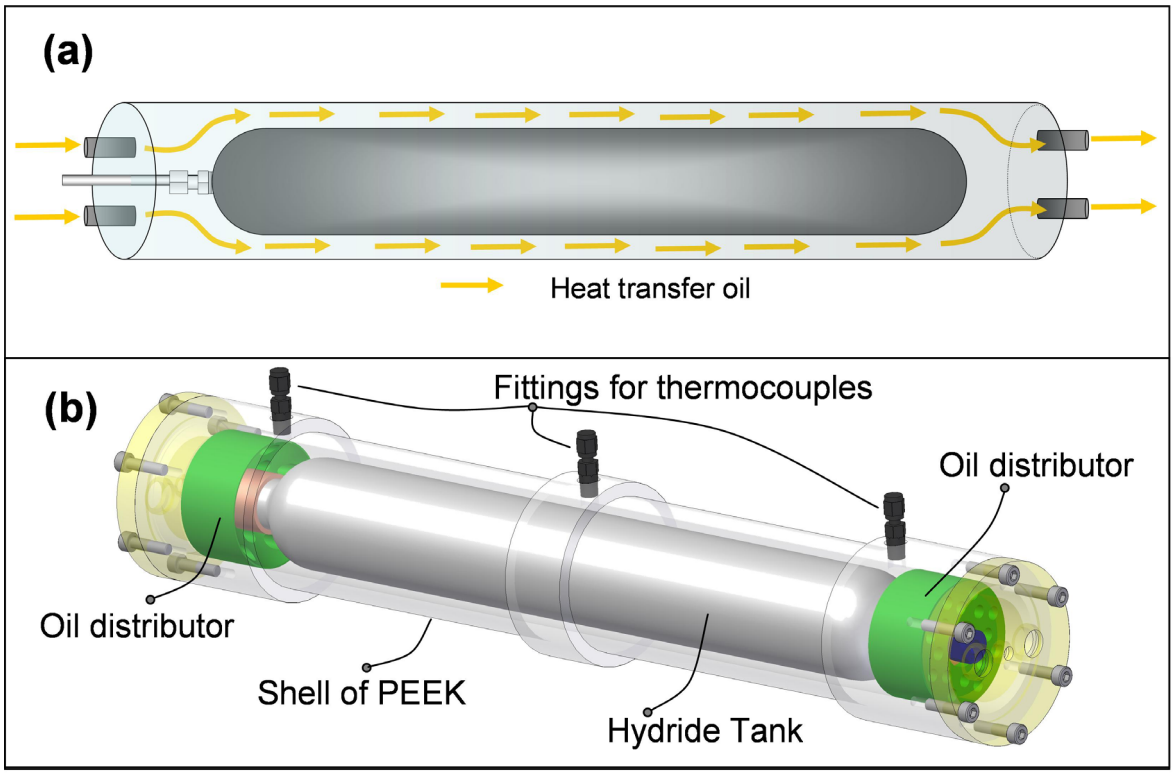

Figure 2.5: Hydride tank inside its shell as heat transfer configuration of "double pipe" type. (a): Schematic of the heat transfer oil pathway in the annular channel. (b): Intern configuration and accessories.

The temperature is measured using thermocouples type K from Thermocoax with fast response grounded junction (temperature range of -40 °C to 1300 °C, accuracy of 0.5 °C). The temperature is measured in the hydrogen pipeline, in two positions inside the hydride tank (see Fig. 2.4) and in three positions in the side of the heat transfer oil close to the tank (see Fig. 2.5). The absolute pressure is measured with a piezoresistive absolute pressure transmitter PAA-23 (pressure range of 0 bar to 200 bar, accuracy of 0.01 bar, KELLER AG). The gas flow is measured and controlled with two thermal flow meters (flow range from 0 ln min^{-1} to 10 ln min^{-1} and 0 ln min^{-1} to 250 ln min^{-1}, accuracy of 0.01 ln min^{-1} and 0.1 ln min^{-1}, respectively. Bronkhorst Mättig). In the thermal flow meters, a voltage signal is produced when a gas is flowing through. This signal is proportional to the mass flow and the heat capacity of the gas. The unit "ln", although not extendedly used but common in gas flow meters controllers, represents one normal litre e.g. one litre of gas under normal conditions of

temperature and pressure (0 °C and 1.01325 bar). For instance, a flow of 1 ln min^{-1} of hydrogen corresponds to a hydrogen mass flow of 0.08991 g min^{-1}, since $\rho_{H_2, 0\,°C, 1.01325\,bar}$ =0.08991 g l^{-1}.

The installation was automatically operated by an own developed LabView computer-based application, which accomplishes the on-line measurement, control, monitoring and regulation of the tank station. Temperature, pressure and mass flows are measured and saved on-line in the computer. Pneumatic valves were installed and controlled from the application. A snap-shot of the designed interface of the application and a general view of the tank station are presented in the appendix. A more extensive description of the experimental procedures and the installation as well as its risk and safety analysis is presented elsewhere [34].

3 Experimental sorptions: kinetics and heat transfer

This chapter starts with the experimental results on the effect of heat transfer on the sorption kinetics of sodium alanate material [35]. Further on, developed empirical kinetic models for the absorption and desorption of the material are presented [36, 37]. The last part of the chapter focuses on scaled-up sorptions of the material. The chapter is organized in four different sections that cover the mentioned investigated themes. Each section begins with the description of the experimental results and concludes with the respective discussion.

3.1 Effects of heat transfer on the sorption kinetics

This section pursues an advanced understanding of the factors that influence charging and discharging kinetics in large beds of sodium alanate material. In particular, the effect of the carbon powder addition during milling, sorption temperature and the size of the hydride bed on the reactions kinetics of sodium alanate material catalyzed with aluminium-reduced $TiCl_4$ ($3TiCl_3+AlCl_3$) is studied in detail. For this purpose, titration measurements were performed using cylindrical cells of different diameters, as presented in Fig. 2.1. To understand the underlying mechanisms, the temperature was measured during the process at different positions inside the hydride bed using the constructed thermocell (described in Section 2.2 and shown in Fig. 2.2). The measurement with the thermocell provides detailed information about the influence of heat conduction and temperature on the reaction kinetics. This section concludes with the evaluation of the addition of expanded graphite flakes on the sorption behaviour of sodium alanate material. Expanded graphite was mixed with sodium alanate material after milling, contrary to carbon powder which was added before material milling.

3.1.1 Absorption in cells of different sizes

The hydrogen absorption process, which corresponds to filling an automotive tank, is required to last only a few minutes and is therefore much more demanding than the discharging process. Consequently, it will predominantly determine the design of the heat transfer system of a practical application. In this subsection the results are focused on the effect of the cell size on the absorption profiles. The conclusions and discussion with respect to the cell size are valid for the results obtained

with sodium alanate material both with and without carbon addition during milling. The absorption profiles of the material with and without carbon addition are further compared and analyzed in subsection 3.1.5 (see Fig. 3.10). To allow for comparable results the third absorption is taken always to analyze the effect of the powder bed size on kinetics. With this absorption cycle the material has almost reached steady kinetic properties with respect to cycling.

Figure 3.1 shows the absorption profiles of both types of materials (with and without carbon addition) obtained with the cells of different dimensions. Figure 3.2 shows the respective external wall temperature against time. Although the hydrogen capacities after 20 min are similar, the slopes of the curves, and therefore the reaction rates, are notably different. For instance, the 10-mm cell led to the fastest initial kinetics (ca. 3.2 wt% min^{-1}) while the 2-mm cell presented the slowest kinetics (ca. 0.6 wt% min^{-1}).

3.1.2 Absorptions in the thermocell

Sets of experiments were carried out using the thermocell, filled with sodium alanate material with and without carbon powder addition during milling. Figure 3.3 shows the 3rd absorption measurement of sodium alanate material without and with carbon powder addition. The initial temperature was again 125 °C. Quite similar results are obtained with and without carbon addition, and therefore the description presented in the discussion is valid for both types of material. The effects of expanded graphite addition to sodium alanate material after milling are presented in subsection 3.1.4.

3.1.3 Estimation of effective thermal conductivity

A further important factor necessary for the layout of a storage system based on hydrides is the effective thermal conductivity. The positions of the thermocouples in the thermocell in Fig. 2.2 were chosen in order to estimate the effective thermal conductivity of the material bed upon the hydrogenation/dehydrogenation reaction in-situ. The measuring positions were arranged in such a way that a parabolic temperature profile throughout the bed could be measured with uniform and sufficient temperature variation between the positions: calling ΔT the total difference of temperature between the material close to the wall of the cell and the material in the centre (axis) of the cell, T4 reads 0 % of ΔT, T3 reads 33 %, T2 reads 67 % and T1 reads 100 % of ΔT. T1 is located exactly in the centre of the bed.

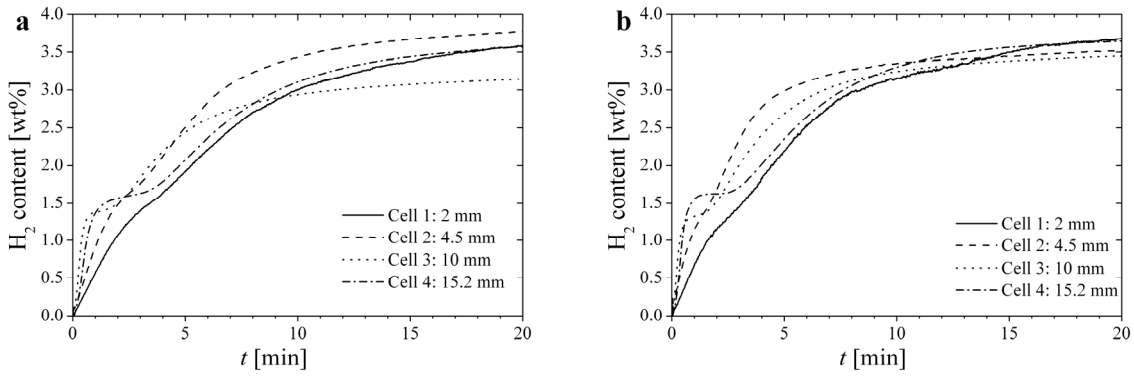

Figure 3.1: Hydrogen content from material (a) with and (b) without carbon addition during 3rd hydrogen absorption measurement with different cells at 100 bar in the Sieverts apparatus. The initial temperature is 125 °C.

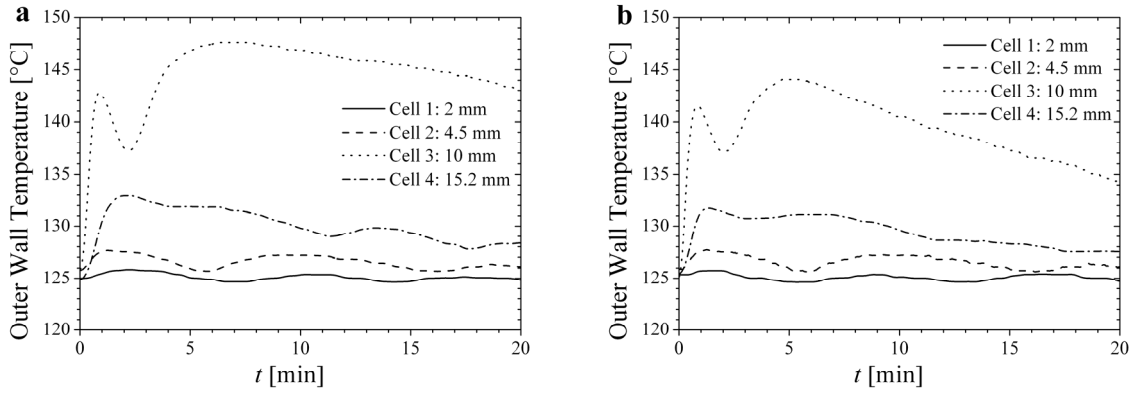

Figure 3.2: Outer wall temperature of the samples with (a) and without (b) carbon addition during the 3rd hydrogen absorption measurement using different cells at 100 bar in the Sieverts apparatus. The initial temperature is 125 °C.

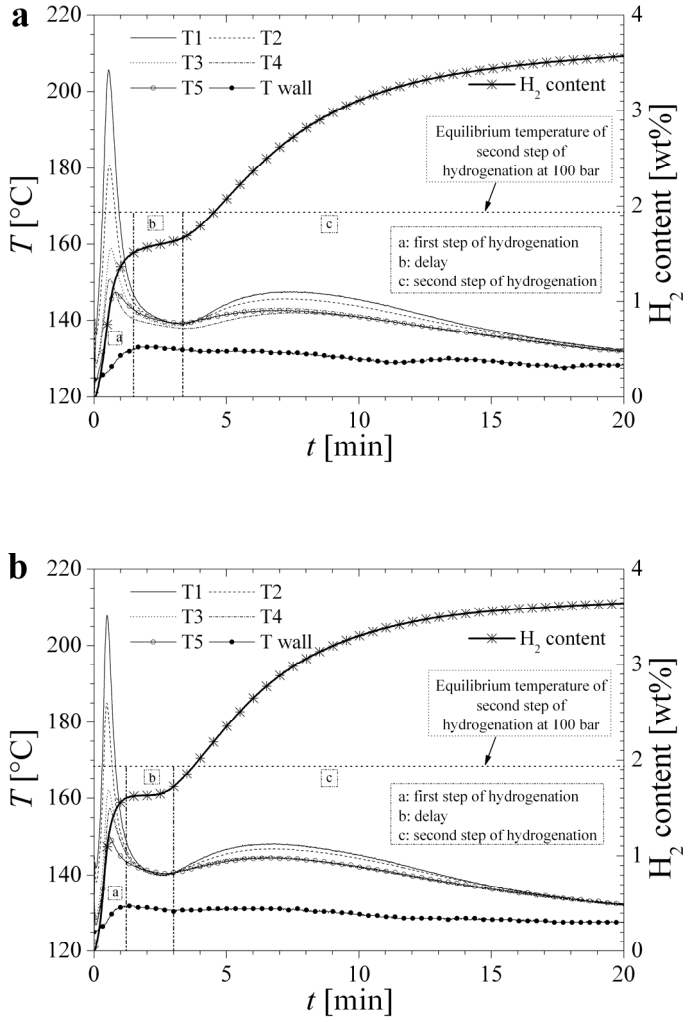

Figure 3.3: Hydrogen content and temperature inside the bed of hydride of samples (a) without and (b) with carbon addition during the 3rd hydrogen absorption measurement at 100 bar, measured in the Sieverts apparatus. The initial temperature is 125 °C. The positions of temperature measurements are presented in Fig. 2.2.

3.1.4 Addition of expanded graphite

Heat conduction is a major aspect during the hydrogen sorption of metal hydrides. Unfortunately, the discontinuities of the solid milled material lead to lower effective thermal conductivities of the beds. The effective thermal conductivity of metal hydride beds can be increased by mixing them with high thermal conducting materials. Diamond has the highest thermal conductivity by far of any solid at room temperature (2000 W m^{-1} K^{-1}) [38], but it is not an option for practical applications. Expanded

graphite (EG) has very high thermal conductivity (reported between 400-2000 W m^{-1} K^{-1} parallel to basal plane [38, 39]) and has been used as a heat transfer additive in other technologies, e.g. adsorption refrigeration, where high rates of heat transfer are required as well [40]. Its high thermal conductivity , which occurs essentially by lattice vibration [38], is due to the high-strength and short-length covalent sigma bonds in the planar hexagonal network of its structure. However, the anisotropy of the graphite crystal influences strongly the thermal conductivity. In the direction perpendicular to the basal plane the thermal conductivity is considerably lower (2-10 W m^{-1} K^{-1} [38, 39]), where weaker van der Waals bonds are present. Another advantage of EG is its low density (2.2 g ml^{-1} [38]), which adds less inert mass when used as thermal conductivity additive in metal hydride beds.

Sodium alanate material of this investigation was mixed with flakes of expanded natural graphite after ball milling in different ratios (particle size 500 μm, SGL Technologies GmbH, Meitingen, Germany). After weighing, the mixture was shaken in a glass recipient for several minutes in order to homogenize it for further measurements. The effect of the additional EG on the sorption behaviour of sodium alanate was tested by performing sorption measurements in the thermocell at the Sieverts apparatus, as it was done in subsection 3.1.2 (without any EG addition). The thermal conductivity for the mixtures was also estimated.

In Fig. 3.4 the first 20 min of the 3rd absorption measurements are shown for mixtures of different sodium alanate to EG ratios. Mixtures of 0, 5, 18 and 50 wt% EG were prepared. As clearly can be seen, each mixture displays quite different absorption behaviour and temperature profiles. As the EG content in the mixture increases, the achieved hydrogen capacities decrease. Moreover, it is also observed that the highest peak of the temperature profile measured during absorption is reduced as well. While the temperature increase is almost 100 °C for the mixture without EG, the mixture with 50 wt% of EG shows a temperature increase of < 1 °C only. In fact, the absorption of the 50 wt% EG proceeds practically isothermal.

3.1.5 Discussion

As shown in Figs. 3.1 and 3.2, the slopes of the curves, and therefore the reaction rates, are notably different during the absorption measurements in the cells of different size. This results from different temperature developments in the beds of material within the cells during the hydrogenation process. The smaller cells exhibit almost isothermal behaviour, while for the larger cells the outer temperature raises by about 10 to 20 °C. This can be explained by ineffective heat transfer with the surrounding air and a limited heat capacity of the vessel. The temperature rise caused by limited heat capacity of the vessel should decrease as the ratio mass of cell wall to mass of hydride, $M_{Cell\ wall}/M_{Hydride}$, increases, because the heat capacity of the cell acts as sink for the heat generated from the reaction. The

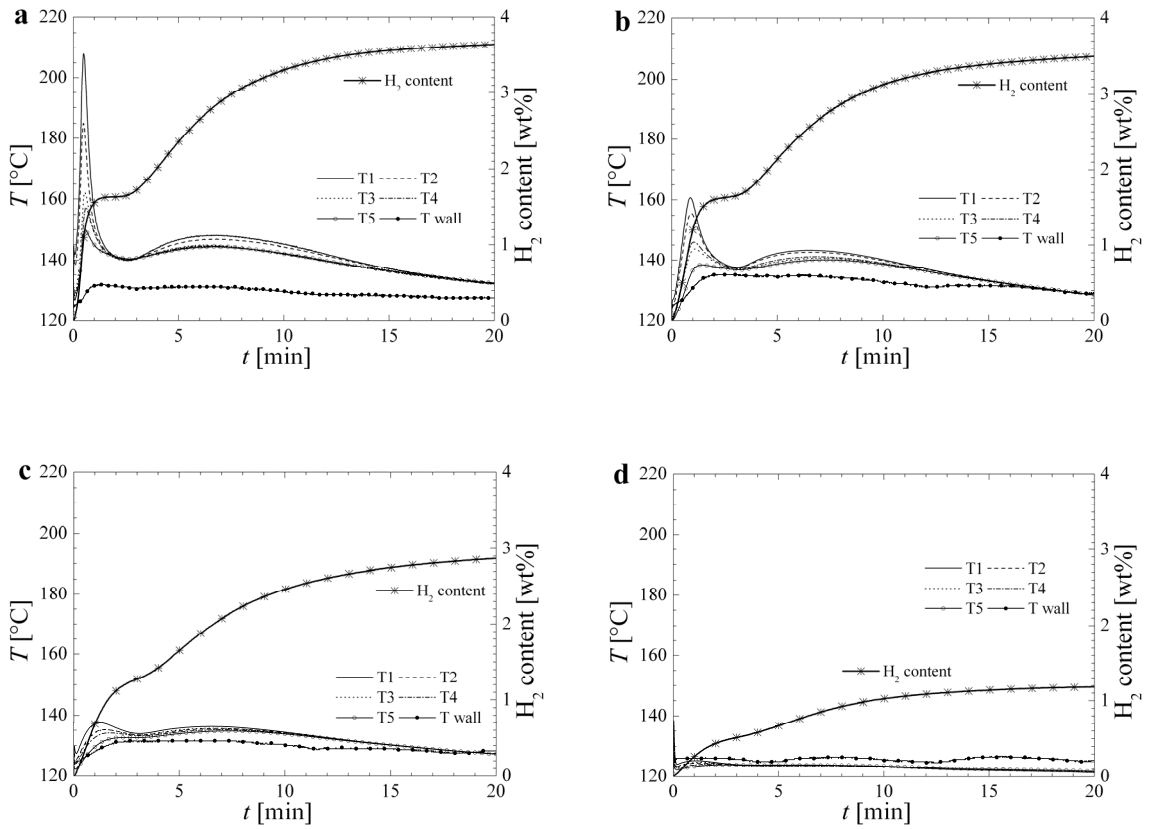

Figure 3.4: 3rd Absorption measuremnt at 100 bar in the thermocell for material (a) without EG, (b) with 5 wt% EG, (c) 18 wt% EG and (d) 50 wt% EG. The initial temperature was 125 °C. The positions of temperature measurement are presented in Fig. 2.2.

calculated ratio $M_{Cell\ wall}/M_{Hydride}$ is presented below in Table 3.1 for the different utilized cells. The ratio was calculated from the cross section of cell wall and the hydride bed (Fig. 3.5) and their respective densities, assuming infinite cylindrical cells. By comparing results of Table 3.1 with those of Fig. 3.2, it can be concluded that the calculated mass ratios relate well with the observed rise of the outer wall temperature. The temperature does not increase in the 2-mm cell, the one with the highest ratio $M_{Cell\ wall}/M_{Hydride}$, whereas the corresponding lowest ratio in cell 3 leads to the highest temperature response.

Additionally, due to the low effective thermal conductivity, temperature profiles inside the bed should develop. Large beds would therefore have their maximal temperature at their centre.

The above outlined thermal effects explain the variance of the performances among the cells (Fig. 3.1). From the thermal and kinetics profiles in Figs. 3.1 and 3.2 it is noted that a rise in temperature improves the kinetics at the beginning of the process, when the first step of hydrogenation proceeds.

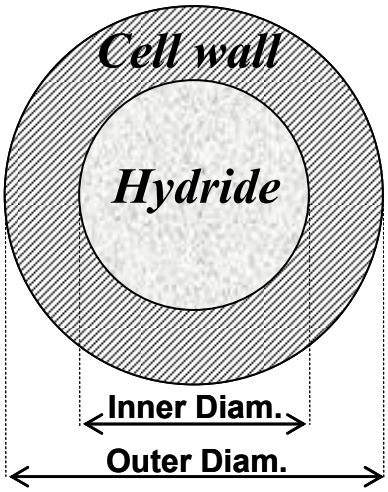

Figure 3.5: Cross-section of any cell used in the experiments

Table 3.1: Ratio of mass of cell wall to mass of hydride for the experimental cells. The density of the bed of material is 0.6 g ml^{-1} and the density of the walls of the cells is 7.85 g ml^{-1}.

Cell	Inner Diameter [mm]	Outer Diameter [mm]	$M_{Cell\ wall} / M_{material}$ [g g^{-1}]
1	2	8	196.3
2	4.5	8	28.3
3	10	15.2	17.1
4	15.2	25	22.3

Consequently, it improves the hydrogenation kinetics in the larger cells compared to the smaller cells. Indeed in cell 3, with the lowest ratio $M_{Cell\ wall}/M_{Hydride}$ and the highest rise in the outer wall temperature, the fastest kinetics for the first step is observed. Respectively, cell 1 having the highest ratio $M_{Cell\ wall}/M_{Hydride}$ presents no rise in temperature and the slowest kinetics for step one. Thus, the optimum temperature for kinetics is substantially higher than the initial temperature of 125 °C but should be lower than the equilibrium temperature at 100 bar for the first step of hydrogenation (Eq. 1.1), which amounts to about 250-260 °C.

At 100 bar, however, the equilibrium temperature for the second step of hydrogenation (Eq. 1.2) is around 170 °C. If the hydride reaches a temperature higher than 170 °C after the first step of reaction, the second step will not proceed until the temperature of the material has decreased significantly below that temperature. This would cause a delay between the two steps, and may explain the delays in Fig. 3.1 for the larger cell sizes. This conclusion is supported firstly by the hydrogen content of the

material during the delay, which amounts to around 1.6 wt% corresponds to the theoretical hydrogen capacity of the first step of hydrogenation, and secondly, by the observation that the time of the delay increases with the diameter of the cells.

In addition, the time dependence of the outer wall temperature of cell 3, in Fig. 3.2, reflects the delay between the steps. The temperature rises during the first step, almost 20 °C, and decreases when the first reaction is completed. At the end of the delay, the temperature increases once again. Both increments can be explained by the exothermic hydrogenation reactions. However, the absolute value of temperature rise on the outer wall of the cells does not explain the delay in the reaction, because the equilibrium temperature is neither reached nor exceeded. This indicates significantly higher temperatures in the hydride bed. Therefore, experiments with the thermocell were performed in which the temperature throughout the bed was monitored.

Figure 3.3b shows that as soon as the first absorption step starts, there is a small peak in temperature, which occurs quite shortly for some seconds and had not been detected from outer wall temperature measurements. It can be attributed to hydrogen heating up upon expansion and subsequent fast heat flow into the hydride. At the same time, the exothermic hydrogenation of NaH and Al occurs with fast kinetics, leading to a substantial increase of temperature in the powder bed. As expected, due to the limited heat conduction in the material, after about 1 minute a temperature profile develops with a maximum of 210 °C in the centre of the bed (position T1). This is still lower than the equilibrium temperature of step 1 (Eq. 1.1), which is 250-260 °C at the working pressure (100 bar), but much higher than the equilibrium temperature of step 2 (Eq. 1.2), 170 °C. Consequently, after absorbing 1.6 wt% of hydrogen, corresponding to the completion of step 1, hydrogenation does not continue. Therefore, temperatures in the bed decrease due to the heat flow through the cell wall and the surrounding air. It is observed that the second absorption step does not start at the point when the temperature falls below the equilibrium temperature of 170 °C. The temperature decreases to 140 °C and remains almost constant in the entire bed. Only after 2 minutes does further hydrogenation proceed; the temperature increases correspondingly again and a new temperature gradient develops throughout the bed. According to the slower kinetics of the second hydrogenation step, the temperature gradient is not as high as during the first step.

The delay between both absorption steps, labelled as section b in Fig. 3.3, cannot be entirely explained by the constraint related to the equilibrium temperature for the formation of $NaAlH_4$, since during the delay the temperature in the bed is at 140°C. This is 30 °C lower than the corresponding equilibrium temperature, and even at this temperature and 100 bar the material absorbs once again after its end, when section c in Fig. 3.3 starts. A possible cause is that heating of the material to high temperatures in the first absorption step has resulted in recovery processes of the material, which impede the nucleation of the $NaAlH_4$ phase. In order to support this explanation, the totally absorbed material was

desorbed at 125 °C and 5 bar. This results in the complete decomposition of $NaAlH_4$ into Na_3AlH_6 and Al with the respective release of hydrogen, because the equilibrium pressure for the further dehydrogenation is 3 bar. The material was then hydrogenated at different initial temperatures (100 °C, 125 °C, 140 °C and 150 °C) by applying 100 bar H_2. In order to start the absorption, the pressure increase in the cells using the experimental Sieverts apparatus is performed within less than a second. Interestingly, the reaction starts immediately, as shown in Fig. 3.6, accompanied by temperature increase. Consequently, the delay between the two steps has to be caused by the condition of Na_3AlH_6 or Al after the first hydrogenation step and can, for example, be unfavourable for the $NaAlH_4$ nucleation process.

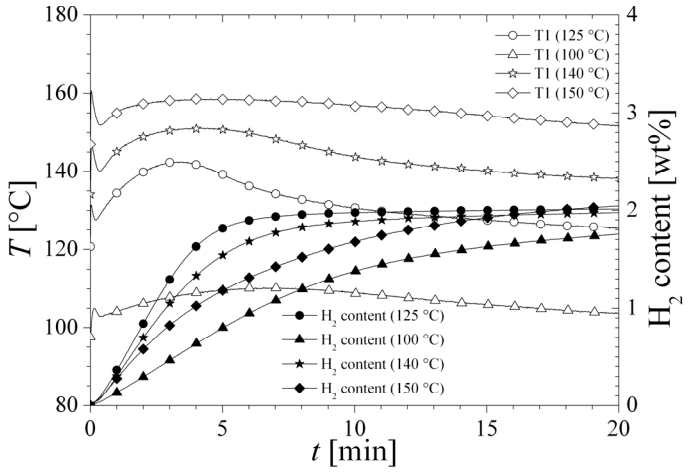

Figure 3.6: Absorptions of Na_3AlH_6/Al at 100 bar H_2, previously formed by desorption of $NaAlH_4$ at 5 bar and 125 °C. Initial temperatures of the absorptions are indicated for each curve (100, 125, 140 and 150 °C). T1 is the temperature in the centre of the hydride bed.

These findings are important for modelling, design and layout of a storage tank based on sodium alanate. It has to be noted that the observed significant heating upon hydrogenation of the cells can be avoided by efficient cooling using water or oil. Aspiring towards cost effectiveness, simple constructions, and the consequently large dimensions of the powder beds, however, will always result in strong temperature changes in the hydride as in this work. A possible approach to overcome the detrimental effect observed before the second absorption step would be to increase the cooling intensity for a short time after the first absorption step is completed.

Experiments were also done in the thermocell in order to estimate the thermal conductivity of the material. In order to evaluate the measurements, a homogeneous cylindrical system is assumed in a stationary process with only radial conduction, no axial conduction, and a constant and homogeneous

heat generation, as well as a constant density and heat conduction of the hydride bed. Heat convection is neglected. In this case a parabolic temperature profile is obtained by the standard heat conduction equation:

$$T - T_C = -\frac{\dot{q}\rho r^2}{4\lambda_{eff}} \tag{3.1}$$

where T is the temperature at a radial distance r from the centric axis of the cylinder, T_C the temperature in the axis (centre) of the cylinder, $\dot{q}$ the heat generation per unit of mass, ρ the density of the hydride bed, and λ_{eff} the effective thermal conductivity of the bed of material.

The effective thermal conductivity of the hydride during in-situ measurements is estimated using Eq. 3.1. For this estimation, a variable m is defined according to Eq. 3.2 below, such that Eq. 3.1 turns into Eq. 3.3.

$$m = -\frac{\dot{q}\rho}{4\lambda_{eff}} \tag{3.2}$$

$$T - T_C = mr^2 \tag{3.3}$$

First, m is numerically adjusted to the experimental set of data $T - T_C$ vs. r^2 taken during an endothermic or exothermic reaction in a moment with constant temperature profile ($\partial T/\partial t = 0$ inside the bed). After adjusting m, λ_{eff} is calculated by Eq. 3.2. As experimentally determined, a density of the bed in the desorbed state of about 0.6 g ml^{-1} was taken. $\dot{q}$ is calculated from the measured reaction rate and the enthalpy of reaction, derived from PcT-measurements.

$$\dot{q} = -r'' \Delta H_R \tag{3.4}$$

where r'' is the hydrogen sorption rate and ΔH_R is the enthalpy of reaction per mol of hydrogen.

The condition $\partial T/\partial t = 0$ inside the bed was not valid during most of the experiments, but it is clearly fulfilled after about 10 minutes during the desorptions of $NaAlH_4$ at 5 bar and 125 °C, as shown in Fig. 3.7. From the experimental temperature profiles and the desorption rate r'', m and $\dot{q}$ are calculated as above explained. The experimental and fitted temperature profile is presented in Fig. 3.8. The estimations of the effective thermal conductivity were done for the material without and with carbon addition as well as the mixtures with expanded graphite. At the moment of the estimation, the sodium alanate material is a mixture of $NaAlH_4$, Na_3AlH_6 and Al.

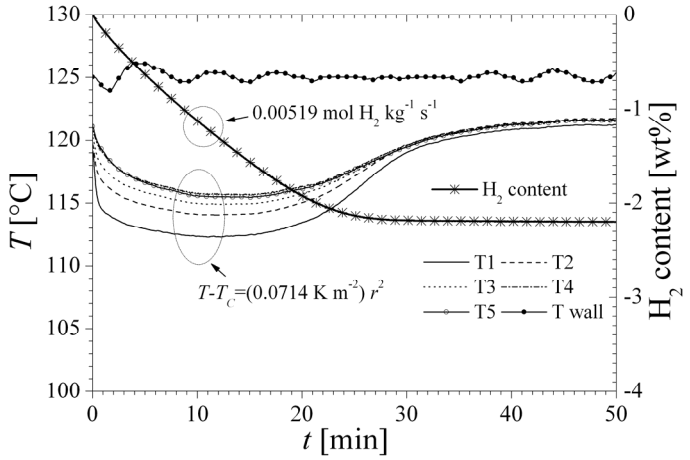

Figure 3.7: Desorption of $NaAlH_4$ at 5 bar and 125 °C in the thermocell. Initial temperature is 125 °C. For a reaction time of 10 min, the temperature profile was fitted and the desorption rate was calculated in order to estimate the effective thermal conductivity of the hydride bed.

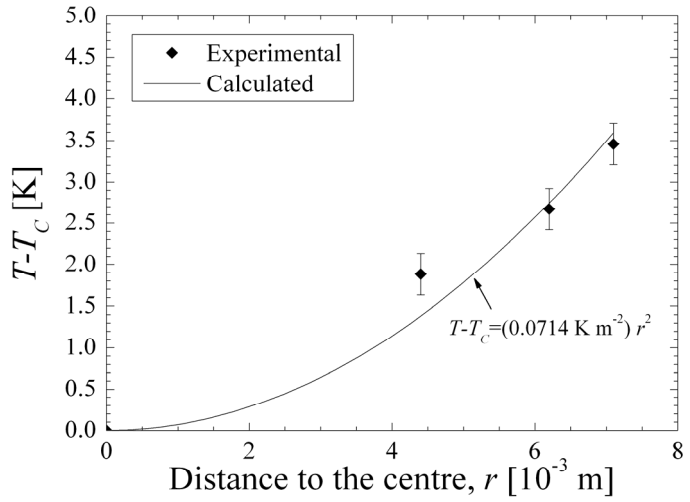

Figure 3.8: Example of temperature of the hydride bed with respect to the distance from the centre corresponding to the indicated data in Fig. 3.7. The fitting was used to estimate the effective thermal conductivity of the hydride bed.

The estimated thermal conductivities are summarized in Fig. 3.9 for material without and with carbon addition. The values obtained with these in-situ measurements for the material without carbon and the values reported in the literature from static measurements at 5 bar hydrogen pressure [41] are in very good agreement, and range between 0.5 and 0.6 W m^{-1} K^{-1}. The differences between the various

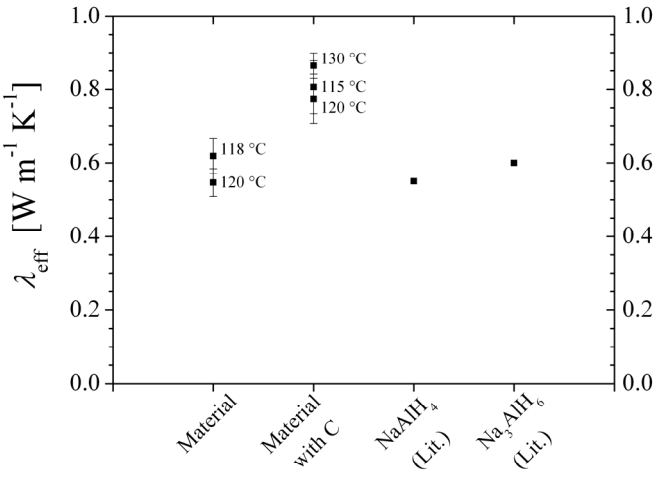

Figure 3.9: Estimated effective thermal conductivity of hydride bed for $NaAlH_4$ with and without carbon addition during desorption at 5 bar H_2 in comparison with literature near room temperature [41]. The temperatures reported are the mean temperatures of the hydride bed.

measurements are within the accuracy of the estimation. In the appendix, the error calculation for this estimation method for the effective thermal conductivity is shown.

The addition of carbon during milling leads to a roughly 50 % higher thermal conductivity, amounting to around 0.8 W m^{-1} K^{-1}. Nevertheless, the behaviour during the absorptions and desorptions is qualitatively the same as without carbon, both showing a significant delay between the two steps of reactions as shown in Fig. 3.10. However, carbon slightly improves the kinetics of both absorption and desorption. As carbon also acts as an effective milling lubricant, it was decided to continue further experiments of this investigation with the material preparation method including the addition of 5 wt% of carbon during the milling. Nevertheless, the improvement of hydrogenation kinetics and thermal conductivity by this carbon addition is still not sufficient for technical applications. Therefore, further investigations on the effective mechanisms in sodium alanate with carbon additions are of high interest.

Inspection of the sorption behaviour of the sodium alanate mixtures in the thermocell shown in Fig. 3.4 reveals achieved enhancement of the effective thermal conductivity by addition of EG. The enhancement of the thermal conductivity is deduced from the smaller temperature peaks and temperature profiles measured during the absorptions. For instance, the mixture with 5 wt% of EG leads to a maximal temperature peak of 160 °C, in contrast to the peak of almost 210 °C for the material without any EG. Besides, at higher content of EG, this temperature peak lowers and the

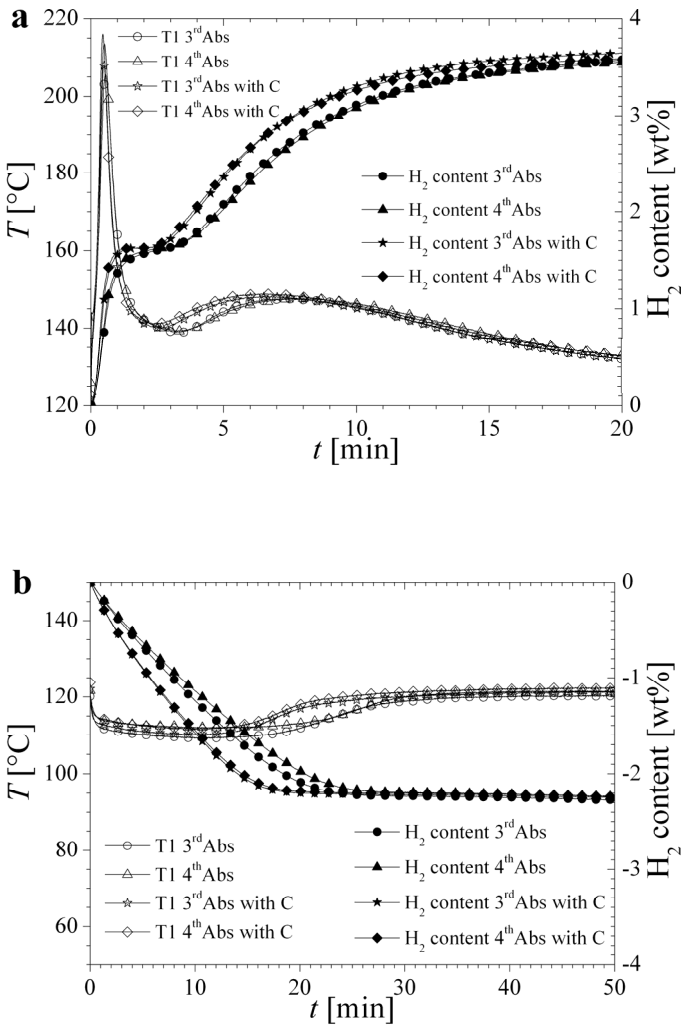

Figure 3.10: (a) Absorption measurements of the material at 100 bar with and without carbon. Initial temperature is 125 °C. (b) Desorption measurements of the material with and without carbon addition into vacuum. Initial temperature is 125 °C. T1 is the temperature in the centre of the bed. As noted also in other investigations, desorption kinetics at 125 °C for the second step is relatively slow. Therefore on the time scale in (b) only desorption of the first reaction step is visible.

temperature profile inside the bed decreases, as shown from Fig. 3.4a to 3.4d. This effect is mainly due to the enhancement of the effective thermal conductivity. In Fig. 3.11 the estimated thermal conductivities of the mixtures with EG flakes are presented. The mixture with 5 wt% of EG has an estimated thermal conductivity between 1.3 and 1.8 W m^{-1} K^{-1}, which almost doubles compared to the material without EG. Higher EG content in the hydride bed leads to higher values of the effective heat conductivity. Though, the estimation method is only appropriated for low values of thermal conductivity according to the error calculation (see error bars in Fig. 3.11 and the error calculation in

the appendix). At high values of the thermal conductivity (>2 W m^{-1} K^{-1}) the temperature profile developed for the estimation, as the one shown in Fig. 3.7, becomes quite narrow. Due to the error of the temperature measurement, the associated propagated error in the estimation turns really high. However, it is clear from both the narrow temperature profile and the lower peaks that the effective thermal conductivity increases at higher content of EG. In addition, besides the enhancement of the thermal conductivity, the EG in the hydride bed acts as an extra sink for the heat release during the absorption and thus reducing the heat generated in the hydride bed per unit of volume. Implementation of mixtures of sodium alanate with EG must be optimised in practical systems. On one hand the addition of inert expanded graphite enhances the effective thermal conductivity of the bed allowing larger bed sizes. On the other hand, it reduces the hydrogen capacity of the hydride bed. Later in Section 5.2 the optimisation of storage systems based on sodium alanate is analysed and discussed, evaluating the effect of the amount of expanded graphite among other parameters, like operating conditions and compaction of the material.

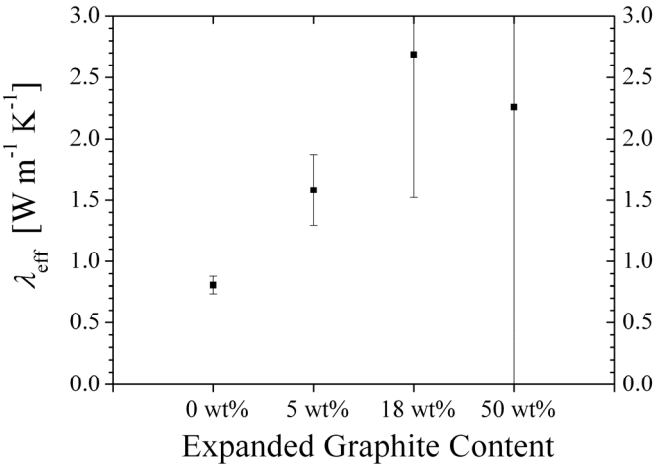

Figure 3.11: Estimated effective thermal conductivity of hydride bed of sodium alanate material mixed with different contents of EG. Measured under desorption at 5 bar in the thermocell.

3.2 Empirical kinetic model of sodium alanate reacting material: hydrogen absorption

Hydrogen storage systems based on metal hydrides require appropriate quantitative kinetic description for simulations and designs, in particular for the crucial absorption process. This section proposes an empirical kinetic model for the hydrogen absorption of sodium alanate material doped with

aluminium-reduced $TiCl_4$, as produced in kg-scale for this work. The model is based on kinetic data obtained by volumetric titration measurements performed on each of the two absorption steps of sodium alanate, within a range of experimental conditions varying from 10 bar to 110 bar and from 100 °C to 180 °C.

Previous kinetic models of the absorption of sodium alanate-based material are derived from experiments in which thermodynamic conditions for both absorption steps are possible [42, 43]. However, they assumed that the second step of hydrogenation occurs only after completion of the first step. Unlike these previous treatments, this investigation is based on the study of the individual absorption steps (as done similarly in [44]). A new approach is proposed for the mass balance of the reactions: one in which the material is described as a mixture composed of different type of reacting materials. This avoids the use of correction terms for the experimental capacities. The mass balance is also validated with experiments in which both absorption steps can occur simultaneously. This kinetic model is planned to be implemented later in this work for numerical simulations of hydrogen storage systems based on sodium alanate, Section 4.2 and 5.2.

3.2.1 Kinetic equations

The reacting system is modelled as two consecutive absorption steps and only their net rate of reaction is considered. Equations 3.5 and 3.6 define the stoichiometry of the first and second absorption steps, respectively. Equation 3.5 includes the additional aluminium and hydrogen required for the second absorption step, Eq. 3.6.

$$3NaH + 3Al + 4.5H_2 \rightarrow Na_3AlH_6 + 2Al + 3H_2 \tag{3.5}$$

$$Na_3AlH_6 + 2Al + 3H_2 \rightarrow 3NaAlH_4 \tag{3.6}$$

Three mixtures of defined composition are used to describe the reacting system (Tang et al. [43] proposed a similar definition)

$$S_I = 3NaH + 3Al + 4.5H_2 \tag{3.7}$$

$$S_{II} = Na_3AlH_6 + 2Al + 3H_2 \tag{3.8}$$

$$S_{III} = 3NaAlH_4 \tag{3.9}$$

Thus, Eq. 3.5 corresponds to

$$S_I \rightarrow S_{II} \tag{3.10}$$

and Eq. 3.6 to

$$S_{II} \rightarrow S_{III} \tag{3.11}$$

The transformed fraction α will be used to follow the progress of the absorption steps and is individually considered for each step. It corresponds, among other possible relations, to the ratio of the

mass of hydrogen that has been absorbed, m_{H_2}, to the maximal mass of hydrogen that can be absorbed, $m_{H_2,\max}$, Eq. 3.12. Equations 3.13 and 3.14 present an equivalent definition for each absorption step in terms of the masses of the mixtures of defined composition.

$$\alpha = \frac{m_{\mathrm{H_2}}}{m_{\mathrm{H_2,max}}} \tag{3.12}$$

$$\alpha_{\mathrm{S_I \rightarrow S_{II}}} = \frac{m_{\mathrm{S_{II}}}}{m_{\mathrm{S_I}} + m_{\mathrm{S_{II}}}} \tag{3.13}$$

$$\alpha_{\mathrm{S_{II} \rightarrow S_{III}}} = \frac{m_{\mathrm{S_{III}}}}{m_{\mathrm{S_{II}}} + m_{\mathrm{S_{III}}}} \tag{3.14}$$

The net rate of reaction of each absorption step is defined in terms of the transformed fraction:

$$\frac{d\alpha}{dt} = k(T,p)g(\alpha) \tag{3.15}$$

The underlying kinetic processes of the absorption, and specially the rate-limiting process, determine the net rate of reaction and consequently the function $g(\alpha)$. In this investigation the function $g(\alpha)$ is empirically determined by comparing the transformed fraction during the experiments with the value predicted by the integrated equation of different kinetic models, Table 3.2. The model equation with best-fit results defines the most appropriate function $g(\alpha)$. Rudman [45] and Barkhordarian et al. [46] discuss a detailed explanation about the applied models and the phenomenology behind them.

The rate constant k in Eq. 3.15 is a function of the temperature and the applied hydrogen pressure:

$$k(T,p) = \left(Ae^{-\frac{E_a}{RT}} \right) f(p, p_{eq}) \tag{3.16}$$

The first factor of Eq. 3.16 is the Arrhenius formula, while the second factor reflects the influence of the equilibrium and applied pressure on the net rate of reaction. This influence is a consequence of the reversible character of the reaction. The factor $f(p, p_{eq})$ acts as the driving force of the absorption, which depends on the deviation of p from p_{eq}. In this work, the factor $f(p, p_{eq})$ is defined by trying different functions and selecting the one that best fits the experimental data. Some of the considered functions are $\ln(p/p_{eq})$ (since it defines the change of hydrogen chemical potential of the sorption process), $(p - p_{eq})/p_{eq}$ (a first order approximation of the logarithm based on its Taylor series), and combinations of them. However, other empirical functions may be also tried for the factor $f(p, p_{eq})$.

Table 3.2: Kinetic models used for fitting the function $g(\alpha)$ to experimental absorption data (see Eq. 3.15)

Model (and possible mechanism)	$g(\alpha)$	**Integrated equation**
Surface controlled	1	$\alpha = kt$
Johnson-Mehl-Avrami (JMA) general equation	$n(1-\alpha)\{\ln[1/(1-\alpha)]\}^{(n-1)/n}$	$[-\ln(1-\alpha)]^{1/n} = kt$
JMA, $n = 3$ (e.g. three-dimensional growth of existing nuclei with constant interface velocity)	$3(1-\alpha)\{\ln[1/(1-\alpha)]\}^{2/3}$	$[-\ln(1-\alpha)]^{1/3} = kt$
JMA, $n = 2$ (e.g. two-dimensional growth of existing nuclei with constant interface velocity)	$2(1-\alpha)\{\ln[1/(1-\alpha)]\}^{1/2}$	$[-\ln(1-\alpha)]^{1/2} = kt$
JMA, $n = 1$ (e.g. one-dimensional growth of existing nuclei with constant interface velocity)	$(1-\alpha)$	$-\ln(1-\alpha) = kt$
Contracting Volume (CV) (e.g. contracting volume, three-dimensional growth with constant interface velocity)	$3(1-\alpha)^{2/3}$	$1-(1-\alpha)^{1/3} = kt$
CV (e.g. contracting volume, two-dimensional growth with constant interface velocity)	$2(1-\alpha)^{1/2}$	$1-(1-\alpha)^{1/2} = kt$
CV (e.g. contracting volume, three dimensional growth diffusion controlled with decreasing interface velocity)	$3/2\left[(1-\alpha)^{-1/3}-1\right]^{-1}$	$1-(2\alpha/3)-(1-\alpha)^{2/3} = kt$

The procedure to obtain the parameters A, E_a, and the functions $g(\alpha)$ and $f(p, p_{eq})$, from experimental data is as follows:

1. The function $g(\alpha)$ is determined by fitting the experimental data to the integrated equations of the models in Table 3.2. The model with best-fit results defines $g(\alpha)$. The experiments must be performed isothermal and isobaric.

2. After a model has been found to define function $g(\alpha)$, the values of the rate constant k for each experiment are determined, i.e. $k(T, p)$

3. A function for the factor $f(p, p_{eq})$ is assumed. The parameters A and E_a are calculated using the experimental values of k by fitting $\ln[k/f(p, p_{eq})]$ vs. $1/T$ (see Eq. 3.16). In a next step, the correlation fit is evaluated and $\ln(k/\{A\exp[-Ea/(RT)]\})$ vs. $f(p, p_{eq})$ is plotted. A perfect fitting of the later relation is a line that crosses the origin and has a slope equal to 1.

4. Other functions $f(p, p_{eq})$ should be considered and the correlation of the plots mentioned in step 3 of this procedure is compared. The function with best results is the one that best describes the kinetics.

3.2.2 Experimental approach

Experimental sorption kinetics was characterized using the Sieverts' apparatus. A cylindrical sample cell of 2 mm diameter was utilized, see Fig. 2.1. During all the experiments the temperature on the outer wall of the cell was measured. The mass of material in the cell was between 40 mg and 50 mg in each of the experiments.

To study the reaction kinetics of each absorption step individually, pressure-temperature (p-T) pairs for the initial and final states were chosen such that only one reaction step took place. The measurements were performed with both initial and final states being at the same temperature. At time $t = 0$ of the experiment the initial pressure was raised stepwise to the pressure of the final state. Figure 3.12 shows the thermodynamic stable states of the reacting system according to p-T conditions. The equilibrium lines are calculated using the van 't Hoff equation and the parameters presented in Table 1.1.

Table 3.3 summarizes initial and final conditions used to study each of the two absorption steps. All the experimental results for the kinetic analysis correspond to measurements of material that had been absorbed and desorbed at least 3 times, after which the material shows reproducible kinetics with respect to cycling.

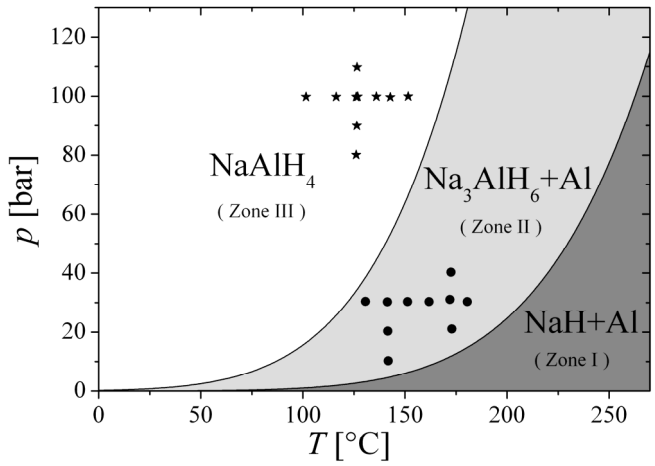

Figure 3.12: p-T diagram presenting the most stable state of the sodium alanate reacting system under H_2 pressure. At p-T conditions inside zones I, II and III, NaH+Al, Na_3AlH_6+Al, and $NaAlH_4$, respectively, are the most stable states. The circles (●) and the stars (★) correspond to p-T conditions for experiments for the first and second absorption steps, respectively.

Table 3.3: Location of the initial and final states for the absorption experiments according to the zones on Fig. 3.12.

Absorption step	**Reaction**	**Initial State**	**Final State**
First	$3NaH + 3Al + 4.5H_2 \rightarrow Na_3AlH_6 + 2Al + 3H_2$	Zone I	Zone II
Second	$Na_3AlH_6 + 2Al + 3H_2 \rightarrow 3NaAlH_4$	Zone II	Zone III

3.2.3 Isobaric and isothermal conditions during measurements

Both pressure and temperature during kinetic measurements must remain constant according to the quantitative analysis presented. If neither this issue nor the effects of the heat flow and mass flow are taken into account, kinetic analyses could be invalid and lead to wrong conclusions about the intrinsic kinetics, as shown in Section 3.1.

The Sieverts' type apparatus uses the change of the hydrogen pressure to follow the extent of the sorption reactions. Therefore, isobaric experiments are impossible to perform with this equipment [32]. To minimize this pressure change and maintain good resolution in the results, the apparatus worked with high gaseous reference volumes. The highest pressure change during the absorption measurements was -0.25 bar, while the pressure level is between 10 and 100 bar. The pressure used in the analysis was the arithmetic mean during each experiment.

Because of the high enthalpy of reaction of the investigated system, isothermal conditions cannot be perfectly maintained. It was shown in Section 3.1 that especially in larger cells sorptions lead to significant changes of temperature of the reacting material during the process. To minimize the temperature increase or decrease, the kinetic measurements were done in a 2-mm cell, which maintains almost isothermal behaviour: finite element simulations of the sorption process in the 2-mm cell demonstrated that the temperature increase of the material is lower than 1 K under the conditions and rates obtained in the experiments. Figure 3.13 shows the results of the simulation of a hydrogenation of totally desorbed material at 100 bar and 125 °C. Under these conditions, the process has a high rate of reaction and, therefore, high rate of heat release and temperature increase are expected. The simulation of the bed of material applied the standard equation of heat conduction with a heat source, Eq. 3.17.

$$c_{p,b}\rho_b \frac{\partial T}{\partial t} = \lambda_b \nabla^2 T - r'' \rho_b \Delta \mathrm{H_R} \tag{3.17}$$

The heat source is calculated from the experimental hydrogen sorption rate per mass of reacting material, the bulk density and the enthalpy of reaction derived from PcT-measurements (see Table 1.1). The heat conduction through the cell wall was simulated with the equation of heat conduction without any heat source term. The surface temperature of the cell wall had a constant temperature of 125 °C as it was measured during the experiments. The properties of the bed of material are as follows: density: 0.55 g ml^{-1} (experimental), heat capacity: 1075 J kg^{-1} K^{-1} [41], and thermal conductivity: 0.5 W m^{-1} K^{-1} [35]. The cell walls are made of stainless steel with a density of 7.9 g ml^{-1}, a heat capacity of 500 J kg^{-1} K^{-1}, and a thermal conductivity of 15 W m^{-1} K^{-1} [47]. The sensible heat of the gaseous phase and the kinetic energy of the incoming hydrogen were neglected. Chapter 4 presents a detailed explanation of finite element simulations of hydrogen absorption process with sodium alanate.

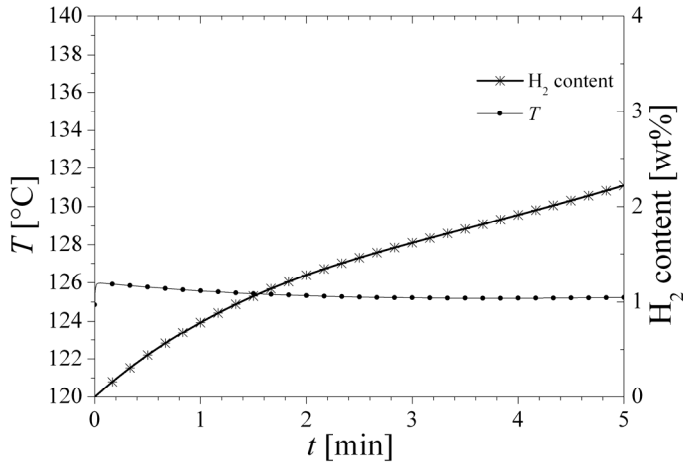

Figure 3.13: Simulated temperature development inside the 2-mm cell during an experimental absorption at 100 bar. Initial temperature is 125 °C. T is the temperature in the centre of the bed of reacting material.

3.2.4 Hydrogen absorption of NaH+Al to form Na_3AlH_6: $S_I \rightarrow S_{II}$

The absorption experiments were done at p-T pairs with starting state within zone I and final state within zone II according to Fig. 3.12. To guarantee the starting state of the material within zone I, desorptions with final conditions within zone I were done until the material was fully desorbed. Afterwards, the material was put under vacuum at 180 °C for one hour. In this investigation, the transformed fraction $\alpha_{S_I \rightarrow S_{II}}$ considers only the active absorbing material and it is referred to the total hydrogen absorbed in each experiment after completion and therefore goes always from 0 to 1. The experimental hydrogen capacity of the absorption experiments was between 1.5 and 1.6 wt%, which corresponds to 88 and 94 %, respectively, of the theoretical capacity of 1.7 wt% of the first absorption step for the mixture of this investigation. The capacities are calculated based on the desorbed material including all inert species (catalysts and additional carbon).

The effect of temperature on the rate of reaction at constant pressure is shown in Fig. 3.14, which presents hydrogen absorption curves at 30 bar and temperatures between 130 °C and 180 °C. Clearly, the rate of absorption increased from 130 °C to 170 °C. At 180 °C, however, only a slight increase in the reaction rate is observed as compared to 170 °C. The equilibrium temperature at 30 bar for the first absorption step corresponds to 208 °C according to Eq. 1.3 (see also Fig. 3.12). As the temperature for the absorption experiments gets close to this equilibrium value, the rate of reaction should decrease and therefore there is a temperature before equilibrium showing the maximum rate of absorption.

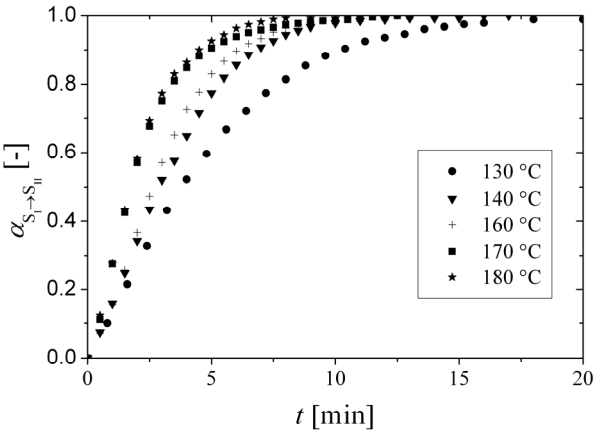

Figure 3.14: Hydrogen absorptions of NaH+Al at 30 bar and temperatures between 130 °C and 180 °C. The transformed fraction is normalized to the total mass of hydrogen absorbed in each experiment after completion.

According to the results at 30 bar, the temperature of the maximum rate of absorption should be in the vicinity of 170 °C and 180 °C. This value will later be compared in subsection 3.2.6.1 by means of the derived analytical expression of the kinetics model.

Absorption curves measured at 140 °C and pressures between 10 bar and 30 bar are shown in Fig. 3.15. At 10 bar it is already possible to reach 40 % of the hydrogen capacity of the first step of absorption after only 20 minutes. After 2 hours, the absorption is almost complete. By increasing the pressure at the same temperature, the rate of absorption gets significantly faster. At 20 bar, the time to absorb 90 % of the hydrogen capacity is reduced to less than 15 minutes, and at 30 bar it is reduced to 7 minutes only.

3.2.5 Hydrogen absorption of Na_3AlH_6+Al to form $NaAlH_4$: $S_{II} \rightarrow S_{III}$

The experiments for this absorption step had p-T starting state within zone II and final state within zone III according to Fig. 3.12. Desorptions with final conditions within zone II guaranteed the starting state of the material. They lasted until the expected hydrogen capacity was reached. As done for the first absorption step, the reported transformed fraction $\alpha_{S_{II} \rightarrow S_{III}}$ considers only the active absorbing material during each experiment and therefore goes always from 0 to 1. The experimental hydrogen capacity of the material for this absorption step was between 2.2 and 2.3 wt%.

Figure 3.16 shows the effect of temperature on the rate of reaction at constant pressure for hydrogen absorptions at 100 bar and temperatures between 100 °C and 150 °C. The behaviour is similar to the

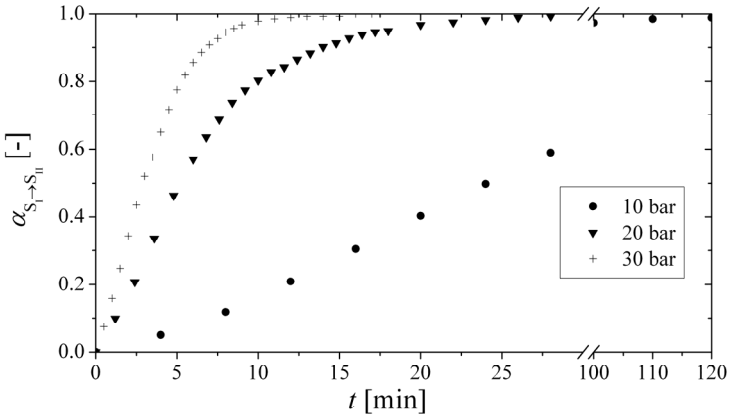

Figure 3.15: Hydrogen absorptions of NaH+Al at 140 °C and pressures between 10 bar and 30 bar.

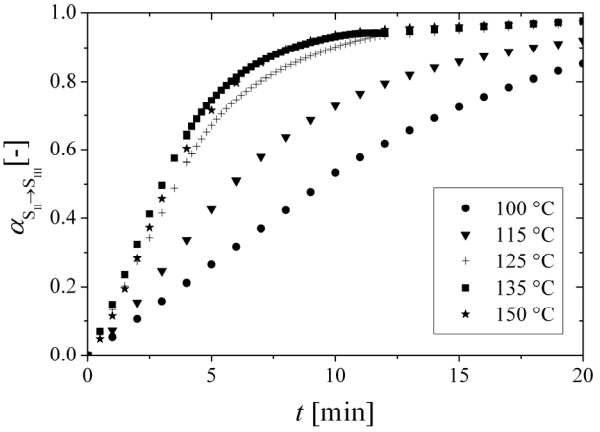

Figure 3.16: Hydrogen absorptions of Na_3AlH_6+Al at 100 bar and temperatures between 100 °C and 150 °C. The transformed fraction is normalized to the total mass of hydrogen absorbed in each experiment after completion

first absorption step: the rate of absorption increased from 100 °C to 135 °C, but at 150 °C, however, there is a slight decrease in the reaction rate. The equilibrium temperature for this absorption step is 169 °C at 100 bar according to Eq. 1.3. At 100 bar, the maximum rate of absorption should be close to 135 °C and 150 °C.

Figure 3.17 shows absorption results at 125 °C and pressures in the range of 80 bar to 110 bar. The effect of pressure is clear, improving the rate of reaction by increasing the driving force. At 125 °C and 110 bar it is possible to absorb 90 % of the hydrogen capacity within 7 minutes.

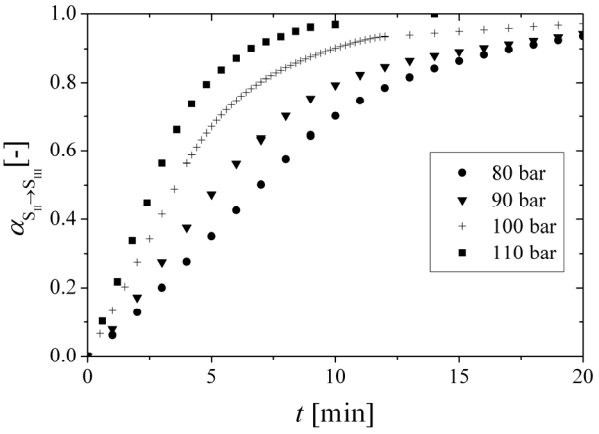

Figure 3.17: Hydrogen absorptions of Na_3AlH_6+Al at 125 °C and pressures between 80 bar and 110 bar.

3.2.6 Discussion

3.2.6.1 Hydrogen absorption of NaH+Al to form Na_3AlH_6: $S_I \rightarrow S_{II}$

The rate of the first absorption step was fitted to the experimental measurements shown in subsection 3.2.4 by applying the procedure explained in subsection 3.2.1. The rate of absorption is best described by the JMA model with n =1.33.

$$\frac{d\alpha_{S_I\rightarrow S_{II}}}{dt} = 1.33 k_{S_I\rightarrow S_{II}} \left(1-\alpha_{S_I\rightarrow S_{II}}\right)\left\{\ln\left(\frac{1}{1-\alpha}\right)\right\}^{0.25} \tag{3.18}$$

Following the procedure, the constant $k_{S_I\rightarrow S_{II}}$ is determined for each experiment. Based on these values, further fitting of Eq. 3.16 led to the function

$$f_{S_I\rightarrow S_{II}}(p, p_{eq}) = \left(p - p_{eq}\right)/p_{eq} \tag{3.19}$$

with Arrhenius parameters A=2.28×10^8 s^{-1} and E_a=91.7 kJ mol^{-1}. Figure 3.18 shows the results of the fitting of the experimental data with these function and parameters.

The exponent value n=1.33 may suggest spatial or temporal superposition of transformation mechanisms. For instance, it could be superposition of two and three dimensional growth of constant number of nuclei at a diffusion controlled transformation. The JMA equation with exponent value n=1.33 for this absorption step is similar to the kinetic model in [44, 48], which reported an empirical equation for this absorption step using the JMA equation with n =1.4 and n=1. Kircher and Fichtner

[49] applied also the JMA equation to the first absorption step, reporting values of n varying between 0.7 to 0.8 depending on the sample preparation method.

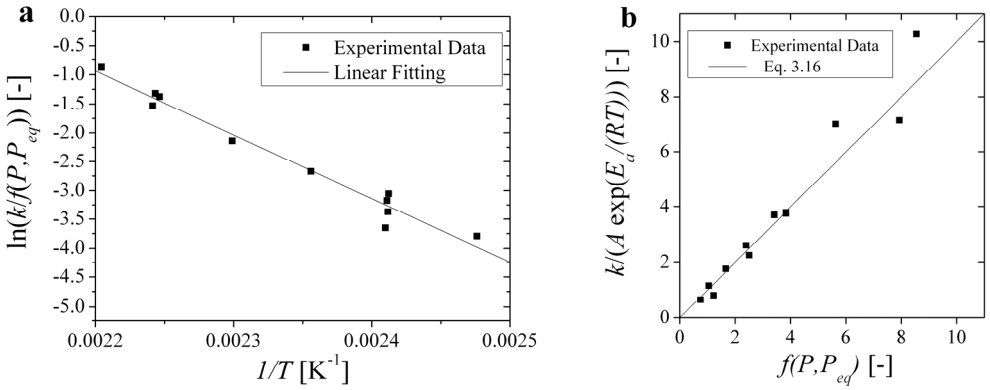

Figure 3.18: Kinetic fitting of the absorption of NaH+Al to Na_3AlH_6. Equation 3.16 defines the fitting relation. The parameters A and E_a in the right diagram (b) come from the fitting in the left diagram (a) (A =2.28 10×8 s^{-1} and E_a =91.7 kJ mol^{-1}).

To complement the analysis, the rate constant $k_{S_I \rightarrow S_{II}}$ is calculated and extrapolated for several p-T conditions by using Eq. 3.16 and parameters of the fitting, and presented in Fig. 3.19. At conditions with pressures lower than the equilibrium pressure of the first absorption step, NaH+Al should not absorb hydrogen and therefore the rate constant for the absorption is set to 0. The constant rate lines of the contour demonstrate that by changing the conditions it is possible to have the same rate of reaction at different temperatures by decreasing the pressure, e.g. the absorption at 120 °C and 40 bar and at 154 °C and 20 bar. The contour also indicates that for every pressure there is a maximum value of the rate of reaction and there are also two temperatures that have the same rate of reaction. One of them is lower than the temperature of the maximum rate of reaction. The second one is higher but still lower than the corresponding equilibrium temperature. The temperature of maximum rate of reaction can be analytically deduced by combining Eqs. 3.16 and 3.19:

$$T_{Opt} = \frac{-\Delta H_R}{R\left[\ln\left(\frac{E_a}{E_a + \Delta H_R}\right) - \ln\left(\frac{P}{1\,bar}\right)\right] - \Delta S_R} \tag{3.20}$$

Equation 3.20 has utility when defining optimal process conditions for hydrogen absorptions. The dotted line on Fig. 3.19 shows the calculated points of maximum rate of reaction for every pressure. At 30 bar, the optimal temperature corresponds to 180 °C and confirms the experimental results in Fig.

3.14. Also, because the contour lines are becoming vertical, it is concluded that the effect of pressure on the rate of reaction is low when p-T conditions are far from the optimal conditions line. Under conditions close to this line, however, the contour lines become horizontal and the effect of the pressure on the rate of reaction is thus the highest. When applying the same analysis to the effect of the temperature on the rate of reaction, it is concluded that far away from the optimal conditions line, the effect of temperature is great, while at the optimal conditions line its effect is the least.

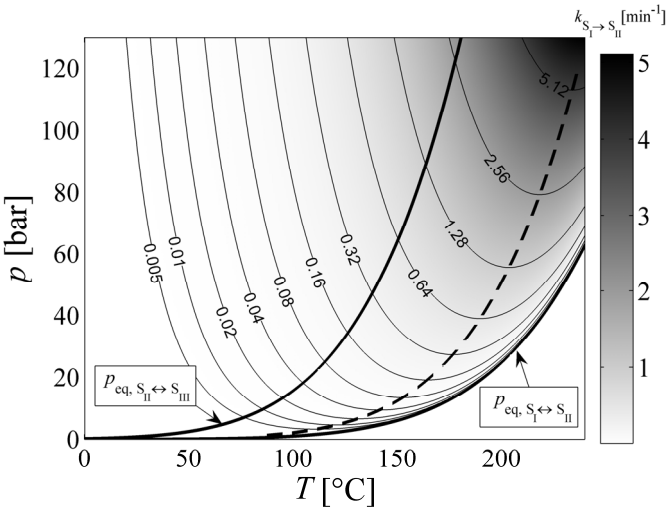

Figure 3.19: Calculated values of the rate constant $k_{S_I \rightarrow S_{II}}$ as a function of pressure and temperature. The lines are contour lines of values having the same rate constant. The dotted line represents the calculated points of maximum rate of reaction for every pressure.

3.2.6.2 Hydrogen absorption of Na_3AlH_6+Al to form $NaAlH_4$: $S_{II} \rightarrow S_{III}$

For this absorption step the experiments yielded a hydrogen capacity of 2.3 wt%, which corresponds to 68 % of the theoretical capacity of 3.4 wt% of the second absorption step. The reduction of the capacity is explained by the inhomogeneous distribution of the reacting solid phases [25, 42] and the consumption of aluminium while reacting with titanium (catalyst) [50]. The inhomogeneous distribution of NaH and Al for the formation of Na_3AlH_6 during the hydrogen absorption, Eq. 1.1, leads to the first inefficiency of the process. Later, during the hydrogenation of Na_3AlH_6+Al, Eq. 1.2, some Na_3AlH_6 does not react further with Al and acts as inert species for this reaction. If an efficiency of 94 % for the first absorption step is considered, the efficiency of the second absorption step becomes 72 %. The aluminium in excess for the first absorption step, which is actually required for the second absorption step, explains the higher efficiency of this first step.

As for the first absorption step, the JMA model with n =1.33 describes the rate of the second absorption step.

$$\frac{d\alpha_{S_{II}\rightarrow S_{III}}}{dt} = 1.33 k_{S_{II}\rightarrow S_{III}} \left(1-\alpha_{S_{II}\rightarrow S_{III}}\right)\left\{\ln\left(\frac{1}{1-\alpha}\right)\right\}^{0.25} \tag{3.21}$$

The fitting procedure of the constant $k_{S_{II}\rightarrow S_{III}}$ of each experiment led to the function

$$f_{S_{II}\rightarrow S_{III}}(p, p_{eq}) = \left(p - p_{eq}\right)/p_{eq} \tag{3.22}$$

The fitted Arrhenius parameters are A=1.52×10^9 s^{-1} and E_a=91.5 kJ mol^{-1}. Franzen [44] and Na Ranong et al. [48] also found that the second absorption step could be fitted with an empirical equation using the JMA equation with the same orders n =1.4 and n=1 as they found for the first absorption step. Kircher and Fichtner [49] reported a JMA order n of 1.1 and 1.4 for this second absorption step (depending on the sample preparation method).

The p-T diagram on Fig. 3.20 shows the calculated and extrapolated values of the rate constant $k_{S_{II}\rightarrow S_{III}}$. When the applied pressure is lower than the equilibrium pressure of the second absorption step, the rate constant is set to 0. Moreover, if the pressure is even lower than the equilibrium pressure of the first absorption step, Na_3AlH_6 should desorb hydrogen and form NaH+Al. These conditions are, however, of no interest for the present analysis. The possible zone for the absorption of the second step is smaller than for the first one and therefore the conditions of the second step of reaction will have stronger influence on the operation when it is desired to work with both steps simultaneously. Compared to the first absorption step, the second step is slower under the same applied conditions. The contour lines of constant reaction rate illustrate the possibility to obtain the same rate of reaction at different temperatures and pressures e.g. the absorption at 120 °C and 100 bar and at 155 °C and 90 bar. The dotted line on Fig. 3.20, plotted according to Eq. 3.20, shows the points of maximum rate of reaction for every pressure. At 100 bar the optimum temperature corresponds to 147 °C, which reflects the result obtained in the experimental measurements given in Fig. 3.16.

3.2.6.3 Empirical kinetic model and validation

The combination of both absorption steps as a model of two consecutive reactions describes the process when the steps can proceed one after the other and simultaneously because of thermodynamic conditions. This is the case when changing conditions from zone I to zone III of Fig. 3.12. As soon as NaH+Al is hydrogenated to Na_3AlH_6, Na_3AlH_6+Al can react further with hydrogen to form $NaAlH_4$.

The combination of Eqs. 3.10 and 3.11 defines the reacting system:

$$S_I \xrightarrow{r_{a1}} S_{II} \xrightarrow{r_{a2}} S_{III} \tag{3.23}$$

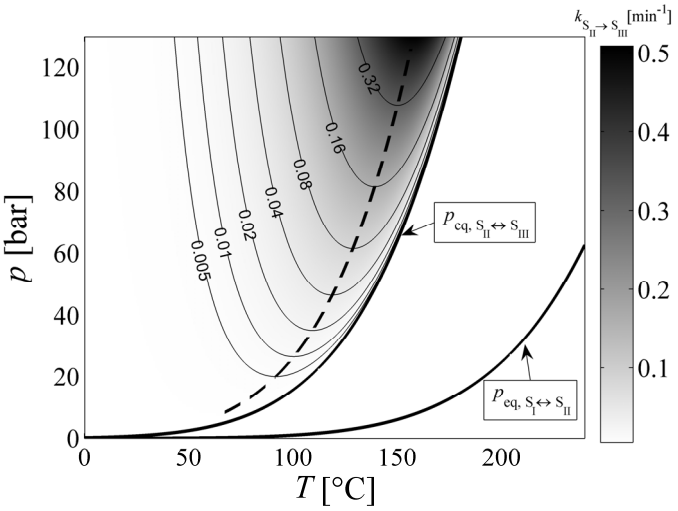

Figure 3.20: Calculated values of the rate constant $k_{S_{II}\rightarrow S_{III}}$ as a function of pressure and temperature. The lines are contour lines of values having the same rate constant. The dotted line represents the calculated points of maximum rate of reaction for every pressure.

The mass balance of the two consecutive reactions is summarized in the following equations:

$$\frac{dm_{S_I}}{dt} = -r_{a1} \tag{3.24}$$

$$\frac{dm_{S_{II}}}{dt} = r_{a1} - r_{a2} \tag{3.25}$$

$$\frac{dm_{S_{III}}}{dt} = r_{a2} \tag{3.26}$$

Thus, the use of this mass balance avoids the approximation of considering that the second absorption starts only after the first one is completed or the use of empirical correlations for the mass balance. The instantaneous rates of reaction in terms of masses are derived based on the kinetic equations when each absorption step independently occurs, Eqs. 3.18 and 3.21. Under this condition the total mass of the reacting system $m_{S_I} + m_{S_{II}}$ and $m_{S_{II}} + m_{S_{III}}$ is constant during the first and second absorption steps, respectively.

From Eqs. 3.12-3.14, 3.18 and 3.24-3.26, the instantaneous rate of the first absorption step in term of masses becomes

$$r_{a1} = 1.33 k_{S_I\rightarrow S_{II}} m_{S_I} \left\{ \ln\left(\frac{m_{S_I} + m_{S_{II}}}{m_{S_I}} \right) \right\}^{0.25} \tag{3.27}$$

and correspondingly the instantaneous rate of the second absorption step:

$$r_{a2} = 1.33 k_{S_{II} \rightarrow S_{III}} m_{S_{II}} \left\{ \ln\left(\frac{m_{S_{II}} + m_{S_{III}}}{m_{S_{II}}} \right) \right\}^{0.25} \tag{3.28}$$

Finally, the model considers that a mixture of three types of material composes the reacting system:

1. Material that can form NaH+Al, Na_3AlH_6 and $NaAlH_4$.
2. Material that can form NaH+Al and Na_3AlH_6 but not $NaAlH_4$. (inert material for the second absorption step)
3. Material that does not react at all (inert material for both absorption steps)

This new approach for the material balance eliminates the use of artificial terms in the kinetic equations to limit the capacities to the experimentally obtained ones as it is done in other kinetic models for sodium alanate [42-44, 48]. The ratios of these materials are based on the stoichiometry of the system and on the achieved experimental hydrogen capacities. Table 3.4 shows the mass composition of the material used in this investigation. These mass fractions are calculated based on the masses of the initial raw materials, the measured experimental hydrogen capacities and the stoichiometry of the system (Eqs. 1.1 and 1.2).

Figure 3.21 presents some calculated absorption curves based on the presented kinetic model under various operating conditions. To validate the model, the figure also shows the respective experimental results. It can be seen from the figure that the model reflects the experimentally determined data accurately. This validation, which complements the presented results of the individual absorption steps, ensures reliability of the presented fitting procedure and the empirical kinetic model. The model can be numerically implemented for simulations, designs and evaluations of hydrogen storage systems based on sodium alanate material as produced in this work. The proposed fitting procedure and material balance is also suitable for the development of empirical kinetic models for other metal hydride systems.

Table 3.4: Mass composition of the different type of materials according to experimental results.

Type of Material	Mass fraction in the initial mixture [-]
Active material for both absorption steps	0.58
Active material for the first absorption step only	0.23
Inert material	0.19

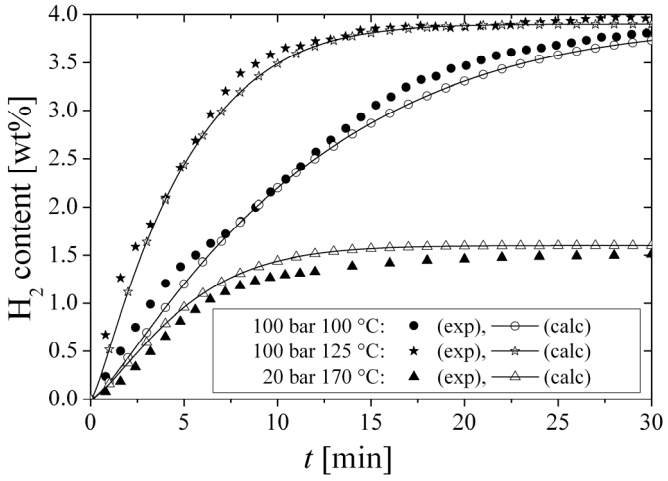

Figure 3.21: Experimental and calculated absorptions of totally desorbed sodium alanate material at different conditions.

3.3 Empirical kinetic model of sodium alanate reacting material: hydrogen desorption

This section presents an analogous empirical kinetic model for the two-step hydrogen desorption of sodium alanate material as produced in this investigation. The model is based on kinetic data obtained by volumetric titration measurements within a range of experimental conditions varying from 0 bar to 35 bar and from 100 °C to 190 °C. This section complements the model presented in Section 3.2 of the corresponding hydrogen absorption of sodium alanate material.

Previous experimental investigations determined kinetic expressions for the desorption steps of sodium alanate doped with $TiCl_3$ [42, 51], Ti_{13}·6THF [52], $Ti(OBu^n)_4$ and $Zr(OBu^n)_4$ [53]. They mainly focused on the determination of the energy of activation of the Arrhenius equation. However, the hydrogen back-pressure in the desorptions and its effect on the kinetics are not reported in most of these investigations [51-53]. Luo ang Gross [42] studied the effect of hydrogen back-pressure up to 3 bar, Bellosta von Colbe went up to 3.75 bar [54]. This section proposes an empirical kinetic model supported on experimental desorptions carried out at temperatures from 100 °C to 190 °C under hydrogen back-pressures from 0 bar up to 35 bar. This interval includes conditions which appear in the operation of practical applications and at which so far no previous measurements were reported. The utilized approach allows the independent study of each desorption step of sodium alanate material. The obtained empirical kinetic equations consider the effect of the temperature and hydrogen back-pressure as well as the transformed fraction of the material.

3.3.1 Kinetic equations

In an analogous way as previously done in Section 3.2 on hydrogen absorption, the kinetic equations of the model are presented for the case of hydrogen desorption. The model consists of two consecutive desorption steps, and only their net rate of reaction is considered. Equations 3.29 and 3.30 define the stoichiometry of the first and second desorption steps, respectively. Equation 3.30 includes the additional aluminium and hydrogen produced in the first desorption step.

$$3NaAlH_4 \rightarrow Na_3AlH_6 + 2Al + 3H_2 \tag{3.29}$$

$$Na_3AlH_6 + 2Al + 3H_2 \rightarrow 3NaH + 3Al + 4.5H_2 \tag{3.30}$$

By using the mixtures of defined composition in Eqs. 3.7-3.9, Eqs. 3.29 and 3.30 correspond to Eqs. 3.31 and 3.32, respectively:

$$S_{III} \rightarrow S_{II} \tag{3.31}$$

$$S_{II} \rightarrow S_{I} \tag{3.32}$$

Equations 3.33 and 3.34 present an equivalent definition for each desorption step in terms of the masses of the mixtures of defined composition.

$$\alpha_{S_{III} \rightarrow S_{II}} = \frac{m_{S_{II}}}{m_{S_{III}} + m_{S_{II}}} \tag{3.33}$$

$$\alpha_{S_{II} \rightarrow S_{I}} = \frac{m_{S_{I}}}{m_{S_{II}} + m_{S_{I}}} \tag{3.34}$$

The net rate of reaction of each desorption step is defined in terms of the transformed fraction, Eq. 3.15. As done for the absorption analysis, the function $g(\alpha)$ is empirically determined by comparing the transformed fraction during the experiments with the value predicted by the integrated equation of different kinetic models, see Table 3.2. Further analysis of the empirical rate constant in Eq. 3.15 and its fitting procedure is done as for the hydrogen absorption model (see subsection 3.2.1).

3.3.2 Experimental approach

The method of material preparation and the utilized apparatus for the kinetic measurements are as described in Chapter 2. The apparatus and the geometry of the cell were selected to assure in good approximation isothermal and isobaric conditions during the experiments (Section 3.2.3). The reaction kinetics of each desorption step was individually investigated by choosing specific p-T pairs for the initial and final states. The thermodynamically stable states of the reacting system according to p-T conditions are presented in Fig. 3.22. Table 3.5 summarizes initial and final conditions used to study each desorption reaction.

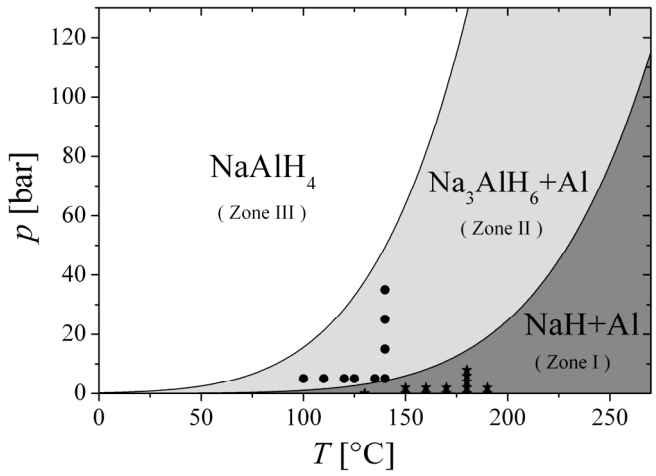

Figure 3.22: Stable states of the sodium alanate reacting system under hydrogen pressure at different p-T conditions. At p-T conditions inside zone I, II and III, the most stable solid states are NaH+Al, Na_3AlH_6+Al, and $NaAlH_4$, respectively. The circles (•) and the stars (★) correspond to p-T conditions for the final state of experiments for the first and second desorption steps, respectively.

Table 3.5: Location of the initial and final states for the desorption experiments according to the zones on Fig. 3.22.

Desorption step	Reaction	Initial State	Final State
First	$3NaAlH_4 \rightarrow Na_3AlH_6 + 2Al + 3H_2$	Zone III	Zone II
Second	$Na_3AlH_6 + 2Al + 3H_2 \rightarrow 3NaH + 3Al + 4.5H_2$	Zone II	Zone I

3.3.3 Hydrogen desorption of $NaAlH_4$ forming Na_3AlH_6+Al: $S_{III} \rightarrow S_{II}$

Desorption experiments were carried out at different p-T conditions with starting state within zone III and final state within zone II (see Fig. 3.22). Previous absorptions with final conditions within zone III guaranteed the starting state of the material within this zone for the subsequent desorption. The experimental desorptions yielded hydrogen capacities of about 2.3 wt%, agreeing with the obtained results for the second absorption step.

Figure 3.23 shows hydrogen desorption measurements performed at 5 bar and temperatures between 100 °C and 140 °C. All desorptions start immediately and remain at constant rate without showing an

incubation period or an inflection. Such a linear behaviour hints at surface reaction limited kinetics. It changes only when the transformed fraction is close to 1 and the maximal experimental capacity is almost reached. As expected because of the endothermic nature of the desorption process, the rate of desorption always increases with the temperature. At 140 °C and 5 bar full desorption is done in less than 5 minutes.

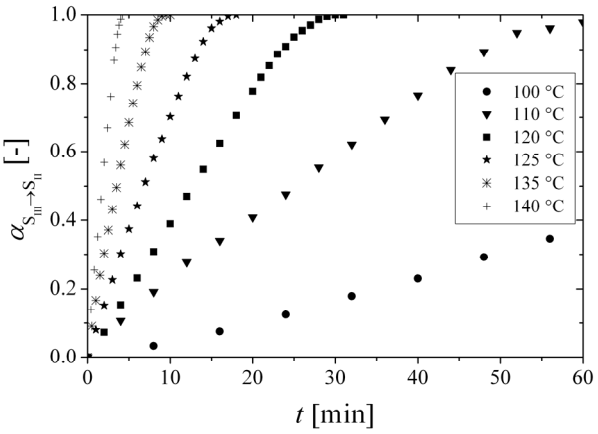

Figure 3.23: Desorption measurements of $NaAlH_4$ forming Na_3AlH_6+Al at 5 bar and temperatures between 100 °C and 140 °C. The transformed fraction is normalized to the total mass of hydrogen desorbed in each experiment after completion.

The desorptions at 140 °C under hydrogen back-pressures between 5 bar and 35 bar also start immediately and their slopes have the same qualitative behaviour, as shown in Figure 3.24. The hydrogen back-pressure shows a clear effect on the rate of desorption. For example, by reducing the hydrogen back-pressure from 25 to 5 bar, the rate of desorption approximately doubles.

3.3.4 Hydrogen desorption of Na_3AlH_6 forming NaH+Al: $S_{II} \rightarrow S_I$

The desorptions of Na_3AlH_6, $S_{II} \rightarrow S_I$, had a starting state inside zone II and final state inside zone I. Previous absorptions under conditions inside zone II ensured the starting state in this zone for these desorptions. The experimental capacities measured for this desorption step were around 1.6 wt%, in agreement with the measured capacities during the absorption experiments for this step. Figure 3.25 shows the results of the hydrogen desorption measurements at different temperatures under a hydrogen back-pressure of 0 bar (ca. 50 mbar). The rate of desorption increases with the temperature, at 190 °C requiring 10 min to desorb more than 97 % of the hydrogen stored. The desorptions start immediately, and in contrast to the case of $NaAlH_4$, the desorption of Na_3AlH_6 forming NaH+Al does not present a linear behaviour. The reaction rate does not stay constant as the desorption proceeds.

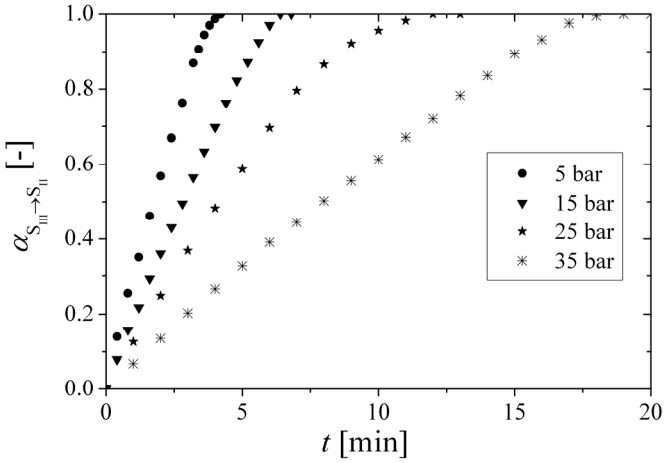

Figure 3.24: Desorption measurements of $NaAlH_4$ forming Na_3AlH_6+Al at 140 °C and hydrogen back-pressures between 5 bar and 35 bar.

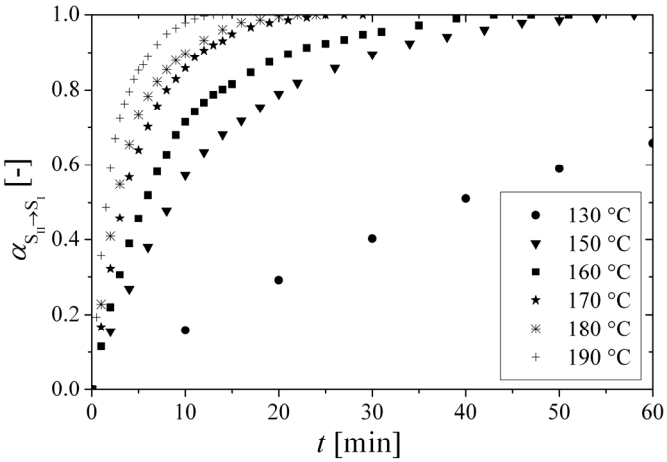

Figure 3.25: Desorption measurements of Na_3AlH_6 at 0 bar and temperatures between 100 °C and 140 °C.

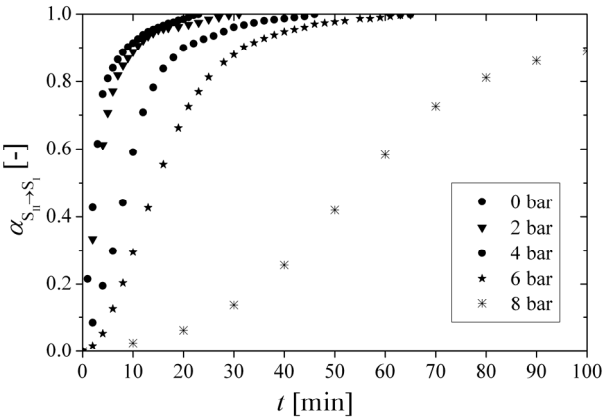

Figure 3.26: Desorption measurements of Na_3AlH_6 at 180 °C and different hydrogen back-pressures.

3.3.5 Discussion

3.3.5.1 Hydrogen desorption of $NaAlH_4$ forming Na_3AlH_6+2Al: $S_{III} \rightarrow S_{II}$

As mentioned before, the rate of desorption of $NaAlH_4$, when transforming to Na_3AlH_6+Al and releasing H_2, has a linear behaviour corresponding to a zero-order reaction, which is characteristic of surface controlled kinetics [46]. The best fitting model for Eq. 3.15 is obtained with the function $g(\alpha) = 1$. Thus, Eq. 3.15 for this desorption reaction corresponds to:

$$\frac{d\alpha_{S_{III}\rightarrow S_{II}}}{dt} = k_{S_{III}\rightarrow S_{II}} \tag{3.35}$$

This result agrees with the results of Sandrock et al [51], who also reports a constant reaction rate, independent of the transformed fraction. However, it is in contrast with the first order kinetic equation reported by Luo and Gross using $TiCl_3$ [42] and Kiyobayashi et al. using $Ti(OBu^n)_4$ and $Zr(OBu^n)_4$ [53] for the desorption of $NaAlH_4$ forming Na_3AlH_6.

The fitting procedure of the constant $k_{S_{III}\rightarrow S_{II}}$, based on Eq. 3.16, yields as best fitting function:

$$f_{S_{III}\rightarrow S_{II}}(p, p_{eq}) = \left(\left(p_{eq} - p\right)/p_{eq}\right)^2 + 1.04\left(\left(p_{eq} - p\right)/p_{eq}\right) \tag{3.36}$$

with Arrhenius parameters A=5.41×10^{10} s^{-1} and E_a=105.85 kJ mol^{-1}. This function was found to be most appropriate for the fitting procedure described in Section 3.2.1. The first and second order terms of the function originate from the Taylor series of the function $\ln\left(p_{eq}/p\right)$, which defines the driving force of the sorption process. Figure 3.27 shows the results of the fitting of the experimental data by

use of these function and parameters. An increment of temperature will affect the rate of reaction not only by the Arrhenius factor but also by the function $f_{S_{III}\rightarrow S_{II}}(p, p_{eq})$ through the equilibrium pressure $p_{eq}(T)$. By increasing the temperature, the value p_{eq} increases and thus the difference $p_{eq} - p$. This makes the driving force represented by $f_{S_{III}\rightarrow S_{II}}(p, p_{eq})$ larger and consequently the rate of reaction increases. Figure 3.28 shows calculated desorption curves using the fitting equations at the conditions of the experimental curves shown in Figs. 3.23 and 3.24.

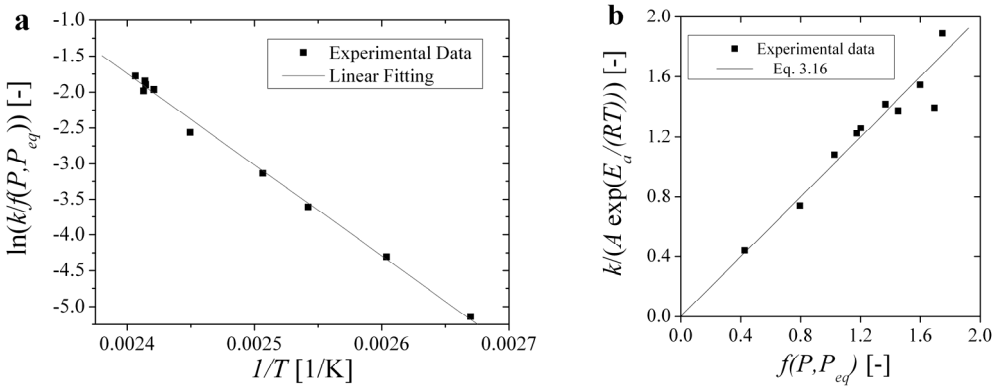

Figure 3.27: Kinetic fitting of the desorption of $NaAlH_4$ forming Na_3AlH_6+Al. Equation 3.16 defines the fitting relation. The parameters A and E_a in the right diagram (b) are determined in the fitting presented in the left diagram (a) (A =5.41×10^{10} s^{-1} and E_a =105.85 kJ mol^{-1}).

The rate constant $k_{S_{III}\rightarrow S_{II}}$ is calculated for several conditions p-T by using the functions and parameters determined through the fitting and then plotted in Fig. 3.29. When the hydrogen back-pressure is higher than the equilibrium pressure of the first desorption step, the rate constant is 0 by definition. By increasing the temperature as well as by decreasing the hydrogen back-pressure the value of the rate constant increases, the effect of the temperature being higher than the effect of the hydrogen back-pressure in the given ranges. The constant rate lines of the contour also demonstrate that by changing conditions it is possible to have the same reaction rate at different temperatures by modifying the hydrogen back-pressure e.g. the desorption at 140 °C and 20 bar and at 130 °C and 0 bar.

The minimum value of $k_{S_{III}\rightarrow S_{II}}$ was calculated using Eq. 3.35 and plotted also in Fig. 3.29 (dashed line), such that the material during the first desorption step fulfils the discharging rate (max) of

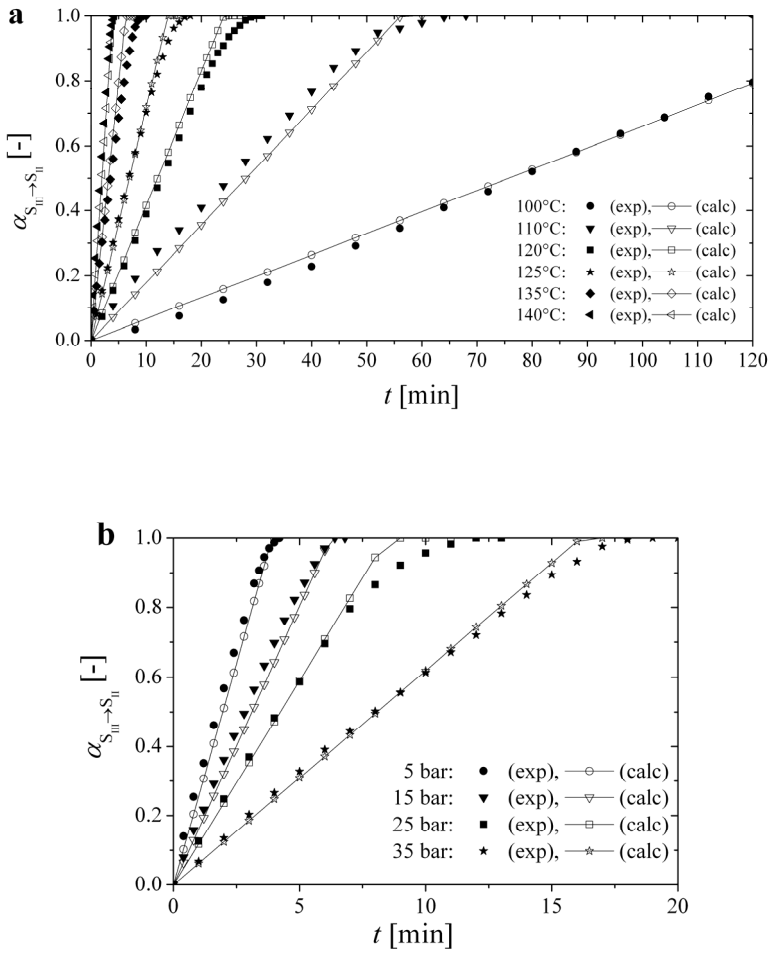

Figure 3.28: Calculated desorptions of $NaAlH_4$ forming Na_3AlH_6+Al at (a) 5 bar and different temperatures, and at (b) 140 °C and different hydrogen back-pressures. The experimental conditions of the desorption measurements correspond to the data in (a) Fig. 3.23 and (b) Fig. 3.24.

hydrogen in a fuel cell vehicle. The calculation assumed the conditions defined in [7]: hydrogen discharging rate of 2 g s^{-1} and a total storage mass of 6 kg of hydrogen. This minimum value of $k_{S_{III}\rightarrow S_{II}}$ corresponds to 0.034 min^{-1}. Under this condition, temperatures starting from 120 °C can maintain 6 bar of hydrogen back-pressure. Temperatures lower than 114 °C are not sufficient at any level of hydrogen back-pressure to fulfil this required discharging rate. This analysis is necessary in the evaluation and design of hydrogen storage systems based on metal hydrides; for example, for the determination of p-T working conditions required for the integration of the waste heat from a fuel cell with the heating system for the desorption of hydrogen from the hydride in a fuel cell powered system.

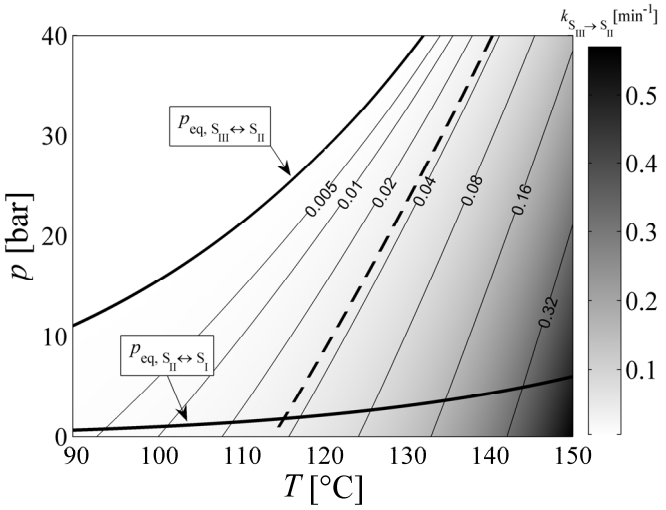

Figure 3.29: Calculated values of the rate constant $k_{S_{III}\rightarrow S_{II}}$ as a function of temperature and hydrogen back-pressure. The contour lines represent points with the same value of rate constant. The dashed line (---) is the minimum value of $k_{S_{III}\rightarrow S_{II}}$ that fulfils the discharging rate conditions defined in [7].

3.3.5.2 Hydrogen desorption of Na_3AlH_6 forming NaH+Al: $S_{II} \rightarrow S_I$

The fitting procedure for this desorption step gave the JMA equation with n=1 as best representing model, Eq. 3.37, which is equivalent to the expression for a rate of reaction of first order.

$$\frac{d\alpha_{S_{II}\rightarrow S_I}}{dt} = k_{S_{II}\rightarrow S_I}\left(1-\alpha_{S_{II}\rightarrow S_I}\right) \tag{3.37}$$

An equivalent first order kinetic equation is also reported by Luo and Gross [42] and and Kiyobayashi et al. [53]. However, it is in contrast to the constant reaction rate reported by Sandrock et al. [51].

The effect of the hydrogen back-pressure on desorption of Na_3AlH_6 is depicted in Fig. 3.26. During desorption the reaction rate does not always follow a first order behaviour as the hydrogen back-pressure gets close to the corresponding equilibrium pressure. It is found that only desorption measurements performed at low hydrogen back-pressures have rates according to first order reactions. At hydrogen back-pressures which draw near to the equilibrium pressure, the best fitting n parameter of the JMA equation for each measurement increases from 1 to 2, indicating a possible change in the reaction mechanism or in the rate limiting step (e.g. potential nucleation problems). Figure 3.30 illustrates this effect by comparing the relation between the expression $\left(p_{eq}-p\right)/p_{eq}$ and the best fitted n parameter of the JMA equation for different experiments. Under conditions far away from equilibrium $\left(p_{eq} >> p\right)$, n is close to 1. While approaching equilibrium conditions, the parameter n

increases. This indicates that the model with the JMA equation n=1 is only valid if $(p_{eq} - p)/p_{eq}$ >0.7.

The kinetic constant $k_{S_{II} \rightarrow S_I}$ was fitted by using $g(\alpha) = (1 - \alpha)$ for all the measurements. The fitting data is best adjusted by using the function:

$$f_{S_{II} \rightarrow S_I}(p, p_{eq}) = \left((p_{eq} - p)/p_{eq}\right)^2 - 0.46\left((p_{eq} - p)/p_{eq}\right) \quad (3.38)$$

The fitted Arrhenius parameters for Eq. 3.16 are A=3.41×10^8 s^{-1} and E_a=91.5 kJ mol^{-1}. Figure 3.31 shows the comparison of the experimental data and the calculated desorption based on the model and fitted parameters. It validates the fitting for low hydrogen back-pressure with good agreement. For desorptions at hydrogen back-pressures close to the equilibrium, the fitting deviates from the experimental data, as discussed above, (see e.g. desorption at 180 °C and 8 bar on Fig. 3.31).

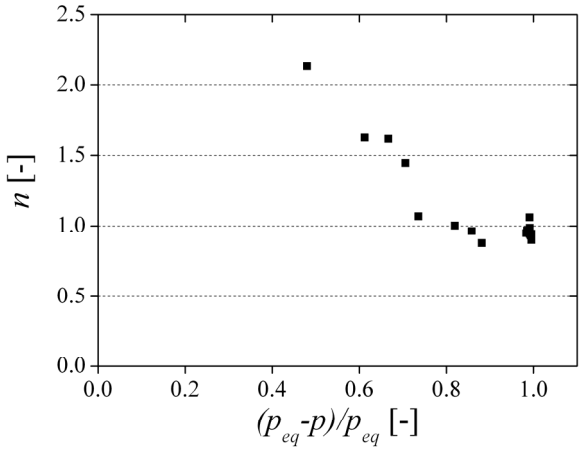

Figure 3.30: Best fitted JMA parameter n plotted against $(p_{eq} - p)/p_{eq}$ for the experimental desorption of Na_3AlH_6 at different p-T conditions.

The calculated values of the rate constant $k_{S_{II} \rightarrow S_I}$ are shown on Fig. 3.32 (as similarly done for the first desorption step). At p-T conditions when the hydrogen back-pressure is higher than the equilibrium pressure of the second desorption step, the rate constant takes a value of 0 by definition. The qualitative behaviour of the rate constant of the first desorption step also applies for the rate constant of the second one in regard to temperature and pressure. By both increasing the temperature and decreasing the hydrogen back-pressure the value of the rate constant increases. Again the effect of varying the temperature is higher than the corresponding effect of the hydrogen back-pressure. Quantitatively, if compared under the same p-T conditions and using Eq. 3.35 and the fitted

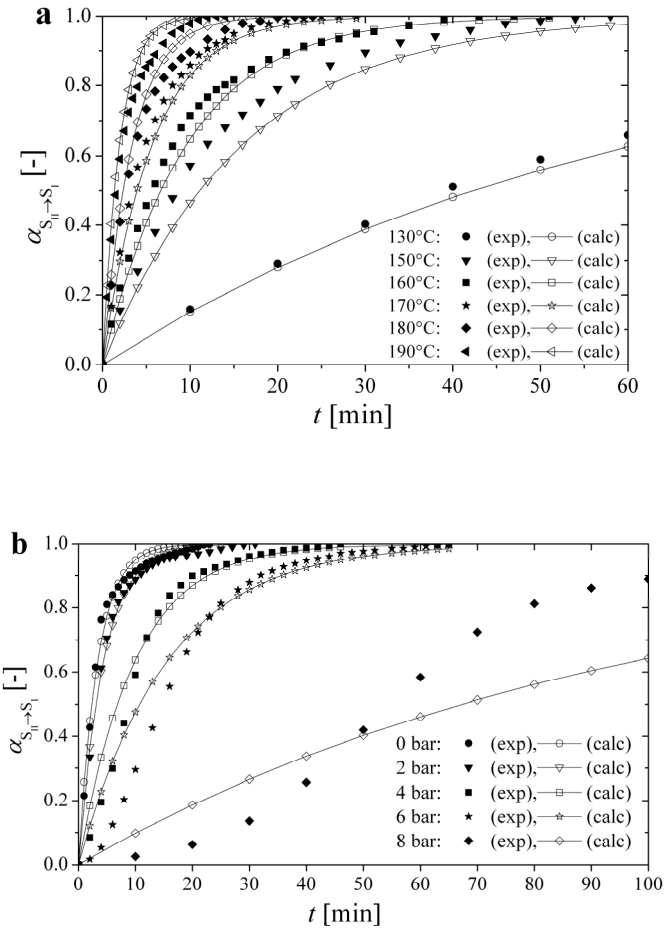

Figure 3.31: Calculated desorptions of Na_3AlH_6 at (a) 0 bar and different temperatures, and at (b) 180 °C and different hydrogen back-pressures. The experimental conditions of the desorption measurements correspond to the data in (a) Fig. 3.25 and (b) Fig. 3.26.

parameters, the first desorption step is substantially faster than the second one. For example, at 140°C and 0 bar (ca. 50 mbar), the calculated initial hydrogen desorption rate of the first step is 10 times higher than the rate of the second desorption step. The second desorption step needs higher temperatures in order to obtain the required discharging rate of hydrogen in a fuel cell vehicle [7]. At the beginning of the desorption step ($\alpha_{S_{II}\rightarrow S_I}$ =0), the temperature must be at least 147 °C to obtain the discharging rate of 2 g s^{-1} when the hydrogen back-pressure is 0 bar. In case of the partially desorbed sample, e.g. $\alpha_{S_{II}\rightarrow S_I}$ = 0.5 and = 0.9, temperatures of 159 °C and 189 °C, respectively, are required to achieve this fast rate of desorption.

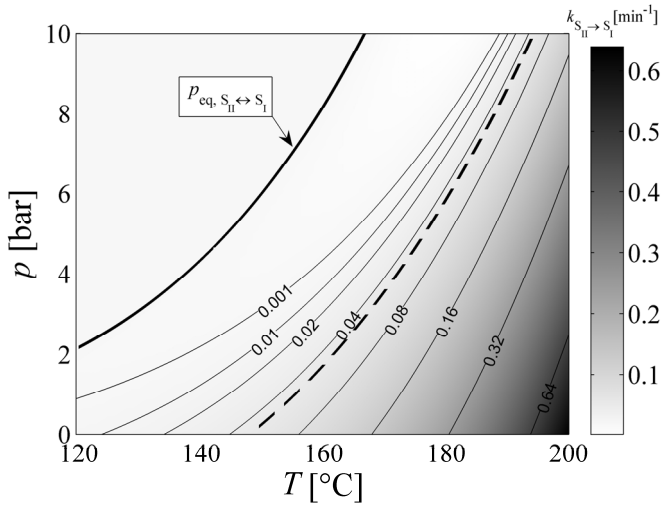

Figure 3.32: Calculated values of the rate constant $k_{S_{II}\rightarrow S_I}$ as a function of temperature and hydrogen back-pressure. The contour lines represent p-T conditions with the same value of rate constant. The dashed line (---) is the minimum value of $k_{S_{II}\rightarrow S_I}$ that fulfils the discharging rate conditions defined in [7] (for totally absorbed material when $\alpha_{S_{II}\rightarrow S_I}$=0).

3.3.5.3 Kinetic model and validation

The desorption steps $S_{III} \rightarrow S_{II}$ and $S_{II} \rightarrow S_I$ proceed as consecutive reactions, or simultaneously. This is the case when changing conditions from zone III to I of Fig. 3.22. As soon as $NaAlH_4$ desorbs to Na_3AlH_6 and Al, Na_3AlH_6 desorbs further to NaH and Al because it is unstable in zone I. Desorption steps and material balances are defined in the following equations:

$$S_{III} \xrightarrow{r_{d1}} S_{II} \xrightarrow{r_{d2}} S_I \tag{3.39}$$

$$\frac{dm_{S_I}}{dt} = r_{d2} \tag{3.40}$$

$$\frac{dm_{S_{II}}}{dt} = r_{d1} - r_{d2} \tag{3.41}$$

$$\frac{dm_{S_{III}}}{dt} = -r_{d1} \tag{3.42}$$

$$r_{d1} = k_{S_{III}\rightarrow S_{II}}\left(m_{S_{III}} + m_{S_{II}}\right) \tag{3.43}$$

$$r_{d2} = k_{S_{II}\rightarrow S_I} m_{S_{II}} \tag{3.44}$$

Calculated desorption curves based on the kinetic model are presented in Fig. 3.33. The respective experimental results are shown for comparison. It must be pointed out that the high sensitivity of the rate of reaction with respect to the experimental temperature may cause deviations from the experimentally measured, e.g. the first desorption step at 0 bar and 100 °C in Fig. 3.33 (at these conditions, a difference of ±1 °C in the temperature for the calculation produces a change of ±10 % in the rate of reaction). The calculated desorption at 0 bar and 102 °C is also shown in the figure to illustrate the sensitivity of the calculated rate of reaction. In general, the agreement between calculated and experimental results in terms of both the expected capacity and the kinetic behaviour is found to be very good.

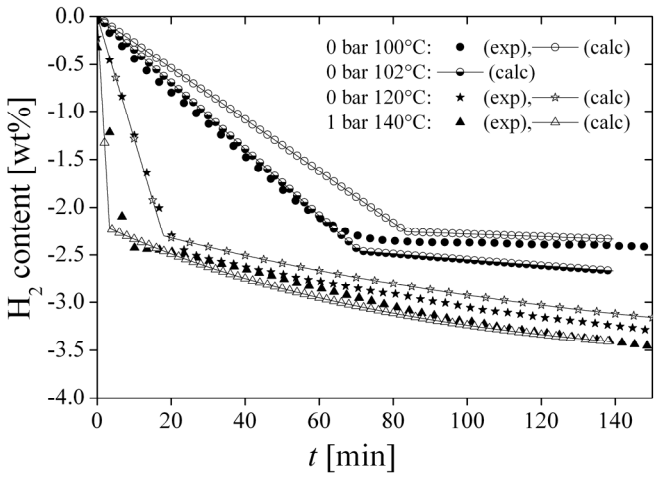

Figure 3.33: Experimental and calculated desorption curves of $NaAlH_4$ at different conditions.

3.4 Scaled-up sorptions

The hydrogen storage of a fuel-cell based car would require 6 kg of hydrogen in order to have a driving range of 500 km [7]. This value corresponds to a storage system containing more than 100 kg of sodium alanate material. The hydrogen storage system should fulfil additional defined criteria for the fuel-cell car, such as refuelling times and delivery rates [7]. It was shown in Section 3.1 that the sorption behaviour of sodium alanate material strongly depends on the size of the hydride bed. This result evidences the necessity of study the sorption scaled-up behaviour of the material looking towards implementation of the material in practical systems. This section shows and discusses the results of the experimental hydrogenation of larger amounts of material. The experiments were performed at the tank charging station presented in Section 2.3. First, the evaluation of the tank station using a conventional metal hydride as reference is presented. Afterwards, measurements of sodium

alanate material are performed. The section concludes with the evaluation on the sorption behaviour of mixtures of sodium alanate material with expanded graphite (EG).

3.4.1 Hydrogenation of Hydralloy C5

The constructed tank station was first tested by measuring the hydrogen sorption of 1.3 kg of Hydralloy C5 (GfE Metalle und Materialien GmbH) filled in a 500 ml stainless-steel tank (see Fig. 2.4). The chemical composition of the used Hydralloy C5 is $Ti_{0.95}Zr_{0.05}Mn_{1.5}V_{0.45}Fe_{0.1}$, with molar mass of 158.39 g mol^{-1}, density of 6.4 g ml^{-1} and apparent density of 3.5 g ml^{-1} [55]. Although it has a hydrogen absorption capacity of 1.8 wt% according to the manufacturer, experimental sorption measurements performed in the Sieverts' apparatus led to 1.25 wt% at 50 bar and 25 °C, see Fig. 3.34. The loss of capacity of the alloy may have been caused by oxidation of the material during handling [56]. A thermal activation of the material is necessary to dissolve a possible oxide surface layer [56]. This material without activation was simply used as standard reference material for the evaluation of the hydrogen tank station with the Sieverts' apparatus.

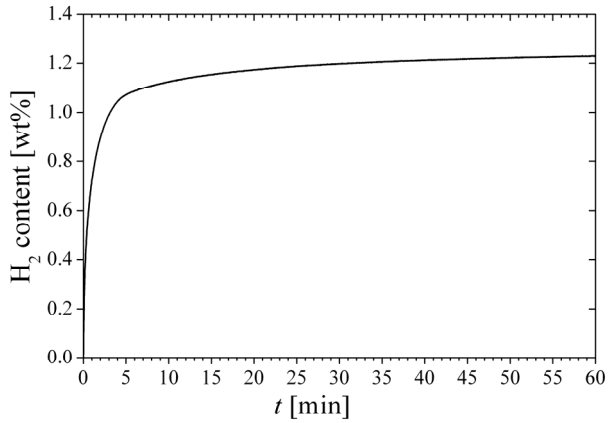

Figure 3.34: Absorption measurements of Hydralloy C5 at the Sieverts' apparatus. Hydrogen inlet-pressure was 50 bar, initial temperature was 25 °C.

Figure 3.35 shows the results of hydrogen absorption measurements of the Hydralloy C5 at 50 bar and 20 °C. Prior to these experiments, the material was activated by cycling it two times. The final hydrogen content measured in the tank station was between 1.3 and 1.4 wt%. Two sets of experiments are presented in Fig. 3.35: absorption performed with and without heat exchanger. At the beginning of the absorption measurement without heat exchanger, the temperature in the hydride bed increased from 20 °C up to 75 °C, and then it was cooled down very slowly by natural convection to the surroundings. After one hour the temperature is still high (approx. 60 °C). In contrast, the absorption

performed with heat exchanger at 20 °C was clearly faster. The increase of temperature of the hydride bed was 15 °C lower. After only 10 minutes the temperature decreased to 30 °C and after 20 minutes already down to around 20 °C. In comparison, while it took 3 hours without heat exchanger to reach 90 % of the capacity (not shown in Fig. 3.35), the same capacity is reached within 12 min if the absorption is carried out with heat exchanger. The experiments are presented with their duplicates in order to show the reproducibility of these results.

Desorption was carried out in a set of experiments with and without heat exchanger also, shown in Fig. 3.36. In case of the desorption without heat exchanger the temperature of the hydride bed dropped from the initial 20 °C down to -10 °C in less than a minute. Natural convection to the surroundings increased the temperature to -6 °C after almost three hours. Only after 6 hours (not shown in the Fig. 3.36), 90 % of the final capacity is desorbed. In the case of desorption performed with heat exchanger, 90 % of the final capacity is reached in less than 40 minutes. The deepest measured temperature was -6 °C, and after 10 and 20 minutes the temperature in the hydride bed was 10 °C and 20 °C, respectively.

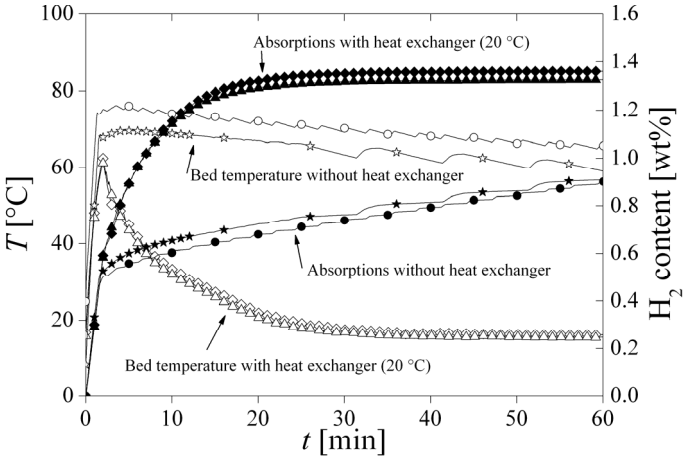

Figure 3.35: Absorption measurements of Hydralloy C5 at the tank station. Hydrogen inlet-pressure was 50 bar, initial temperature 20 °C. Circles (●) and stars (★) correspond to experiments performed without heat exchanger. Triangles (▲) and diamonds (♦) correspond to experiments performed with heat exchanger at 20 °C. Dark-filled symbols correspond to hydrogen contents [wt%], empty symbols are bed temperatures [°C].

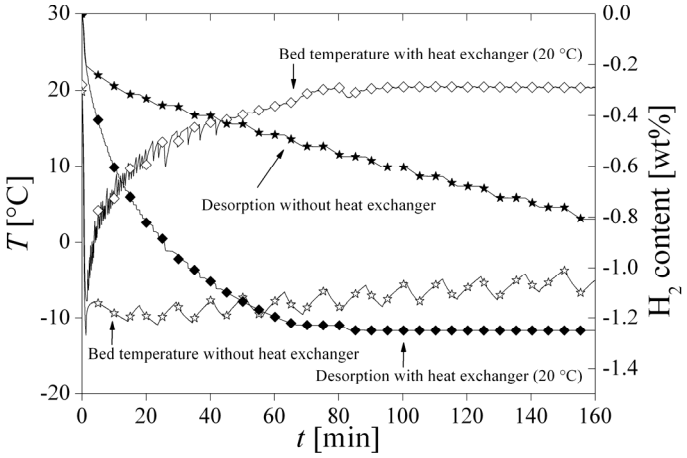

Figure 3.36: Desorption measurements of Hydralloy C5 at the tank station. Initial temperature was 20 °C, initial pressure in the tank 50 bar. Diamonds (♦) correspond to experiments with heat exchanger at 20 °C and stars (★) to experiments performed without heat exchanger. Dark-filled symbols are hydrogen contents [wt%], empty symbols are bed temperatures [°C].

3.4.2 Hydrogenation of sodium alanate material

For the measurements of the sodium alanate material, a tank with thicker walls and consequently less volume was used because of the higher temperature and pressure conditions in comparison to the sorption conditions of the Hydralloy C5. A 300 ml stainless-steel tank (see Fig. 2.4) was filled with 186 g of sodium alanate material prepared as explained in Section 2.1. The material included the additional 5 wt% of carbon during milling. The intern volume of the empty tank was determined with water at room temperature (ρ =1.00 g ml^{-1}). Intern empty volume was 300 ml. Thus, the experimental apparent density of the hydride bed inside the tank was 0.62 g ml^{-1}. Before starting the absorption measurements, the filled tank is set under vacuum and heated up to the temperature of the experiment. Figure 3.37 shows the hydrogen content and the temperature inside the tank during the first and second absorption measurements. The maximum hydrogen inlet flow through the flow meters was set to 10 ln min^{-1} during the first and the second absorption measurements. After the second absorption measurement the maximum inlet hydrogen flow was set to 20 ln min^{-1}. The maximum hydrogen flow is set specifically for the period of time when the pressure increases from its initial value up to the nominal pressure of the experiment. Afterwards, the nominal pressure is regulated ±1 bar using an algorithm from the software application of the tank station. After the first absorption measurement ran for several hours without further detectable increase of the hydrogen content, the material was desorbed at 120 °C and vacuum for several days. In order to guarantee full absorption of the material,

further hydrogenations were left to run for several hours as well. After each absorption measurement, the material was desorbed under vacuum also for several hours. Fig. 3.38 summarizes the five performed absorptions with sodium alanate material in the 300-ml tank.

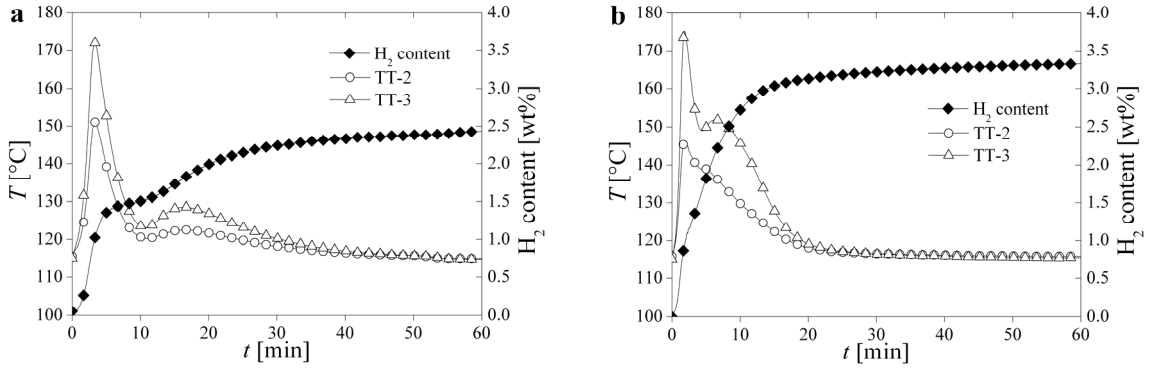

Figure 3.37: (a) First and (b) second absorption measurements of sodium alanate material at the tank station. Initial temperature was 115 °C. Hydrogen inlet-pressure is 100 bar. TT-3 and TT-2 are the temperatures in the centre of the hydride bed and in a non-defined position in the bed of material, respectively (see Fig. 2.4)

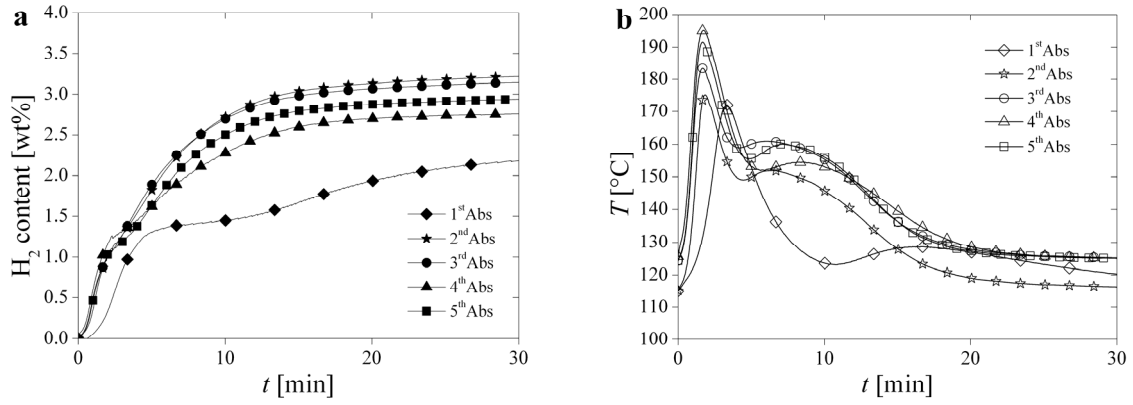

Figure 3.38: (a) Hydrogen content and (b) temperature profiles of the 1st to 5th absorption measurements of sodium alanate material performed at the tank station. Initial temperatures were between 115 °C and 125 °C. Hydrogen inlet-pressure is 100 bar. TT-3 is the temperature in the centre of the hydride bed (see Fig. 2.4).

3.4.3 Addition of expanded graphite

It was shown in Section 3.1 how the addition of expanded graphite (EG) enhances the effective thermal conductivity of sodium alanate material. Using this beneficial effect in the hydrogenations of systems with larger bed sizes, sodium alanate material was mixed with 10 wt% of EG (flakes, particle size 500 μm, SGL Technologies GmbH, Meitingen, Germany) and then filled in a 300 ml stainless-steel tank. A total mass of 160 g of mixture was weighed into the tank, corresponding to an apparent density of the hydride bed inside the tank of 0.53 g ml^{-1}. Figure 3.39 summarizes the results of the performed absorptions (13 in total). All the measured absorptions shown in the figure were performed with heat exchanger set to 125 °C and a maximum inlet hydrogen flow of 20 ln min^{-1}. The absorption measurements were let to run for 3 hours, after which the pressure was released and the system evacuated under vacuum at 160 °C for 16 hours. Desorption at these conditions guaranteed full desorption for the following absorption measurement. Fig. 3.40 shows the results of a desorption measurement. For further comparison, first to fifth absorption measurements of the sodium alanate material with EG and the material without EG are presented in Fig. 3.41.

3.4.4 Discussion

As it is shown in Fig. 3.35 and 3.36, the tank station was successfully tested during the hydrogenation of Hydralloy C5. The self-developed LabView application for on-line measuring and control of the experiments was as well satisfactorily proved. In respect to the quantitative results, there is very good

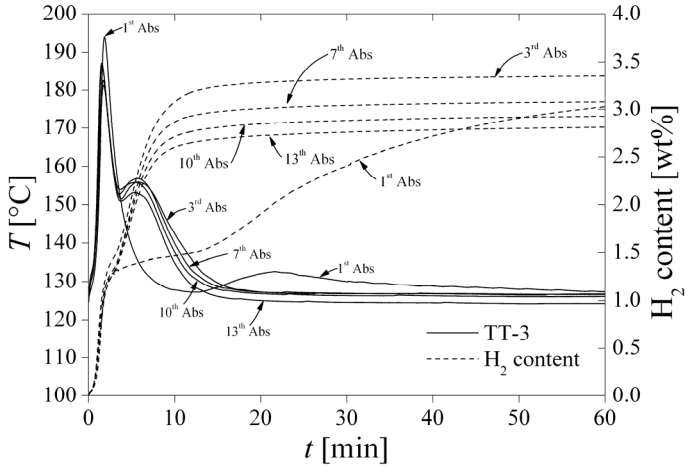

Figure 3.39: Absorption measurements of sodium alanate material mixed with 10 wt% EG performed at the tank station. Initial temperature was around 115 °C and 125 °C. Hydrogen inlet-pressure was 100 bar. TT-3 is the temperature in the centre of the hydride bed (see Fig. 2.4).

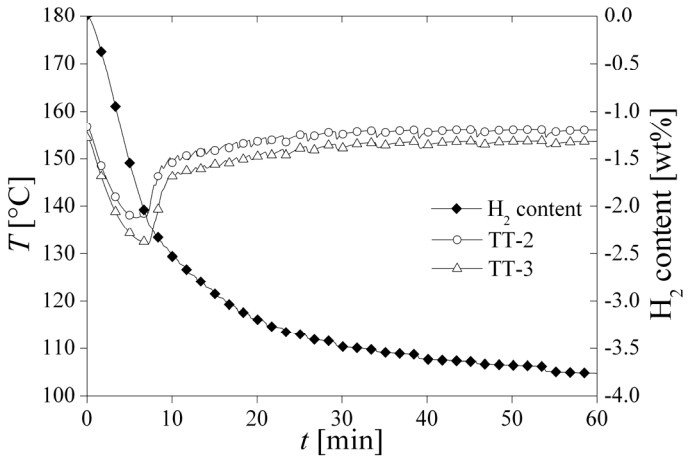

Figure 3.40: Desorption measurement of sodium alanate material mixed with 10 wt% EG performed at the tank station. Initial temperature was 155 °C and initial pressure was 87 bar. TT-3 and TT-2 are the temperatures in the centre of the hydride bed and in a non-defined position in the bed of material (see Fig. 2.4).

agreement of the hydrogen content of the material measured at the tank station (1.3 wt%, see Fig. 3.35) in comparison to the obtained at the Sieverts' apparatus (1.25 wt%, see Fig. 3.34). The duplicate of the experiments shown in Fig. 3.35 demonstrates very good measurement reproducibility. In the case of desorption, measurements shown in Fig. 3.36 had a total hydrogen capacity around 1.25 wt%, in good agreement with the achieved capacities in the absorption measurements of Fig. 3.35.

Both Figs. 3.35 and 3.36 show the clear effect of heat transfer on the sorption behaviour of the Hydralloy C5. The set of absorption experiments without heat exchanger require longer times in order to achieve the same hydrogen content compared to the measurements with heat exchanger. This is due to the higher temperature during the absorption measurements without heat exchanger, which reduces the thermodynamic driving force. The rate of absorption is in this case limited by heat exchange by natural convection to the surroundings, which is quite low. The effect of the heat exchanger is also clear in desorption measurements. Desorption with heat exchanger is substantially faster due to the higher temperature in the hydride bed maintained during the experiments.

The saw-tooth shaped lines, like the bed temperatures in Figs. 3.35 and 3.36, are due to the algorithm employed to control the pressure inside the tank during the measurements. In order to improve the accuracy of the flow meter measurements at low flow rates, it was operated in cycles by opening and closing the inlet or outlet flows. Cycling was controlled by pressure measurements. The saw-tooth shape is a consequence of the alternate temperature decrease (e.g. during desorption due to the hydrogen outflow) and the temperature increase (e.g. during desorption due to the pressure increase

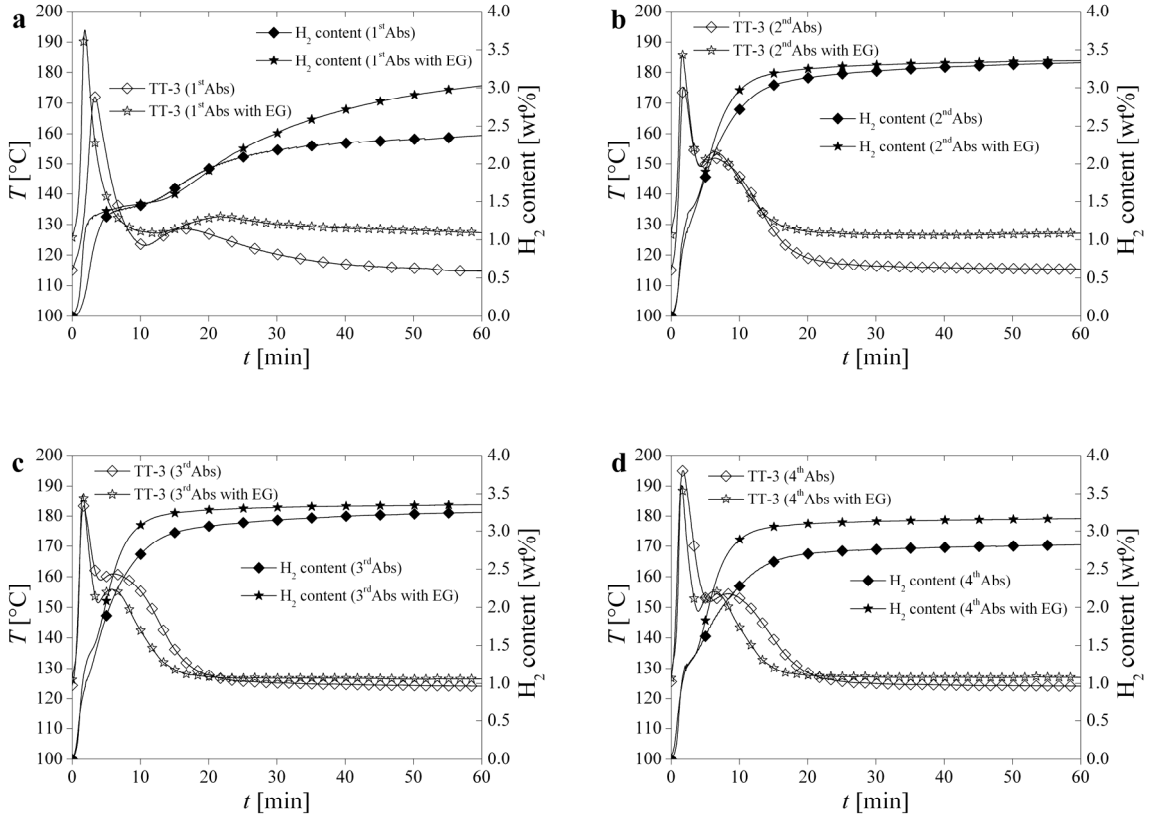

Figure 3.41: Comparison of the (a) 1st, (b) 2nd, (c) 3rd and (d) 4th absorption measurements of sodium alanate material with and without addition of expanded graphite. The material was filled in a 300 ml tank performed at the tank station. Initial temperature was around 115 °C and 125 °C. Initial pressure was 0 bar. Hydrogen inlet-pressure was 100 bar. TT-3 is the temperature in the centre of the hydride bed (see Fig. 2.4). The maximum hydrogen inlet-flow was 20 ln min^{-1}.

inside the tank when no outflow is allowed). A similar algorithm was used to regulate the pressure during both absorption and desorption experiments. In spite of this, smooth hydrogen content curves were obtained thanks to the mass balance equation, which considers not only hydrogen inlet and outlet flows but the change hydrogen in the gaseous phase contained in the void volume of the tank (see Eq. 2.2)

In the first absorption measurement of sodium alanate material (Fig. 3.37a), the two steps of the absorption are directly distinguished both from the hydrogen content and the temperature profiles. The temperature increase is caused by the fast exothermic hydrogenation of the material coupled with the hydrogen heating upon expansion from the pressure of the inlet line (>100 bar) to the final pressure inside the tank. The temperature in the centre of the hydride bed increases from the initial 115 °C to a maximum of 175 °C during the first five minutes. This corresponds to the first absorption step. Approximately 1.4 wt% of hydrogen is absorbed at this step (after 5 min). The temperature behaviour

with respect to time agrees very well with the slope of the hydrogen content curve: on one hand, when the slope of the hydrogen absorption is high enough, the temperature increases. On the other hand, when the slope of the hydrogen absorption is low, the material cools down towards the temperature of the external cooling fluid.

The second absorption measurement (Fig. 3.37b) is faster compared to the first one, mainly due to the activation of the material during the first cycle. Especially the second absorption step is significantly faster in the second absorption measurement: after the first temperature peak being 175 °C, the temperature does not fall drastically as it happens in the first absorption measurement after the first step. In the second absorption measurement, the temperature falls down to around 150 °C only and the second absorption step proceeds. In fact, in the second absorption measurement 90 % of the hydrogen capacity is reached within 14 minutes, while for the first absorption measurement less than 50 % of the capacity is reached in the same time period. In further absorption measurements, summarized in Fig. 3.38, the hydrogen content and temperature profiles are qualitatively very similar. Though, the highest measured temperature in absorptions 3rd to 5th is higher (190 °C), when compared to the first two absorptions (170 °C). This effect is related to the initial temperature of the system as the experiments started. While the initial temperature of the first and second absorptions was 115 °C, further absorptions started at 125 °C. In respect to the reached hydrogen content in the different absorptions, a maximum of 3.4 wt% 2nd and 3rd absorptions is observed. In further absorptions, however, a slight decrement of the capacity is seen. One cause may be the physical separation of the constituents of the composites in the hydride bed after the time, which is as well an explanation of the lower practical hydrogen capacity in comparison to the theoretical capacity of the material, as discussed previously in Section 3.2. Another possible explanation is the melting and/or sintering of reacting material in the hydride bed. This may happen since the melting point of $NaAlH_4$ is 183 °C [57] only and temperatures over this value were measured during the absorptions (Figs. 3.37 and 3.38). $NaAlH_4$ could already have been formed at those temperatures higher than its melting point. Additionally, conditions for sintering are also present later since the temperature remains close to the melting point of $NaAlH_4$. Melting and/or sintering negatively affect the surface area of the particle as well as the catalyst activity, which brings a decrease in the fraction of material that finally reacts. Thus, the measured hydrogen capacity of the material decreases as well.

Hydrogen absorption measurements of sodium alanate material with additional 10 wt% EG, as shown in Figs. 3.39 and 3.41, present a similar behaviour as the material without EG: hydrogen capacities between 3 and 3.5 wt% are obtained, two-step behaviour of the hydrogenation is observed in the hydrogen content and temperature curves, and after the first absorption the material is activated, exhibiting faster kinetics. During the first absorption measurements (Fig. 3.41a), the higher peak of temperature of the material with EG in the first absorption step is explained by the higher initial

temperature and higher hydrogen flow allowed. However, inspection of absorption kinetics in Fig. 3.41 reveals faster absorption kinetics of the material with EG. Because of the EG content, the hydride bed has higher effective thermal conductivity and thus the heat released during hydrogenation can be faster removed. The temperature of the hydride bed decreases in shorter time into conditions of fast kinetics. This is favourable especially for the kinetics of the second absorption step, where the optimal temperature for absorption at 100 bar is 147 °C (see Fig. 3.20). The faster heat transfer is also reflected by shorter cooling times of the hydride bed in case of the absorptions of the sodium alanate material with EG (Fig. 3.41). As for the sodium alanate material without EG, the hydrogen capacity is also reduced by cycling of the material with EG (Fig. 3.39), and may be also due to high temperature that result into melting, sintering and/or agglomeration of the material.

It could be expected, that due to a cooling effect of the incoming hydrogen during absorptions, the temperature close to the centre (TT-3) should be lowest in the tank. Interestingly, the temperature profiles in Figs. 3.37a and 3.37b indicate that the highest temperature inside the hydride bed during absorptions may actually be located in the centre (TT-3) or close to it. In all performed absorption experiments, the temperature measured in other position of the hydride bed (TT-2) was always lower. At the wall, the temperature of the material should be closer to the temperature of the cooling fluid. This observation is determining when defining the heat transfer boundary conditions for numerical simulations of the system. Analogously for desorption, Fig. 3.40, the deepest temperature is measured close to the sinter filter in the centre of the hydride bed, while the highest must be close to the wall of the tank, at which externally the heating fluid flows.

4 Modelling and simulation: hydrogen sorption in practical systems based on metal hydrides

This chapter discusses the different sub-processes that occur during the hydrogen sorption of practical systems based on metal hydrides, i.e. intrinsic reaction and transport phenomena. It starts with the description of the model equations of the sorption sub-processes in a hydride bed. Derived from these model equations, a comparative analysis is developed to quantify how strongly each sub-process affects the overall sorption kinetics in the hydride bed and thereby the sorption-rate limiting sub-process can be identified. The last section of the chapter presents the results of finite element simulations of practical systems based on sodium alanate reactive material. The simulations are conceived to predict the hydrogen sorption behaviour in practical systems based on metal hydrides, in particular on sodium alanate material. For simplicity and clearness, the case of hydrogen absorption is selected for the explanations. The description of the sub-processes and the model equations are valid for the case of hydrogen desorption as well.

4.1 Model equations of a hydride bed and analysis of sorption rate limiting sub-process

In every hydrogen storage system based on metal hydrides, no matter the size or scale, three sub-processes occur in the hydride bed during hydrogen absorption:

1. Hydrogen transport
2. Chemical reaction
3. Heat transfer

4.1.1 Hydrogen transport

Hydrogen flows from its initial storage source, at certain pressure, to the surface of the material to be hydrogenated. This flow is possible if a difference between the pressure at the initial source and the pressure at the surface of the material exists. This difference is the driving force of the hydrogen transport sub-process (influence of gravitational and any other external fields are neglected). The

pressure drop in the hydrogen pipeline of an apparatus is in most cases negligible. For instance, through a 1 m pipe with 6 mm inner diameter the calculated hydrogen pressure drop using correlations [58] would be 0.017 bar (hydrogen flow of 0.5 kg min^{-1} at 100 bar). However, the resistance to the flow of hydrogen through the hydride bed may have bigger influence on the hydrogen transport. The flow of hydrogen through the hydride bed, considered a porous media, follows Darcy's law as momentum balance equation [59, 60]:

$$\vec{u}_g = -\frac{\kappa}{\mu}\vec{\nabla}p \tag{4.1}$$

The differential mass balance of the flow of hydrogen through the hydride bed is:

$$\frac{\partial(\rho_g \varepsilon)}{\partial t} + \vec{\nabla}\cdot(\rho_g \vec{u}_g) = -r'_{abs} \tag{4.2}$$

In Eq. 4.2, the first term of the left side is the accumulation of hydrogen in the void volume and the second term is the mass flow of hydrogen. The right hand side is a source term of hydrogen mass, corresponding to the hydrogen being absorbed by the material per unit of volume and time.

4.1.2 Chemical reaction

Following hydrogen transport, hydrogen is absorbed by the material in a chemical reaction. The driving force of this sub-process, the change of free energy, depends on the deviation between the applied hydrogen pressure p and the corresponding equilibrium pressure p_{eq}. As discussed in detail in subsection 3.2.1, the rate of reaction is a function of the reacted fraction, the temperature and the deviation of p from p_{eq}.

$$\frac{d\alpha}{dt} = \left(Ae^{\frac{-Ea}{RT}}\right) f(p, p_{eq}) g(\alpha) \tag{4.3}$$

The hydrogen absorption rate per unit of volume corresponds to:

$$r'_{abs} = \frac{d\alpha}{dt} w_{\max,H_2} \rho_b \tag{4.4}$$

The function $f(p, p_{eq})$ in Eq. 4.3 is in many cases $(p - p_{eq})/p_{eq}$, e.g. in kinetic expressions for $LaNi_5$ [61], MgH_2 [62], $NaAlH_4$ (Sections 3.2 and 3.3 of this work). This function is a first order approximation of the Taylor series of $\ln(p/p_{eq})$, which defines the change of free energy of the sorption process. Substituting this function into Eq. 4.3, and combining this latter equation with Eq. 4.4 yields:

$$r'_{abs} = \left(\frac{Ae^{\frac{-Ea}{RT}} g(\alpha) w_{Max,H_2} \rho_b}{p_{eq}(T)}\right)\left(p - p_{eq}(T)\right) \tag{4.5}$$

4.1.3 Heat transfer

Heat transfer is the third sub-process that occurs in the hydride bed during hydrogen absorption. The previous sub-process, chemical hydrogen absorption, is a highly exothermal process. The term "highly" is applied since the enthalpy of reaction is able to increment the temperature of the hydride bed several hundreds K. For instance, the temperature can theoretically increase more than 1000 K during the first absorption step in the sodium alanate system (calculated by comparing the energy dissipated due to the enthalpy of reaction and the specific heat of the material). In fact, what actually happens is that the temperature increases up to the corresponding equilibrium temperature of the applied hydrogen pressure. Thus, without proper heat management, the driving force of the chemical reaction is reduced and heat transfer becomes the rate limiting sub-process of the overall sorption process. Proper heat management guarantees that the heat of reaction is transferred through the system to a final sink, e.g. by external convection to a heat oil. The driving force for the heat transfer sub-process is the difference between the temperature of the hydride bed and the temperature of the sink.
Heat transfer in the hydride bed is described by the following thermal energy balance:

$$\left[\varepsilon\left(c_p\rho\right)_g + \left(1-\varepsilon\right)\left(c_p\rho\right)_s\right]\frac{\partial T}{\partial t} + \left(-\lambda_{eff}\nabla^2 T\right) + \left(c_p\rho\right)_g\left(\vec{u}_g \cdot \vec{\nabla} T\right) = r'_{abs}\left(\frac{-\Delta \mathrm{H_R}}{MW_{\mathrm{H_2}}}\right) \qquad (4.6)$$

In the left hand side of Eq. 4.6, the first term is the increment of temperature of the hydride bed (gas and solid phases), the second term is the effective heat conduction (Fourier's law) and the third term is the heat being transported by the stream of gas (convection). The right hand side is the heat source-term, corresponding to the enthalpy of reaction being released during the chemical reaction. Equation 4.6 is an averaged (homogeneous) formulation, which assumes that the temperatures of the solid phase and the gas phase are equal at any point of the hydride bed [44, 59, 63].

4.1.4 Sorption-rate limiting sub-process in a hydride bed

The three described sub-processes occur consecutive and simultaneously in the hydride bed, with mostly different rates that depend on the spatial location inside the bed. The final observed overall hydrogen absorption rate is affected by the interaction of the three sub-processes. It is desired, by means of the model equations presented in the previous subsections, to identify the driving forces of the hydrogen absorption sub-processes, define their resistances, and finally compare the sub-processes by means of these resistances. The analysis of this section makes several simplifications, which will be clarified throughout the explanation. For instance, quasi-steady-state conditions are assumed for the hydrogen absorption. A more rigorous treatment of the model equations is given when solving them by the finite element method, Section 4.2.

If there is no hydrogen accumulation in the gas phase, or if it is neglected in comparison with the magnitude of the other two terms in Eq. 4.2, the integration of Eq. 4.2 with combination of Eq. 4.1 in a one dimensional simple geometry yields:

$$r'_{abs} = \frac{2\rho_g \kappa}{L_{H_2-T}{}^2 \mu}\left(p_{in} - p\right) \tag{4.7}$$

If there is no thermal energy accumulation and convection is neglected, the respective integration of Eq. 4.6 yields:

$$r'_{abs} = \left(\frac{2\lambda_{eff} MW_{H_2}}{L_{HT}{}^2\left(-\Delta \mathrm{H_R}\right)}\right)\left(T - T_0\right) \tag{4.8}$$

Eq. 4.8 will be modified in order to compare the sub-processes with pressure differences as driving force expressions. By using the van 't Hoff equilibrium relation,

$$\ln\left(\frac{p_{eq}(T)}{p_{eq}(T_0)}\right) = \frac{\Delta \mathrm{H_R}}{R}\left(\frac{1}{T} - \frac{1}{T_0}\right) \tag{4.9}$$

The differences $\left(T - T_0\right)$ and $\left(p_{eq}(T) - p_{eq}(T_0)\right)$ may be roughly simplified,

$$\frac{\Delta \mathrm{H_R}}{R}\left(\frac{1}{T} - \frac{1}{T_0}\right) \approx -\frac{\Delta \mathrm{H_R}\left(T - T_0\right)}{R T_0{}^2} \tag{4.10}$$

$$\ln\left(\frac{p_{eq}(T)}{p_{eq}(T_0)}\right) \approx \frac{p_{eq}(T) - p_{eq}(T_0)}{p_{eq}(T_0)} \tag{4.11}$$

Finally, by combining Eqs. 4.8, 4.9, 4.10 and 4.11:

$$r'_{abs} = \left(\frac{2\lambda_{eff} MW_{H_2} T_0^2 R}{L_{HT}{}^2 p_{eq}(T_0)\Delta \mathrm{H_R}{}^2}\right)\left(p_{eq}(T) - p_{eq}(T_0)\right) \tag{4.12}$$

Equations 4.5, 4.7 and 4.12 are used to compare the effect of each sub-process on the overall rate of absorption. It is particularly interesting that these equations suggest an analogy to electrical conduction circuits or heat transfer [64]. Figure 4.1 represents the three sub-processes as three resistances in series analogous to Ohm's law or heat conduction resistances analysis. The analogy is summarized in Eqs. 4.13 to 4.15, and in Table 4.1.

$$r'_{abs} = \frac{\Delta p_i}{R_i} \tag{4.13}$$

$$r'_{abs} = \frac{p_{in} - p_{eq}(T_0)}{R_{abs}} \tag{4.14}$$

$$R_{abs} = R_{H_2-T} + R_{IK} + R_{HT} \tag{4.15}$$

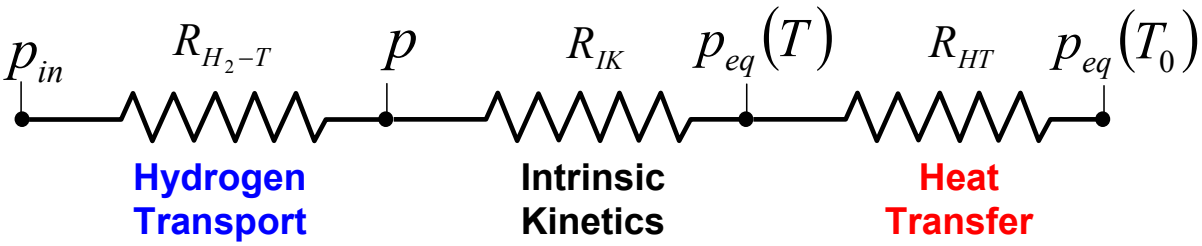

Figure 4.1: Hydrogen sorption sub-processes as a concept of 3 resistances in series where the driving forces are pressure gradients expressions. The intensity of the flow corresponds to the volumetric rate of sorption. Equations 4.5, 4.7 and 4.12 present the relations for the hydrogen transport, chemical reaction and heat transfer, respectively.

Table 4.1: Expressions for driving forces and resistances for the hydrogen absorption sub-processes.

Expression	Hydrogen transport	Intrinsic kinetics	Heat transfer
Sub-process resistance, R_i	$\frac{L_{H_2-T}{}^2 \mu}{2\rho_g \kappa}$	$\frac{p_{eq}(T)}{Ae^{\frac{-E_a}{RT}} g(\alpha) w_{Max,H_2} \rho_{b,m}}$	$\frac{L_{HT}{}^2 p_{eq}(T_0) \Delta H_R{}^2}{2\lambda_{eff} MW_{H_2} T_0^2 R}$
Driving Force (in terms of pressure gradients), Δp_i	$p_{in} - p$	$p - p_{eq}(T)$	$p_{eq}(T) - p_{eq}(T_0)$

According to Eq. 4.14, the overall driving force of the hydrogen absorption process is the difference between the applied hydrogen pressure and the equilibrium pressure at the temperature of the heat transfer medium. The overall resistance is the sum of the three individual resistances, Eq. 4.15. If the order of magnitude of one of the resistances is several times higher than the other two, the overall resistance is defined by this value. Thus, this sub-process would become the absorption-rate limiting sub-process. Important remarks on the resistances:

- **Resistance for hydrogen transport**. On one hand, this resistance is highly dependent on the geometry of the system since it is proportional to the square of the characteristic length for hydrogen transport. On the other hand, the permeability of the hydride bed and this resistance vary inversely. The permeability of the hydride bed can be affected, for instance, by compacting processes, which reduce the void volume for hydrogen transport and decrease therefore the permeability.

- **Resistance for intrinsic kinetics**. This resistance is dependent on the temperature of the system through the Arrhenius factors and the equilibrium pressure. The function $g(\alpha)$, which depends on the transformed fraction α, is the most influential parameter. At low values of the function, e.g. when the transformed fraction approaches one in reactions of first or higher orders, this resistance increases drastically and the absorption process is basically limited by this sub-process.
- **Resistance for heat transfer**. Analogous to the resistance for hydrogen transport, this resistance is proportional to the square of the characteristic length for heat transport. Thus, it is highly dependent upon the geometry and the size of the system. Two other parameters define this resistance: the enthalpy of the reaction and the effective thermal conductivity of the hydride bed.

In system scale-up, as the size of the system increases, the resistances for hydrogen transport and heat transfer become rapidly more influential. Optimised designs, constrained by fast charging times, must focus on maintaining these two transport resistances as low as possible, such that rather intrinsic kinetics define the overall resistance. Furthermore, in investigations on intrinsic kinetics, the resistances of heat transfer and heat transfer must be negligible. This kind of investigations is normally done in cells of small size.

The resistances are calculated for the case of the first absorption step of sodium alanate reacting material at 100 bar H_2 and 125 °C, Fig. 4.2. Three different geometries are evaluated: a) a small cell of diameter of 2 mm, b) the thermocell (15 mm) and the tank (48 mm), see Figs. 2.1, 2.2 and 2.4. The parameters for the calculation are summarized in Table 4.2.

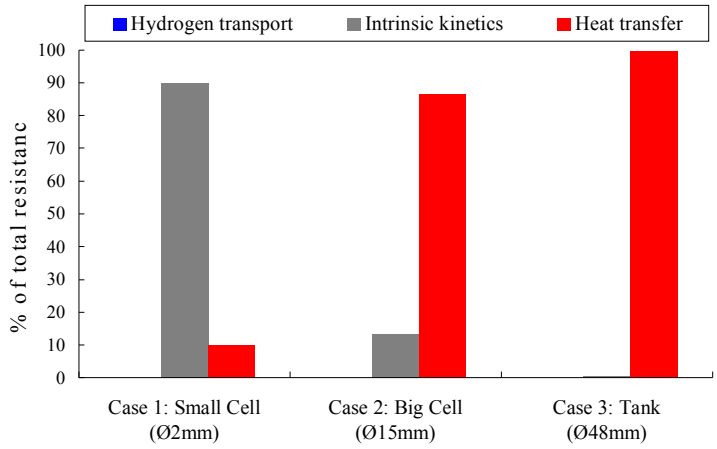

Figure 4.2: Comparison of hydrogen absorption resistances for the first absorption step of sodium alanate reacting material at 100 bar H_2 and 125 °C

Table 4.2: Parameters used for the comparison of hydrogen absorption resistances for the first absorption step of sodium alanate reacting material at 100 bar H_2 and 125 °C

Parameter	Value	Reference
L_{H_2-T}	Small Cell: 0.004 m Big Cell: 0.04 m Tank: 0.04 m	(geometries, see Sections 2.2 and 2.3)
L_{HT}	Small Cell: 0.001 m Big Cell: 0.0072 m Tank: 0.04 m	(geometries, see Sections 2.2 and 2.3)
μ	1.08×10^{-5} kg m^{-1} s^{-1}	[10]
ρ_g	5.81 kg m^{-3}	[10]
κ	3.78×10^{-13} m^2	[44]
T_0	125 °C	-
$p_{eq}(T_0)$	2.60 bar	Eq. 1.3
A	2.28E+08 s^{-1}	Section 3.2
E_a	91.7 kJ mol^{-1}	Section 3.2
$g(\alpha)$	0.133	Section 3.2, Eq. 3.18 $\alpha \approx 0$
ΔH_R	-47 kJ mol H_2^{-1}	[23]
λ_{eff}	0.8 W m^{-1} K^{-1}	Subsection 3.1.3

The comparison shown in Fig. 4.2 demonstrates that for the hydrogen absorption of sodium alanate material the heat transfer resistance is the dominant and rate limiting sub-process, with the exception of small geometries (< 2 mm). It is also found that the resistance due to hydrogen transport is negligible in comparison to the overall absorption resistance. This is mainly due to the high permeability of sodium alanate material as loose powder. As consequence, simulations and designs of scaled-up systems based on sodium alanate material require always heat transfer considerations. Hydrogen transport, on the other hand, may not be necessarily included. Using a similar approach and simplifications, Chaise et al. suggested a criterion to quantify the error when hydrogen transport is neglected, and proved it for different magnesium hydride tanks [63]. This might be not the case when the material is compacted and the porosity reduces and thus the permeability (see Section 5.1)

This is the first time that a resistance analysis is done for the hydrogen absorption sub-processes, and it is not limited to the sodium alanate system. It can be used as tool for a first evaluation of hydrogen transport and heat transfer during scale-up of any hydrogen storage system based on any metal hydride.

4.2 Finite element simulation of the hydrogen sorption of sodium alanate material

As previously shown, pressure, temperature and composition depend upon the spatial location in a hydride bed during a hydrogen sorption process as a consequence of the coupled transport phenomena (heat transfer and hydrogen transport) with chemical reaction. Pressure and temperature spatial profiles inside a hydride bed of sodium alanate material may be neglected and homogeneously assumed only in small geometries, as it was shown in subsection 4.1.4. Since this is not the case in practical systems (Fig. 4.2), numerical simulations are required to solve the model equations that describe the coupled sub-processes of hydrogen transport, intrinsic kinetics and heat transfer in physical geometries. The simulations are mainly conceived to predict the hydrogen sorption behaviour in practical systems based on metal hydrides, in particular on sodium alanate material.

Previously, Franzen developed a numerical simulation for the absorption of sodium alanate [44], which was further extended by Na Ranong for the development of a prototype tank based on sodium alanate [48, 59, 65]. Based on these works, a numerical simulation for the present investigation was further developed. It has the following new features:

- Implementation of the desorption simulation
- New empirical kinetic model for both hydrogen absorption and desorption (see Sections 3.2 and 3.3)
- New approach for the material balance (see 4.2.2 and 4.2.3), which eliminates the use of artificial terms in the kinetic equations (as done in other kinetic models [42-44, 48])
- Experimental validation of the model with the results of the tank station

The numerical simulation of the coupled sub-processes is implemented and solved in COMSOL, a software package that solves partial differential equations by the finite element method [66].

The geometry selected for the simulations is a tubular reactor, like the one used in the experimental investigation of this work (see Figs. 2.4 and 2.5). The cross section of the reactor will be simulated, neglecting possible profiles in the axial direction (2D-Simulation). Figure 4.3 shows the geometric components of the reactor to be simulated, as well as the internal and external boundaries. It must be pointed out, that the developed simulation is not restricted to this geometry and new geometries may

be implemented as well. For instance, different possible configurations of metal hydride systems are well sketched in [67].

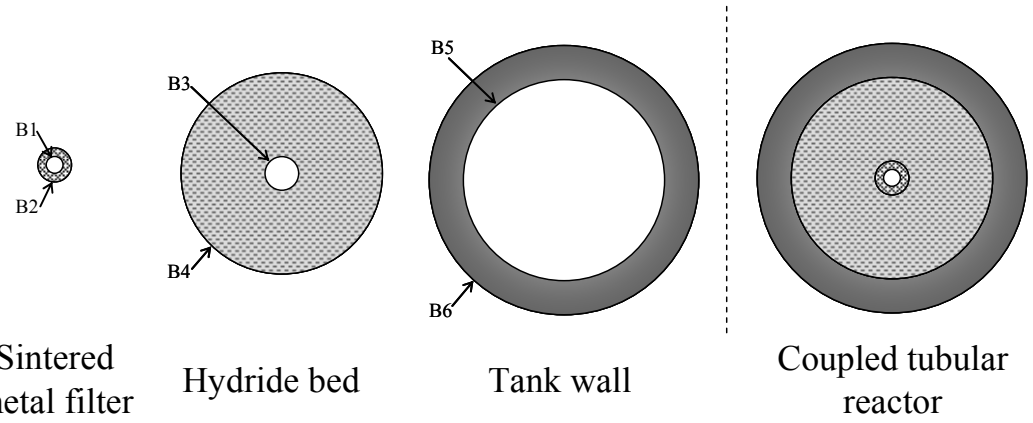

Figure 4.3: Cross-section of a tubular reactor filled with sodium alanate material. Internal and external boundaries are indicated (B1-B6), after [65].

4.2.1 Procedure of the simulation

The simulation of the tubular reactor proceeds according to the following general steps for finite element simulations:

1. **Geometry**. The geometry, i.e. system components, to be simulated must be defined. This can be done directly in the software package or by importing it from standard CAD software.
2. **Governing equations**. The balance equations that describe the physical phenomena to be simulated in the different subdomains are selected or defined.
3. **Initial conditions and boundary conditions**. The initial conditions of the variables and the required parameters in every system component are specified. Boundary conditions are specified for all boundaries of the system components. How these initial and boundary conditions are defined is crucial since the solution of the equations depends strongly on them.
4. **Solution**. The program proceeds to solve the coupled equations in the geometry by using special numerical algorithms. The subdomains are previously discretised by a meshing procedure.
5. **Post-processing**. After the solution is found, further treatment of the solution may be desired for further analysis. For instance, system components and boundary integrations.

For the simulation of the tubular reactor filled with sodium alanate material, the geometry is presented in Fig. 4.3. The physical phenomena to be simulated are hydrogen transport, intrinsic kinetics and heat transfer. The corresponding describing equations of these physical phenomena are summarized in Table 4.3 for the different system components. The boundary conditions are presented in Table 4.4.

Table 4.3: Summary of model equations of the different components of a tubular reactor based on metal hydrides, see Fig. 4.3.

System component	**Hydrogen Transport** Variable: Hydrogen Pressure	**Intrinsic Kinetics** Variables: Reactant mass concentrations	**Heat transfer** Variable: Temperature
Sintered metal filter	Darcy's Law (momentum balance, Eqs. 4.1 and 4.2, $r'_{abs}=0$)	- do not apply -	Heat conduction and convection (Eq. 4.6, $r'_{abs}=0$)
Hydride bed	Darcy's Law (momentum balance, Eqs. 4.1 and 4.2)	Kinetic models (see Sections 4.2.2 and 4.2.3, Eqs. 4.17-4.19 and 4.32-4.34)	Heat conduction and convection, with heat generation (Eq. 4.6)
Tank wall	- do not apply -	- do not apply --	Heat conduction (Eq. 4.6: $\vec{u}_g=0$, $r'_{abs}=0$)

Table 4.4: Boundary conditions for the different physical phenomena defined for a metal hydride tubular reactor, see Fig. 4.3.

Boundary	**Hydrogen Transport** Variable: Hydrogen Pressure	**Intrinsic Kinetics** Variables: Reactant mass concentrations	**Heat transfer** Variable: Temperature
B1	Inlet pressure $p\big\|_{\mathrm{B1}} = p_{inlet}(t)$	- do not apply -	Heat convection $\left(c_p\rho T\right)_g\left(\vec{u}_g\right)\big\|_{inlet} = -\lambda_{eff}\vec{\nabla}T\big\|_{\mathrm{B1}} + \left(c_p\rho T\right)_g\left(\vec{u}_g\right)\big\|_{\mathrm{B1}}$
B2-B3	Pressure continuity $p\big\|_{\mathrm{B2}} = p\big\|_{\mathrm{B3}}$	Insulation $\nabla\gamma\big\|_{\mathrm{B3}} = 0$	Temperature continuity $T\big\|_{\mathrm{B2}} = T\big\|_{\mathrm{B3}}$
B4-B5	Insulation $\nabla p\big\|_{\mathrm{B4-B5}} = 0$	Insulation $\nabla\gamma\big\|_{\mathrm{B4}} = 0$	Temperature continuity $T\big\|_{\mathrm{B4}} = T\big\|_{\mathrm{B5}}$
B6	- do not apply -	- do not apply -	Heat convection to thermal oil $-\lambda\nabla T\big\|_{\mathrm{B6}} = \alpha\left(T - T_{Oil}\right)$

Final results of the simulation are presented in the subsection 4.2.4. Before presenting the final results, the new approach developed during this work for the intrinsic kinetics is in detailed described in the following two subsections. Later on, the simulation will be used to optimise a tubular configuration as the experimental used, see Section 5.2.

4.2.2 Intrinsic kinetics: absorption model

Intrinsic kinetics determines the local rate of reaction in which the chemical transformation proceeds, depending on the local hydrogen pressure, temperature and composition in the hydride bed. To describe and follow this transformation, a new approach is proposed in this investigation, in which the hydride bed of sodium alanate is considered as a mixture of three types of material that composes the reacting system (see subsection 3.2.6.3). Their mass concentrations are used to follow the physical phenomena in the simulation. The mass concentration of a component in the mixture corresponds to its mass divided by the volume of the mixture [68]. Equation 4.16 represents the absorption reacting system as defined in Eqs. 3.7, 3.8 and 3.9. The stoichiometry for the numerical simulation is followed per unit of volume, e.g. in terms of mass concentrations of the materials. It is assumed that the bulk volume of the hydride bed is constant. Equations 4.17 to 4.19 are the fundamental model equations for the finite element absorption simulation. Equations 4.20 and 4.21 are expressions of the instantaneous rate of absorptions in terms of mass concentrations, derived from Eqs. 3.27 and 3.28.

$$\mathrm{S_I} \xrightarrow{r'_{a1}} \mathrm{S_{II}} \xrightarrow{r'_{a2}} \mathrm{S_{III}} \tag{4.16}$$

$$\frac{d\gamma_{\mathrm{S_I}}}{dt} = -r'_{a1} \tag{4.17}$$

$$\frac{d\gamma_{\mathrm{S_{II}}}}{dt} = r'_{a1} - r'_{a2} \tag{4.18}$$

$$\frac{d\gamma_{\mathrm{S_{III}}}}{dt} = r'_{a2} \tag{4.19}$$

$$r'_{a1} = 1.33 k_{\mathrm{S_I \rightarrow S_{II}}} \gamma_{\mathrm{S_I}} \left\{ \ln\left(\frac{\gamma_{\mathrm{S_I}} + \gamma_{\mathrm{S_{II}}}}{\gamma_{\mathrm{S_I}}} \right) \right\}^{0.25} \tag{4.20}$$

$$r'_{a2} = 1.33 k_{\mathrm{S_{II} \rightarrow S_{III}}} \gamma_{\mathrm{S_{II}}} \left\{ \ln\left(\frac{\gamma_{\mathrm{S_{II}}} + \gamma_{\mathrm{S_{III}}}}{\gamma_{\mathrm{S_{II}}}} \right) \right\}^{0.25} \tag{4.21}$$

From the stoichiometry of the system, the volumetric rate of hydrogen absorption is calculated using Eq. 4.22. The volumetric heat of reaction is calculated using Eq. 4.23, which corresponds to the right hand side of Eq. 4.6:

$$r'_{abs} = r'_{a1}\left(\frac{\Delta m_{H_2}}{\Delta m_{S_I}}\right)_{S_I \to S_{II}} + r'_{a2}\left(\frac{\Delta m_{H_2}}{\Delta m_{S_{II}}}\right)_{S_{II} \to S_{III}} = 0.0187 r'_{a1} + 0.0374 r'_{a2} \tag{4.22}$$

$$r'_{a1}\left(\frac{\Delta m_{H_2}}{\Delta m_{S_I}}\right)_{S_I \to S_{II}}\left(\frac{-\Delta H_{R,S_I \to S_{II}}}{MW_{H_2}}\right) + r'_{a2}\left(\frac{\Delta m_{H_2}}{\Delta m_{S_{II}}}\right)_{S_{II} \to S_{III}}\left(\frac{-\Delta H_{R,S_{II} \to S_{III}}}{MW_{H_2}}\right) \tag{4.23}$$

The model equations of intrinsic kinetics are implemented in the simulation for the active material for both absorption steps, and for the active material for the first absorption step only. As indicated in Section 3.2, some fraction of the reacting material is inert during the second absorption step. Table 4.5 shows the mass fraction of the material used in this investigation according to the obtained experimental results in Section (see Section 3.2 and Table 3.4). The mass concentrations of each type of material are also presented, which are calculated from their mass fractions and the experimental bulk density of the loose material (0.6 g ml^{-1}). It is assumed that in the initial conditions of the absorption simulation all material is in the desorbed state S_I.

For material active during the two absorptions steps Eqs. 4.17 and 4.18 are solved. The mass concentration $\gamma_{S_{III}}$ for this type of material is calculated on the basis of the mass conservation:

$$\left(\gamma_{S_I} + \gamma_{S_{II}} + \gamma_{S_{III}}\right)_t = \left(\gamma_{S_I} + \gamma_{S_{II}} + \gamma_{S_{III}}\right)_{t_0} = \text{Constant} \tag{4.24}$$

For material active during the first step of absorption, but inert to the second one, only Eq. 4.17 is solved. For this material, the relation $\gamma_{S_{III}} = 0$ is valid at any time. Therefore, the concentration $\gamma_{S_{II}}$ can be calculated directly from the mass conservation equation (Eq. 4.24).

Table 4.5: Mass fraction and mass concentration of the different type of materials that compose the initial sodium alanate material mixture according to experimental results (see Table 3.4). Bulk density of the initial sodium alanate material mixture is 0.6 g ml^{-1}.

Type of Material	**Mass fraction [-]**	**Mass concentration [kg m^{-3}]**
Active material for both absorption steps	0.5805	348.3
Active material for the first absorption step only	0.2271	136.3
Inert material	0.1924	115.4

The solid density, ρ_s, bulk density (also called apparent density), ρ_b, and porosity of the material, ε, are calculated from the mass concentrations as shown in Eqs. 4.25 to 4.27. The hydrogen-free mass concentrations, γ^0, are based on the stoichiometry definitions of S_I, S_{II} and S_{III}, see Eqs. 4.28 to 4.30

$$\rho_s = \frac{\gamma^0_{S_I} + \gamma^0_{S_{II}} + \gamma^0_{S_{III}} + \gamma_{Inerts}}{\frac{\gamma^0_{S_I}}{\rho^0_{S_I}} + \frac{\gamma^0_{S_{II}}}{\rho^0_{S_{II}}} + \frac{\gamma^0_{S_{III}}}{\rho^0_{S_{III}}} + \frac{\gamma_{Inerts}}{\rho_{Inerts}}} \tag{4.25}$$

$$\rho_b = \gamma^0_{S_I} + \gamma^0_{S_{II}} + \gamma^0_{S_{III}} + \gamma_{Inerts} \tag{4.26}$$

$$\varepsilon = 1 - \frac{\rho_b}{\rho_s} \tag{4.27}$$

$$\gamma^0_{S_I} = 0.9439\gamma_{S_I} \tag{4.28}$$

$$\gamma^0_{S_{II}} = 0.9626\gamma_{S_I} \tag{4.29}$$

$$\gamma^0_{S_{III}} = \gamma_{S_{III}} \tag{4.30}$$

4.2.3 Intrinsic kinetics: desorption model

The simulation of the hydrogen desorption model implements the empirical kinetic model for the hydrogen desorption of sodium alanate material, see Section 3.3. The hydrogen transport and heat transfer equations are the same as for the hydrogen absorption. As done in the absorption model, the new approach proposed for the material composition is used. Mass concentrations are as well used to follow the physical phenomena in the simulation. Equation 4.31 represents the reacting system as defined in Eqs. 3.7, 3.8 and 3.9. Equations 4.32 to 4.34 are the model equations for the finite element desorption simulation. Equations 4.35 and 4.36 are expressions of the instantaneous rate of desorption in terms of mass concentrations, derived from Eqs. 3.43 and 3.44.

$$S_{III} \xrightarrow{r'_{d1}} S_{II} \xrightarrow{r'_{d2}} S_I \tag{4.31}$$

$$\frac{d\gamma_{S_{III}}}{dt} = -r'_{d1} \tag{4.32}$$

$$\frac{d\gamma_{S_{II}}}{dt} = r'_{d1} - r'_{d2} \tag{4.33}$$

$$\frac{d\gamma_{S_I}}{dt} = r'_{d2} \tag{4.34}$$

$$r'_{d1} = k_{S_{III} \to S_{II}} \left(\gamma_{S_{II}} + \gamma_{S_{III}} \right) \tag{4.35}$$

$$r'_{d2} = k_{S_{II} \rightarrow S_I} \gamma_{S_{II}} \tag{4.36}$$

From the stoichiometry of the system, the volumetric rate of hydrogen desorption is calculated using Eq. 4.37. The volumetric heat of reaction is calculated using Eq. 4.38, which corresponds to the right hand side of Eq. 4.6:

$$r'_{des} = r'_{d1} \left(\frac{\Delta m_{H_2}}{\Delta m_{S_{III}}} \right)_{S_{III} \rightarrow S_{II}} + r'_{d2} \left(\frac{\Delta m_{H_2}}{\Delta m_{S_{II}}} \right)_{S_{II} \rightarrow S_I} = 0.0374 r'_{d1} + 0.0187 r'_{d2} \tag{4.37}$$

$$r'_{d1} \left(\frac{\Delta m_{H_2}}{\Delta m_{S_{III}}} \right)_{S_{III} \rightarrow S_{II}} \left(\frac{-\Delta H_{R,S_{III} \rightarrow S_{II}}}{MW_{H_2}} \right) + r'_{d2} \left(\frac{\Delta m_{H_2}}{\Delta m_{S_{II}}} \right)_{S_{II} \rightarrow S_I} \left(\frac{-\Delta H_{R,S_{II} \rightarrow S_I}}{MW_{H_2}} \right) \tag{4.38}$$

The hydrogen desorption model equations are also implemented for two types of material in an analogous way as done in the absorption model. The material that was active for both absorption steps is all initially in the absorbed state S_{III}. The mass conservation, Eq. 4.24, is also used as mass balance equation. On the other hand, the material that was active only for the first step of absorption is present as the intermediate state S_{II}. For this material, only Eq. 4.33 is solved in the implemented application, having $\gamma_{S_{III}} = 0$ kg m^{-3} at any time.

4.2.4 Simulation predictions

The central result of the developed simulation is the prediction of the sorption behaviour of the storage system, which must be validated on the basis of experimental results. The comparison of simulation results and experiments supports the determination of suitable assumptions of parameters and conditions for reliable simulations. The boundary condition of the energy equation at the interior of the sintered metal filter (B1, see Fig. 4.3) is taken as example to illustrate the effect of different assumptions on the simulation results. In particular, the definition of this boundary condition may be ambiguous, and the validation should hint at the most suitable assumption. The predictions from the simulation and the experimental results obtained in the tank station are plotted in Fig. 4.4. The assumptions of the simulations in Fig. 4.4 are described in Table 4.6. A further feature of the simulation is the prediction of the porosity of the hydride bed. Figure 4.5 shows the profile of the predicted porosity of the hydride bed during the absorption.

Table 4.6: Assumptions for the evaluated simulations presented in Fig. 4.4

Simulation	Boundary condition assumption for heat transfer at B1 (see Fig. 4.3)
SIM-1	Heat flux $\left(c_p \rho T\right)_g \left(\vec{u}_g\right)\Big\|_{inlet} = -\lambda_{eff} \vec{\nabla} T\Big\|_{\mathrm{B1}} + \left(c_p \rho T\right)_g \left(\vec{u}_g\right)\Big\|_{\mathrm{B1}}$
SIM-2	Convective flux $-\mathrm{n} \cdot \left(\lambda_{eff} \vec{\nabla} T\Big\|_{\mathrm{B1}}\right) = 0$
SIM-3	Constant temperature $T\Big\|_{\mathrm{B1}} = T\Big\|_{inlet} \; ; \; T\Big\|_{inlet} = 80\ °\mathrm{C}$

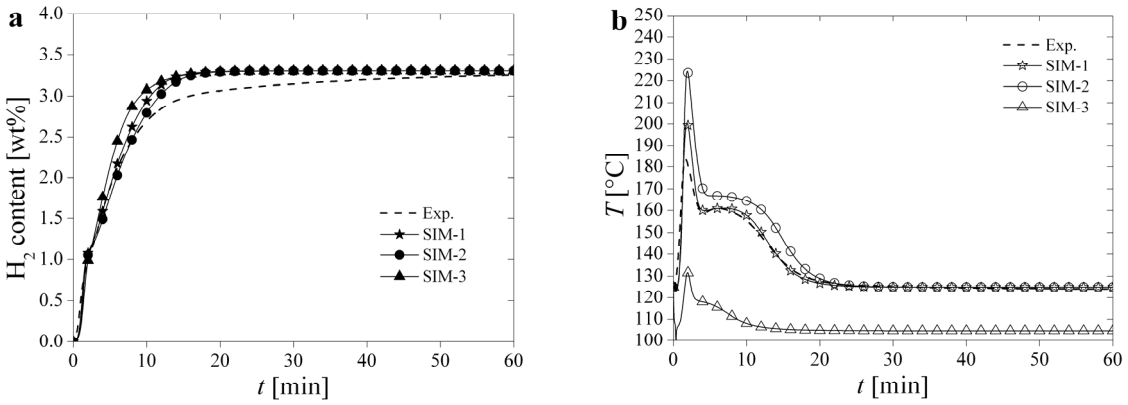

Figure 4.4: Experimental and predicted absorption behaviour in the tubular reactor filled with sodium alanate material: (a) absorbed hydrogen content and (b) course of temperature evolution close to the sintered metal filter

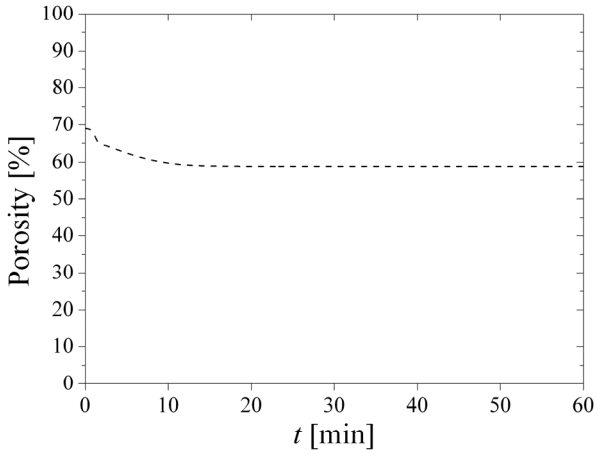

Figure 4.5: Evolution of the porosity according to absorption simulation results

The simulation results of desorption are shown in Fig. 4.6. Boundary condition for the heat transfer at the interior of the sintered metal filter, interface B1 in Fig. 4.3, is redefined for desorption, since in this case the temperature of the hydrogen flowing out corresponds to the same temperature as at this interface (in the case of absorption the temperature of the hydrogen flowing into the sintered filter was different as the temperature at this interface).

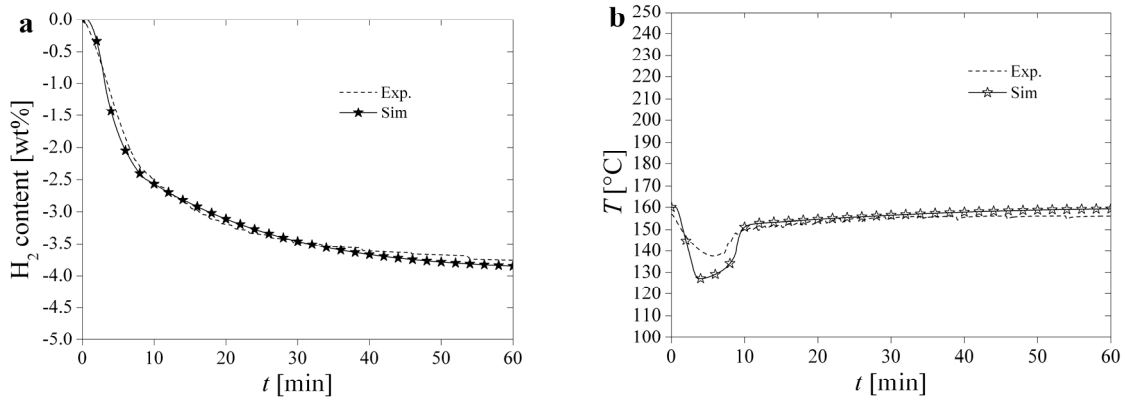

Figure 4.6: Experimental and predicted desorption behaviour in the tubular reactor filled with sodium alanate material: (a) total hydrogen content and (b) course of temperature evolution close to the sintered metal filter

4.2.5 Discussion

Figure 4.4 reveals that best predictions of the experimental results are obtained with the assumptions of simulation SIM-1, in terms of hydrogen sorption behaviour and achieved hydrogen contents, and specifically the profile of the temperature close to the sintered metal filter. SIM-2, in which the cooling effect of the hydrogen inlet-flow is neglected, predicts higher temperature levels. SIM-3, on the other hand, overestimates this cooling effect. The boundary condition of SIM-1 for the energy transport is called Danckwerts condition and was theoretically proposed for the inlet interface of metal hydride storage tanks by Na Ranong [65]. The present results validate the suitable boundary conditions of SIM-1 and therefore it is chosen as the final valid simulation for further analysis. On its basis, the predicted temperature field of the tubular tank during absorption is presented in Fig. 4.7. Initially the hydride bed is isothermal, Fig. 4.7a. When the absorption proceeds, Fig. 4.7b and 4.7c, the released heat of reaction increases the temperature of the bed of hydride and its hottest region is located at a middle radius between the tank wall and the sintered filter. The lower temperature level close to the sintered filter is explained by the convective cooling effect of the hydrogen inlet-flow at the beginning of the absorption. Later on during the absorption, Fig. 4.7d and Fig. 4.7e, the hottest region shifts inwards to the sintered metal filter, because the total hydrogen inlet-flow diminishes and consequently its cooling effect. On the other hand, the coldest region in the hydride bed is close to the tank wall. Although at some moment the temperature in some part of the hydride bed is higher than the equilibrium value for the second absorption step, further reaction is predicted. This can happen since in some other regions of the hydride bed the temperature does not increase beyond this equilibrium value. The temperature of the tank wall remains practically constant and almost identical to the temperature of the heat transfer oil in this example. In contrast to the hydride bed, the thermal conductivity of the tank wall is higher and does not have any heat source. As expected from the resistance analysis of Fig. 4.2, heat transfer through the bed has a strong effect on the sorption performance of the hydride bed. The simulation confirms the resistance analysis also by the predicted pressure gradients in the hydride bed. The analysis predicted a negligible resistance due to hydrogen transport, confirmed by the extremely low pressure gradient in the reactor in the results of the simulated sorption. Nevertheless, it must be stressed that simulation of the hydrogen transport is required due to the heat convection from hydrogen flow, with stronger effect at the beginning of the sorption process. The determined most suitable boundary condition of heat transfer in the inner boundary (B1 in Fig. 4.3) of the simulation strengthens this requirement.

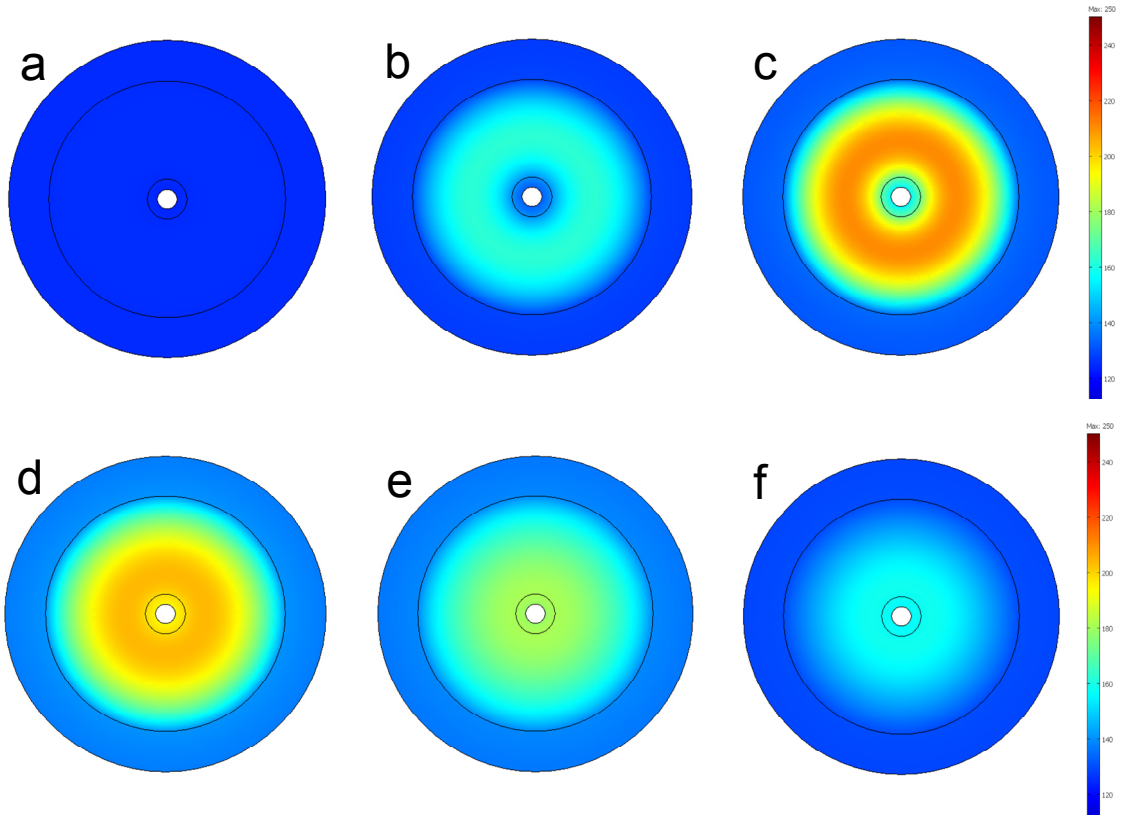

Figure 4.7: Temperature profile of the tubular reactor at different times according to simulation SIM-1: (a) 0.1 min, (b) 1 min, (c) 1.5 min, (d) 2 min, (e) 3 min, (f) 10 min

The porosity of the hydride bed changes as the absorption proceeds, Figure 4.5. The simulation does not assume constant bulk density and thus neither constant porosity of the hydride bed. The porosity depends on the mass concentrations and solid densities of the materials, as shown in Eqs. 4.25 to 4.27. The porosity changes from 70 %, initial state of the hydride bed, to 59 %, final state of the hydride bed. This is due to the lower solid density of the material at the desorbed state in comparison to the absorbed state, also enhanced by the higher total solid mass of the system at the desorbed state.

The simulation results of desorption, Fig. 4.6, show that both predicted temperature profiles and hydrogen content are in good agreement with the experimental results. Heat transfer is not decisive, as desorption is not expected to occur in short time periods. A temperature decrease of only 30 °C during the first part of desorption is predicted, even by high rates of desorption. As desorption proceeds, e.g. after 10 minutes, no noticeable temperature decrease is observed. In other applications at which desorption proceed at a constant rate, smaller temperature decreases may be expected that actually do not influence the overall rate of hydrogen desorption. Further implementation of desorption simulations are e.g. simulations of system integrations of the hydrogen storage tanks being heated-up by the waste heat coming out of hydrogen-based fuel cells.

5 Optimised hydrogen storage systems with sodium alanate material

The use of sodium alanate in a practical hydrogen storage system requires the highest gravimetric capacity and volumetric capacity as possible. This chapter presents combined approaches that optimise hydrogen storage systems based on sodium alanate material. In the first Section of the Chapter, optimisation of the volumetric hydrogen storage capacity is experimentally demonstrated by powder compaction. In the second part, a tubular tank filled with sodium alanate material is theoretically optimised towards its gravimetric hydrogen storage capacity using the obtained experimental results throughout this investigation and the developed simulation tool of Section 4.2.

5.1 Optimising volumetric hydrogen density by compaction

As hydrogen storage option, the major advantage of metal hydrides over compressed hydrogen, even at high pressures, is their greater volumetric hydrogen density. When metal hydrides are handled as powder in a bed, however, the effective volumetric hydrogen density is reduced due to the void volume present inside the bed. For instance, loose sodium alanate material of this investigation has a porosity of more than 60 % (experimental density of the alanate bed is 0.6 g ml^{-1} while the solid density of desorbed initial material is 1.8 g ml^{-1}), i.e. less than half of the volume of the hydride bed is actually occupied by the hydrogen absorbing material. Fortunately, the effective volumetric hydrogen density in a bed can be enhanced by powder densification, i.e. compaction of the material. Compacts of metal hydrides have several advantages over loose powder in a hydride bed. Besides the greater volumetric hydrogen density, compacts are much easier to handle, and their effective thermal conductivity should increase since the particles are closer to each other, facilitating heat conduction through the solid phase. Thus, the heat transfer resistance to sorption is decreased and faster sorption kinetics may be expected. Nevertheless, it should be stressed that the lower porosity of a compact may result in higher resistance to the hydrogen flow and it could become the rate limiting sub-process of the overall hydrogen sorption.

This section presents and discusses the results of the absorption and desorption behaviour of compacts of sodium alanate material which were prepared under different levels of compaction pressure. It is shown that even at high levels of compaction and low porosity, absorption and desorption proceed fast. It is demonstrated that the cycling behaviour is directly related to volumetric expansion of the compact. Important scale-up relevant results, like safety and mechanical stability, are also discussed.

5.1.1 Compacts manufacture

Sodium alanate material in the desorbed state was used for the compacts manufacture, prepared as explained in Section 2.1, including the additional 5 wt% of carbon during milling. All preparation was carried out inside a glove box with purified argon atmosphere. The material was uniaxial compacted and shaped into cylindrical moulds of 4 and 8 mm diameter, using a hydraulic axial press (Enerpac). The compaction pressure was gradually varied from compact to compact, such that different apparent densities and porosities were obtained. The compaction procedure began by filling the loose sodium alanate material in the cavity of the mould. Afterwards, the material was compacted under the desired level of pressure for two minutes. The pressure was subsequently released for a minute. A second consolidation is performed at the same level of compaction pressure for another 2 minutes and the compact is then finally ejected out of the mould.

After manufacture, the apparent density of the compacts was determined by measuring their mass (mg precision scale), and their diameter as well as their thickness (10^{-2} mm precision calliper). The mass of the 4-mm and 8-mm compacts was around 50 mg and 400 mg, respectively. Figure 5.1 summarizes the apparent densities of several manufactured compacts as a function of the applied compaction pressure. The surface of the compacts after preparation and prior to sorption experiments was smooth and even shiny.

A test was done in order to compare pyrophoric behaviour of the compacts in comparison of the powder. First, unconsolidated sodium alanate powder (ca. 30 mg) and 4-mm compacts were exposed to air. As second test, unconsolidated power and compacts were put in contact with water. The tests were carried-out three times, showing the same results. While unconsolidated sodium alanate powder was found to be readily pyrophoric when exposed to air (lot of sparks were observed), compacts did not react at all. In the test with water, the compacts do react but in a quite and calm manner, in contrast to the strong and agitated reaction of the unconsolidated powder.

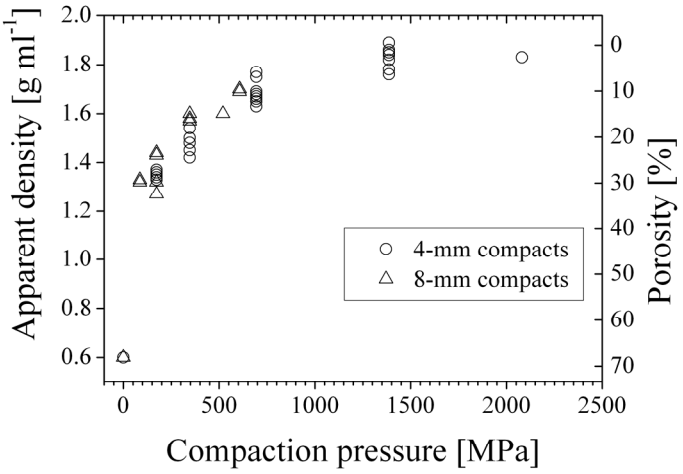

Figure 5.1: Apparent density and porosity of 4-mm and 8-mm compacts of sodium alanate material (desorbed state)

5.1.2 Sorption kinetics

Sorption kinetics of compacts manufactured under different pressures was measured in the Sieverts' apparatus. Hydrogen absorption and desorption of several 4-mm compacts were successfully measured [69]. Figures 5.2 and 5.3 summarize the sorption behaviour of compacts of different apparent densities. One set of was compacted to a still rather low density of 1.3 g ml^{-1}, under a compaction pressure of 200 MPa. The second set was compacted to high density, 1.65 g ml^{-1}, under 700 MPa. Each set consisted of three 4-mm compacts and three 8-mm compacts. Fig. 5.2 shows that the hydrogen absorption of the low density compacts proceeds faster during the first three absorption measurements in comparison to the high density ones. Interestingly, the 5th absorption of the high density compacts proceeds as fast as the low density compacts after the 3rd absorption. Analogous results are found in the hydrogen desorptions, Fig. 5.3. After the second desorption, the low density compacts present already a fast desorption. The second desorption of the high density compacts is still sluggish, but after the 3rd desorption the kinetics are as fast as the 3rd desorption of the low density ones, and the kinetics seems to maintain the same profile in the subsequent desorptions. In addition, the total hydrogen capacity of both types of compacts is surprisingly higher than 4.5 wt%. This value is higher than the total capacity observed during hydrogenation of loose powder and even closer to the theoretical capacity of the material of this investigation, 5.0 wt%.

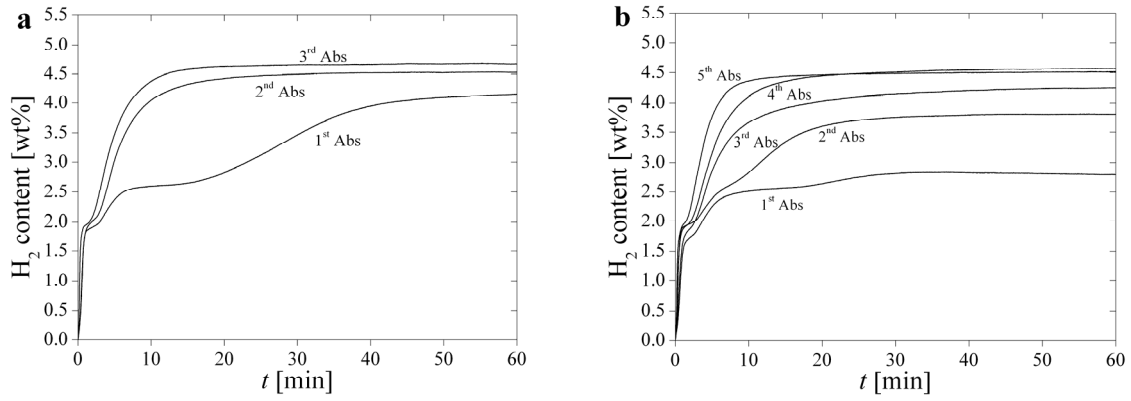

Figure 5.2: Absorptions of sodium alanate compacts at 100 bar and 125 C. (a) Compacts of initial low density (1.3 g ml^{-1}). (b) Compacts of initial high density (1.6 g ml^{-1}).

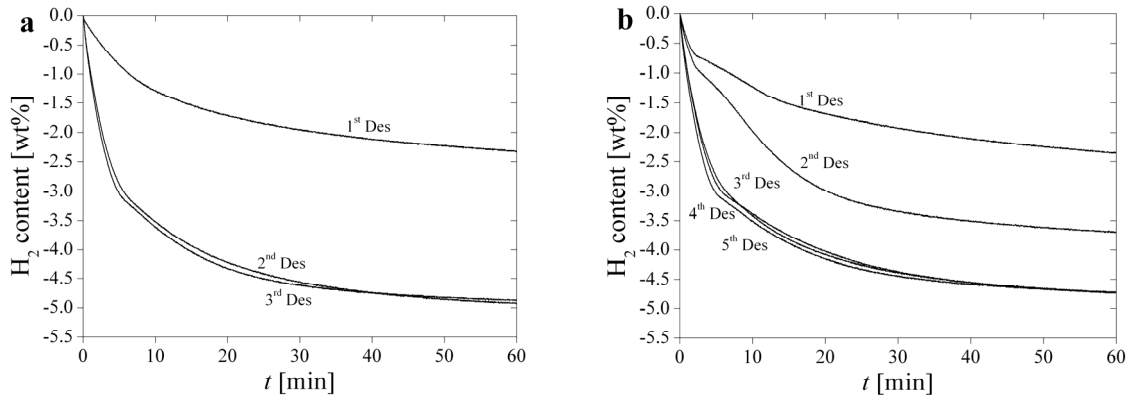

Figure 5.3: Desorptions of sodium alanate compacts at 0 bar and 160 C. (a) Compacts of initial low density (1.3 g ml^{-1}). (b) Compacts of initial high density (1.6 g ml^{-1}).

5.1.3 Apparent density through cycling

After each sorption shown in Figs. 5.2 and 5.3, the cell of the Sieverts' apparatus was dismounted in order to inspect the compacts and to determine their apparent density. Figure 5.4 shows the determined apparent densities of the 4-mm and 8-mm compacts, of both initial low and high density (the low density ones were cycled only 3 times). The apparent densities in Fig. 5.4 correspond to the arithmetic mean of values of the three compacts of the same type. The apparent density measured after the manufacture of the compacts is reported as the initial value. After attaching the cell with the compacts for the first time at the Sieverts' apparatus, they were put under vacuum at 160 °C for 2 hours. The

apparent density after these 2 hours is reported in Fig. 5.4 as 0^{th} desorption. Later on, the apparent densities are reported as the cycling was carried out (absorption-desorption). It is observed that by cycling, the apparent density of the compacts diminishes for both low and high density compacts. This decrease is due to the expansion of the compacts during the sorptions. After several cycles, the apparent density of both low and high density compacts tends to the same value, approx. 1 to 1.1 g ml^{-1}, which corresponds to a porosity of around 45 %. It was also observed in the inspection of compacts that after cycling their surface is neither smooth nor shiny. Marked fissures were also found on the surface of the compacts compacted to high density. This was not observed in the low density compacts.

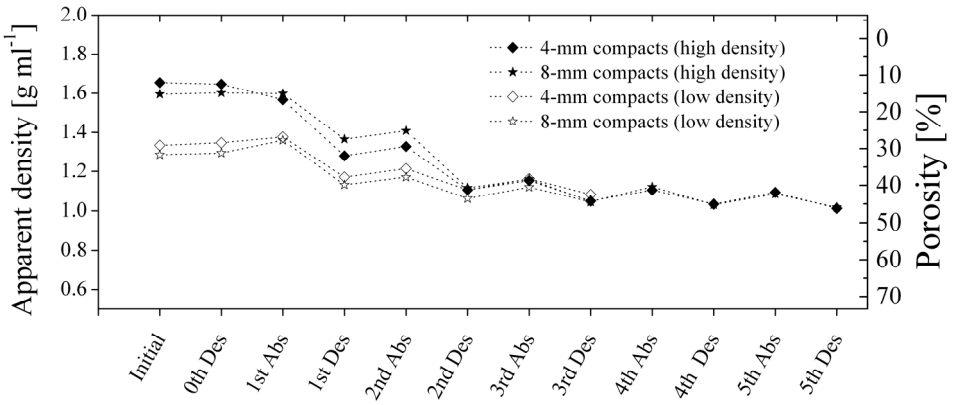

Figure 5.4: Apparent densities of compacts after hydrogen absorptions and desorptions. Compacts were manufactured to low density (1.3 g ml^{-1}) and high density (1.6 g ml^{-1}).

5.1.4 Discussion

Figure 5.1 shows that after consolidation under different pressures, the apparent density of the sodium alanate material compacts can be increased from 0.6 g ml^{-1} to over 1.8 g ml^{-1}. Thus, consolidation can triplicate the effective volumetric hydrogen storage density of the desorbed material. Powder compaction promotes a better packing of the solid particles by rearrangement and further deformation of the particles [70], such that the void interparticulate volume decreases and thus the porosity. It is clearly seen, that the applied compaction pressure has an effect on the apparent density of the manufactured compacts, possibly independent of the size of the compact. Under pressures from 0 MPa up to 700 MPa, the apparent density increases rapidly. At compaction pressures greater than

1400 MPa, the apparent density further increases although slower, asymptotically tending to the theoretical density of the desorbed material (1.88 g ml^{-1}).

The enhancement of sorption kinetics and hydrogen capacity by cycling the compacts of low and high density, shown in Figs. 5.2 and 5.3, is explained by changes of the internal packing arrangement and expansion of the compacts, as well as the increase of the interface area. This is reflected in the evolution of the apparent density, Fig. 5.4. First, it is noted that just the first heating up to 160 °C does not change the apparent density of the compacts. Later, it could be expected that the first hydrogen absorption of the material would decrease the apparent density to a value lower than the theoretical density of $NaAlH_4$, 1.2 g ml^{-1}. However, what really happens is that the material does not fully react. The low porosity of the compact may have had an associated low permeability for hydrogen flow, which caused the lower hydrogen uptake obtained and that the apparent densities stayed over 1.2 g ml^{-1}. After some cycles the apparent density diminishes and the porosity increases: hydrogen reacts with the compacts during absorption and is released during desorption, expanding and fracturing the compact, creating thereby new pathways of flow and thus increasing the permeability and particle interfaces. This resulted in higher hydrogen uptake and faster kinetics. This effect happens in earlier cycles in the low density compacts, since they started with higher porosities than the high density ones. In both cases the apparent density tends to the same value (approx. 1 to 1.1 g ml^{-1}), indicating that the final particle arrangement of the compacts should be quite similar. Nevertheless, the higher expansion of the high density compacts caused fragmentation, which may be an undesired effect if steady shape and integrity of the compacts is desired.

Interestingly, it is during hydrogen desorption when the compact expansion is stronger observed. In order to show this in a clear manner, the dimensional change of the compacts through cycling is shown in Fig. 5.5. Inspection of the change of the volume after the first desorption in comparison to the volume after the first absorption, reveals that during desorption the compacts expand the most. For instance, in Fig. 5.5b the larger change of volume occurs after the first desorption and after the second desorption. In contrast, the expansion during absorptions is less and the compact rather slightly shrinks. These observations may be explained by tensile stresses during hydrogen desorption promoting crack formation by which the particle arrangement in the compact expands. Hydrogen desorption is even used to foam metals (e.g. aluminium and zinc alloys), in which small amounts of metal hydrides (e.g. TiH_2, MgH_2) are mixed with metal powders and afterwards compacted [71]. It is found that when the melting point of the metal is far above than the desorption temperature of the metal hydride, as it is the case of the sodium alanate material, the compact expands in the solid state during hydrogen desorption, yielding crack-like pores [71]. In the case of hydrogen absorption, compressive stress occurs and leads to smaller crack and pore volume fraction in the compact, resulting into the shrinkage of the compact.

Compaction of the powder brings advantages for the storage capacity and safety. Higher hydrogen uptake by the compacts is obtained in comparison to unconsolidated powder. This may be due to narrower pathways for the solid reaction and the lower particle segregation in the compact. Compacts also proved to be safer to handle in contact with air and water compared to the unconsolidated power. The diminished porosity and thus less surface area and lower permeability impede the pyrophoric reaction with air and the strong and agitated reaction with water. All these crucial advantages give the compacts of sodium alanate material great potential for its use in practical hydrogen storage systems. Nevertheless, it must be noted that the expansion of the compact must be considered when determining the internal storage cavity for the compacts. If not additional space is considered, high pressures of the compact against the wall are produced and may damage the container and even cause an explosion. In this sense, the information of the dimensional change can guide the dimensional design of the system. Carefully handled, the radial expansion could be use to reduce the heat transfer resistance to the wall, considering the volume change by means of the height of the compacts.

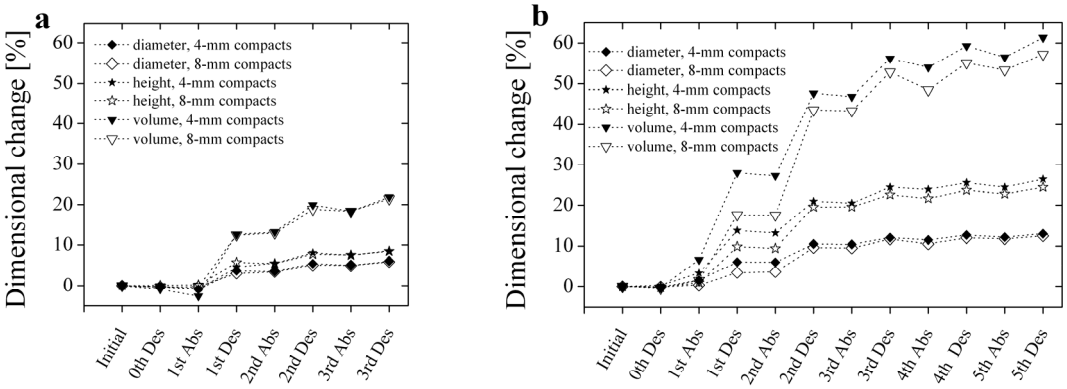

Figure 5.5: Dimensional change of diameter, height and volume of the compacts after different sorptions. (a) Compacts of initial low density (1.3 g ml^{-1}). (b) Compacts of initial high density (1.6 g ml^{-1}).

5.2 Optimisation of tubular storage tanks based on sodium alanate material

Design of practical hydrogen storage systems aims at minimizing their volume and weight while fulfilling defined criteria such as driving ranges in automobile applications and total storage capacities [7, 8]. This section presents the determination of an optimal tubular storage tank design based on

Table 5.1: Optimisation definition for a tubular tank based on sodium alanate material

Issue	Definition
Function to be minimized	Weight of the hydrogen storage system
Variables	1. Internal diameter of the tubular tank 2. Compaction level 3. Addition of expanded graphite
Conditions and constraints	1. The basic configuration of the tubular tank is as presented in Fig. 4.3 2. Time to charge 4.5 kg H_2: 10 min 3. Total hydrogen capacity of the storage system ≥ 5 kg H_2 4. Tank wall thickness must be calculated to hold 100 bar and 250 °C

sodium alanate material for the crucial hydrogen absorption process. The optimisation is carried out on the basis of the predictions of the developed simulation tool for the hydrogen absorption, Section 4.2, supported by the experimental results obtained throughout this investigation.

The optimisation is performed for the case of a tubular tank as presented in Fig. 4.3. Optimisations of tubular tanks filled with loose powder and with compacted material are compared. Compacted material has the advantage over loose powder of higher volumetric hydrogen density and higher thermal conductivity. Nevertheless, the permeability to flow decreases and the volumetric heat release from the hydrogenation is higher. Beyond the possible improvement by compaction, the addition of expanded graphite (EG) is also evaluated in the optimisations. This addition enhances the effective thermal conductivity of the hydride bed, although increasing the amount of inert mass in the system and thus diminishing the total hydrogen storage capacity.

5.2.1 Definition of the tubular tank optimisation

An optimisation is the process of finding the maximum (or minimum) value of a function, by changing the values of a set of variables. Simultaneously, predefined criteria (constraints and conditions) must be fulfilled. Table 5.1 summarizes how the optimisation of a tubular storage tank based on sodium alanate is defined for the present analysis.

The total weight of the hydrogen storage system is composed of the weights of the tank wall, the hydride bed and the sintered filter (Fig. 4.3). The length of the tubular tank is calculated in order to satisfy both conditions 2 and 3 of Table 5.1. The calculation is based on the bulk density of the

hydride bed, ρ_b, and the hydrogen content after 10 minutes that is predicted by the simulation tool. The thickness of the tank wall is calculated according to the temperature and pressure design conditions, see subsection 5.2.1.1. The physical and transport properties of loose powder, compacted material and compacted material with the addition of sodium alanate are discussed in subsection 5.2.1.2.

5.2.1.1 Calculation of the tank wall thickness

The thickness of the tubular tank must hold the stresses due to the hydrogen pressure. The tank wall thickness is calculated according to the technical specifications of the codes of practice on pressure vessels AD 2000 [72] and the norm DIN 17458 [73]. The material of the wall is the standard stainless-steel 1.4571 for hydrogen applications. Equation 5.1 is the basis of the wall thickness calculation for cylinders:

$$s = \frac{D_a p}{20\frac{K}{S}v + p} + c_1 + c_2 \tag{5.1}$$

In Eq. 5.1, s is the required wall thickness [mm], D_a the external diameter of the cylinder [mm], p the design pressure [bar], K the strength coefficient of the wall material [N mm^{-2}], S the design safety factor [-], υ a factor of the utilization of the allowable design stress[-], c_1 and c_2 additional thickness tolerances [mm]. Further details of the calculation procedure and the values of the parameters can be found in the cited references [72, 73]. Table 5.2 presents the values of wall thickness for different tank diameters.

5.2.1.2 Physical and transport properties of the hydride bed

The physical and transport properties of the hydride bed, such as bulk density, thermal conductivity and flow permeability, define the hydrogen sorption resistances (see e.g. Table 4.1) and thus have a main role in the optimisation of the storage system. This subsection summarizes the values assumed for these properties in the simulations and how they are affected by the compaction process and the addition of expanded graphite.

Loose sodium alanate material used in this investigation has an apparent density of 600 kg m^{-3} and a thermal conductivity of 0.8 W m^{-1} K^{-1}, estimated in Section 3.1.3. According to the experimental results on the kinetics of the loose sodium alanate material, Section 3.2, its total hydrogen storage capacity is 3.9 wt%. The flow permeability of the loose powder is 3.17×10^{-13} m^2, as reported by Franzen [44].

Table 5.2: Calculated wall thickness for different tubular tank diameters. The design pressure and temperature are 100 bar and 250 °C, respectively. The material is the austenitic stainless-steel 1.4571. Design safety factor $S = 1.5$.

Internal diameter [mm]	Calculated wall thickness [mm]	External diameter [mm]
20	1.3	22.6
40	2.6	45.2
60	3.9	67.7
80	5.2	90.3
100	6.4	112.9

Compaction of loose powder beds leads to a significant improvement of their effective thermal conductivity [74, 75]. From the results of compaction of magnesium hydride [75], in which the thermal conductivity is multiplied by a factor of 3 when compared to that unconsolidated material, a thermal conductivity of 2 W m^{-1} K^{-1} is expected for the compacts of sodium alanate material. Higher enhancement of compaction is even reported for compacts of conventional metal hydrides [76]. According to the results of Section 5.1, the apparent density of the compacts after cycling is 1100 kg m^{-3} and its total hydrogen storage capacity 4.5 wt%. In order to estimate the change of the flow permeability by compaction and reduction of the porosity, the Blake-Kozeny equation is implemented:

$$\kappa_2 = \kappa_1 \left(\frac{\varepsilon_2}{\varepsilon_1} \right)^3 \left(\frac{1-\varepsilon_1}{1-\varepsilon_2} \right)^2 \tag{5.2}$$

Expanded graphite addition to metal hydride material leads to a significantly improved thermal conductivity, as shown in Section 3.1.4 for loose sodium alanate powder and reported in the literature for metal hydrides compacts [74-77]. Compacts of magnesium hydride with of 5 wt% of expanded graphite have a thermal conductivity of 4 W m^{-1} K^{-1} and with 10 wt% the thermal conductivity goes up to a value of 7 W m^{-1} K^{-1} [75]. These effective thermal conductivities are taken for the simulation predictions of sodium alanate compacts with expanded graphite. The additional inert expanded graphite in the compacts reduces the total hydrogen storage capacity of the material: from 4.5 wt% to 4.3 wt% if 5 wt% of expanded graphite is added, and to 4.05 wt% with an addition of 10 wt% of

expanded graphite. Changes of the bulk density and flow permeability by the addition of expanded graphite are neglected.

5.2.2 Results

The absorption behaviour of tubular tanks of different internal diameters was simulated for loose powder, compacts and compacts with addition of expanded graphite, Fig. 5.6. In the simulations both initial temperature and thermal oil temperature were 110 °C. A constant heat transfer coefficient of 500 W m^{-2} K^{-1} is assumed at the external tank surface. The total system weight according to the conditions of the optimisation is calculated and plotted against the tank internal diameter, Figure 5.7. It is observed that there is a diameter which has a minimum weight of system for each type of material. For loose powder, the minimum total system weight is 640 kg for a tubular tank with an internal diameter of 35 mm. In the case of compacts, with and without EG addition, the minimum system weight is around 350 and 400 kg.

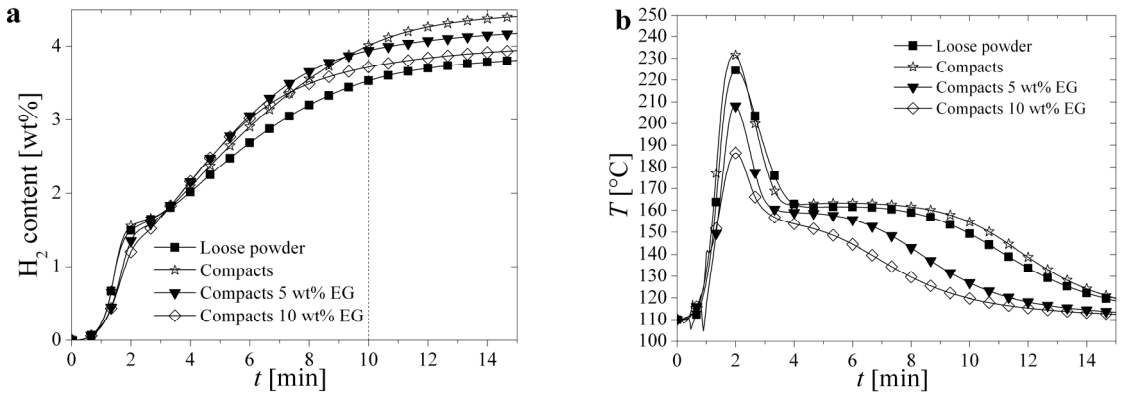

Figure 5.6: Predicted profiles of hydrogen content (a) and temperature close to the sintered filter (b) of a tubular storage tank with D_i=35 mm filled with sodium alanate material. The conditions and constraints are presented in Table 5.1. The initial and oil temperature is 110 °C and the heat transfer coefficient of the oil side is 500 W m^{-2} K^{-1}

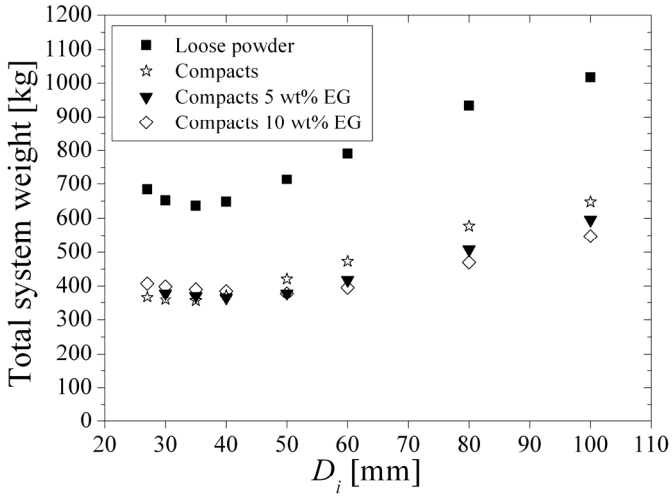

Figure 5.7: Calculated system weight of a tubular storage tank filled with sodium alanate material as a function of the inner diameter. The conditions and constraints are presented in Table 5.1. The initial and oil temperature is 110 °C and the heat transfer coefficient of the oil side is 500 W m^{-2} K^{-1}

5.2.3 Discussion

There are two contrary effects that explain that optimal diameters with minimum total system weight occur for each material in Fig. 5.7. First, as the internal tank diameter is increased, the ratio of mass of hydride bed to mass of tank wall, $m_{\text{Hydride Bed}}/m_{\text{Tank Wall}}$, also increases. Consequently, less inert material (tank wall) per mass of active material is added to the system. The ratio $m_{\text{Hydride Bed}}/m_{\text{Tank Wall}}$ can be calculated from Eq. 5.1, the cross sectional area of the tank, and the densities of the wall and the material. Figure 5.8 shows the calculated ratio $m_{\text{Hydride Bed}}/m_{\text{Tank Wall}}$ for loose material and compacted material as a function of the internal tank diameter. The ratio is 0 when there is not space for the hydride material (when the internal tank diameter is equal to the diameter of the sintered filter, 6 mm). The ratio increases quite fast for internal diameters from 10 mm to 40 mm. For larger diameters the ratio tends asymptotically to a constant value. No noticeable enhancement is noted for internal diameters larger than 70 mm, e.g. less than 1 % enhancement in the ratio $m_{\text{Hydride Bed}}/m_{\text{Tank Wall}}$ is obtained if the diameter goes up to 500 mm. There is an opposed effect when the internal diameter is increased: the resistance to heat transfer and hydrogen transport becomes larger, as shown in Section 4.1.4. As a result, the hydrogen content in the hydride bed after 10 minutes

may be diminished at larger diameters. These two contrary effects lead to an optimal tank diameter, which for the present analysis is around 40 mm according to Fig. 5.7.

Figure 5.8 clarifies why the total weight of system for compacted material is quite lower than for loose material in Fig 5.7. The lower weight of the storage system filled with compacts is explained by the larger bulk density of the compacted material, which causes a larger ratio mass of hydride bed to mass of tank wall in comparison to the loose powder. In addition, as experimentally shown in this investigation, the hydrogen content of loose powder (3.9 wt%) is lower than the one of compacted material (4.5 wt%). Compaction of sodium alanate material causes a total reduction of almost 45 % of the weight of a tubular storage tank, when compared to loose powder. The effect of the lower permeability of the compacted material did not cause any detrimental effect in the absorption behaviour. The predicted pressure gradients that were developed in the hydride bed were quite low for all types of material.

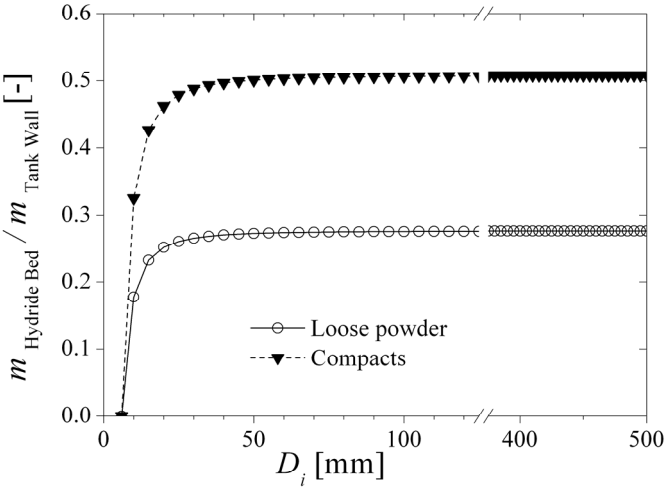

Figure 5.8: Ratio of mass of hydride bed to mass of tank wall as a function of the internal diameter of the tubular tank. The ratio for compacts refers to material with and without addition of expanded graphite.

The additional expanded graphite in the compacted material did not achieve lower optimal system weights (Fig. 5.7). It was expected that the enhanced thermal conductivity through the additional expanded graphite would lead to optimal diameters with less total system weight, since the heat transfer resistance is decreased. The enhancement of the thermal conduction throughout the hydride bed is reflected in the temperature profiles of Fig. 5.6b, with lower and shorter temperature peaks for the material with the addition of expanded graphite. Although it is not considered in the present optimisation, lower levels and peaks of temperature would bring the advantage of possible tank design with thinner walls and options to selection of other lighter wall materials with higher strength (which have a better performance and are more suitable at lower temperatures).

Only at diameters > 40 mm it is observed that the weight of the system is the lowest for compacted material with 5 or 10 wt% of EG. Nevertheless, the overall minimal total system weight is obtained with the compacted material without any addition of EG in a tubular tank of D_i=35 mm. The additional graphite reduces the active material in the tank and therefore more weight is added to the system (see the final hydrogen contents achieved in Fig. 5.6a). Moreover, larger diameters do not enhance the ratio mass of hydride to wall mass enough to compensate the additional inert expanded graphite (Fig. 5.8).

Further optimisations were performed by changing the operating conditions, Figs. 5.9 and 5.10. The initial temperature and the thermal oil temperature is set to 130 °C. In addition, the heat transfer coefficient is changed to 5000 W m^{-2} K^{-1}. No big change is obtained in the minimum total system weights: minimum total system weight is still around 640 kg for loose powder and around 350 and 400 kg for compacted material with and without expanded graphite. Further enhancement of the heat transfer coefficient does not diminish the total weight of the system.

Nevertheless, it must me strengthen that the calculated optimal alanate hydrogen storage system has a higher energy density (2 MJ kg^{-3}, 6 MJ l^{-1}), when compared to lead-acid batteries (0.1 MJ kg^{-3}, 0.4 MJ l^{-1}), nickel-metal hydride batteries (0.4 MJ kg^{-3}, 1.6 MJ l^{-1}) and Lithium-ion batteries (0.6 MJ kg^{-3}, 1 MJ l^{-1}) [78]. Achieving lighter storage systems should concentrate on improving the ratio $m_{\text{Hydride Bed}}/m_{\text{Tank Wall}}$ and the hydrogen storage capacity of the hydride bed. For instance, the hydrogen capacity of the sodium alanate material of this work could be enhanced and optimised by eliminating the carbon addition during milling, which may be not crucial for kinetics but is adding inert material of the system. The excess aluminium in the material (see Table 8.1 in the Appendix), which is adding inert mass to the reacting system as well, can be also optimised: using the exact stoichiometric amount or different aluminium-excess amounts (e.g. considering the possible consumption of aluminium by reacting with titanium), which should bring benefit for hydrogenation kinetics and hydrogen capacity of the material [79]. Another feasible option for lighter storage systems is the evaluation of lighter and hydrogen resistant materials for the tank wall other than the heavy stainless steel (e.g. aluminium alloys, titanium alloys). Materials compatibility studies of sodium alanate with aluminium pressure tanks [80] showed that the integrity of the tank is compromised by the interaction of the tank material with the alanate during cycling (aluminium is consumed in the reverse hydride-formation reactions). A potential material for the pressure tank are light titanium alloys, e.g. $Ti_5Al_{2.5}Sn$, which have been employed as hydrogen tanks and pressure vessels [81]. Since there are not known results with alanate, material compatibility analysis should be done in order to prove that there is not interaction of the material and the alanate.

Furthermore, hydrogen storage materials exhibiting both higher gravimetric and volumetric storage capacity are required in order to achieve lighter storage systems.

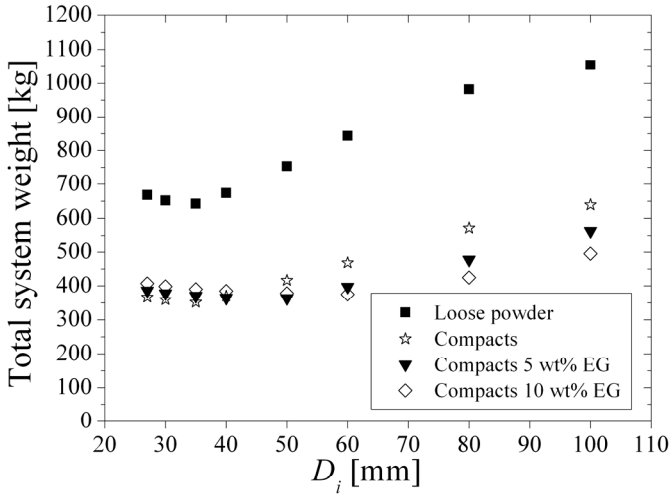

Figure 5.9: Calculated system weight of a tubular storage tank filled with sodium alanate material as a function of the internal diameter. The conditions and constraints are presented in Table 5.1. The initial and oil temperature is 130 °C. The heat transfer coefficient at the oil side of the tubular tank is set to 5000 W m^{-2} K^{-1}

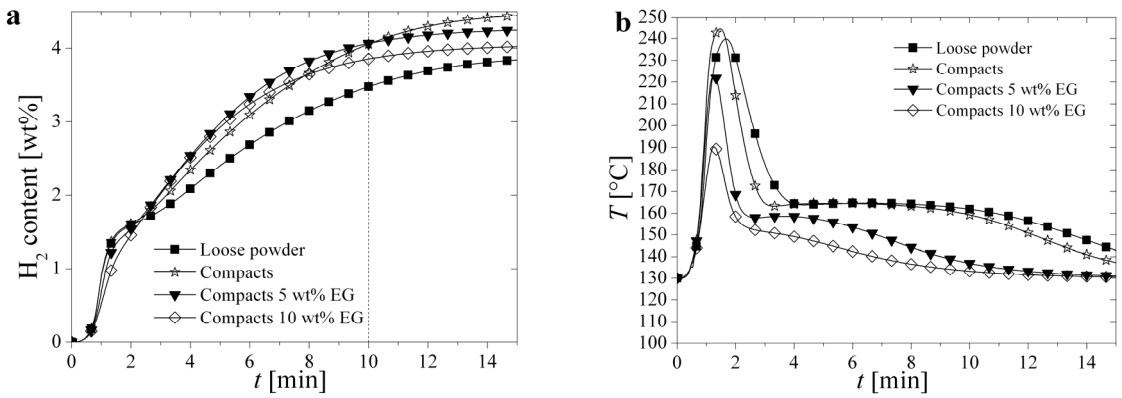

Figure 5.10: Predicted hydrogen content (a) and temperature profiles (b) of a tubular storage tank with D_i =35 mm filled with sodium alanate material. The conditions and constraints are presented in Table 5.1. The initial and oil temperature is 130 °C. The heat transfer coefficient at the oil side of the tubular tank is set to 5000 W m^{-2} K^{-1}

6 Summary

In this work, hydrogen storage systems based on sodium alanate were studied, modelled and optimised, using both experimental and theoretical approaches. The experimental approach covered investigations of the material from mg scale up to kg scale in demonstration test tanks, while the theoretical approach discussed modelling and simulation of the hydrogen sorption process in a hydride bed. Both approaches demonstrated the strong effect of heat transfer on the sorption behaviour of the hydride bed and led to feasible methods to improve and optimise the volumetric and gravimetric capacities of hydrogen storage systems. The applied approaches aimed at an optimal integration of sodium alanate material in practical hydrogen storage systems.

First, it was experimentally shown that the size of the hydride bed influences the hydrogen sorption behaviour of the material. This is explained by the different temperature profiles that are developed inside the hydride bed during the sorptions. In addition, in a self-constructed cell it was possible to follow the hydrogen sorptions and the developed temperature profiles within the bed. Moreover, the effective thermal conductivity of the material was estimated in-situ in this cell, given very good agreement with reported values of ex-situ measurements. It was demonstrated that the effective thermal conductivity of the hydride bed can be enhanced by the addition of expanded graphite. This enhancement promotes lower temperature peaks during the sorptions due to faster heat conduction through the bed, which in addition allows faster heat transfer during sorption.

Looking towards simulations and further evaluations, empirical kinetic models for both hydrogen absorption and desorption of doped sodium alanate were developed. Based on the results of the model, the optimal theoretical pressure-temperature conditions for hydrogen sorptions were determined. A new approach is proposed for the mass balance of the reactions when implementing the model for numerical predictions. This approach describes the material as a mixture composed of different types of reacting materials, which avoids the use of correction terms for the experimental capacities, as it is commonly done in other empirical sorption models for metal hydrides.

To study cycling, kinetics and heat transfer in hydride tanks up to kg scale, a hydrogen tank station was designed and constructed. The sorption behaviour of sodium alanate storage tanks was evaluated, and it was confirmed, that the addition of expanded graphite improves the heat transfer resulting in faster hydrogenation kinetics.

The hydrogen sorption process of practical systems based on hydride beds was modelled for the simultaneous sub-processes of hydrogen transport, intrinsic reaction and heat transfer. Based on the modelling equations, a comparative resistance analysis was developed in order to quantify the effect of each sub-process on the overall sorption kinetics in sodium alanate beds. It was found that large size systems are mainly heat transfer limited. Moreover, on the basis of the modelling equations, a numerical simulation was developed. The simulation was validated with the experimental results obtained in this work.

Optimisation of the volumetric hydrogen storage capacity of sodium alanate based hydrogen storage tanks is experimentally demonstrated by powder compaction. Quite interesting results are discovered on the sorption behaviour of these manufactured compacts: sorption improvement and volumetric expansion of the pellets through cycling as well as enhanced volumetric and gravimetric hydrogen storage capacity of the material. To conclude the work, a tubular tank filled with sodium alanate material was theoretically optimised towards its gravimetric hydrogen storage capacity using the developed simulation and the results obtained during this investigation. The optimisation process includes the evaluation of compaction, the addition of expanded graphite and different tank diameters. It was found that compaction of the material is the most influential factor to optimise the hydrogen capacity of the storage system. Achieving lighter systems should concentrate on improving the ratio $m_{\text{Hydride Bed}}/m_{\text{Tank Wall}}$ and the hydrogen storage capacity of the hydride bed. For instance, the hydrogen capacity of the sodium alanate material of this work could be enhanced by eliminating the carbon addition during milling and the excess aluminium in the material. Another feasible option is to evaluate lighter and hydrogen resistant materials for the tank wall other than the heavy stainless steel. Furthermore, hydrogen storage materials exhibiting both higher gravimetric and volumetric storage capacity are required in order to achieve lighter storage systems.

The scale-up strategy and findings of this work are not limited to the sodium alanate reacting system and may be easily extended to other metal hydride reacting systems.

7 References

[1] International Energy Agency. Key World Energy Statistics 2009. 2009. http://www.iea.org/textbase/nppdf/free/2009/key_stats_2009.pdf; [viewed 12.02.2010]

[2] BP Statistical Review of World Energy June 2009. 2009. http://www.bp.com/liveassets/bp_internet/globalbp/globalbp_uk_english/reports_and_publications/statistical_energy_review_2008/STAGING/local_assets/2009_downloads/statistical_review_of_world_energy_full_report_2009.pdf; [viewed 12.02.2010]

[3] Oil Depletion Analysis Centre and Post Carbon Institute. Preparing for peak oil. 2008. http://www.odac-info.org/sites/default/files/Preparing_for_Peak_Oil_0.pdf; [viewed 12.02.2010]

[4] International Energy Agency. World Energy Outlook 2009. 2009. http://www.worldenergyoutlook.org/docs/weo2009/WEO2009_es_english.pdf; [viewed 14.02.2010]

[5] National Aeronautics and Space Administration. Sun Worldbook. 2009. http://www.nasa.gov/worldbook/sun_worldbook.html; [viewed 12.02.2010]

[6] Colella W.G., Jacobson M.Z., Golden D.M. Switching to a U.S. hydrogen fuel cell vehicle fleet: The resultant change in emissions, energy use, and greenhouse gases. J. Power Sources 2005;150:150-181.

[7] StorHy. StorHy Final Publishable Activity Report. 2008. http://www.storhy.net/pdf/StorHy_FinalPublActivityReport_FV.pdf; [viewed 02.10.2009]

[8] US Department of Energy. Targets of onboard hydrogen storage systems. http://www1.eere.energy.gov/ohydrogenandfuelcells/storage/pdfs/targets_onboard_hydro_storage.pdf; [viewed 12.02.2010]

[9] Züttel A., Borgschulte A., Schlapbach L., editors. Hydrogen as a future energy carrier. Weinheim: Wiley, 2008.

[10] Vargaftik N.B. Handbook of physical properties of liquids and gases: pure substances and mixtures. 2nd Edition. Washington: Hemisphere publishing corporation, 1983.

[11] Aceves S.M., Espinosa-Loza F., Ledesma-Orozco E., Ross T.O., Weisberg A.H., Brunner T.C., Kircher O. High-density automotive hydrogen storage with cryogenic capable pressure vessels. Int. J. Hydrogen Energy 2010;35:1219-1226.

[12] Ahluwalia R.K., Hua T.Q., Peng J.K., Lasher S., McKenney K., Sinha J., Gardiner M. Technical assessment of cryo-compressed hydrogen storage tank systems for automotive applications. Int. J. Hydrogen Energy 2010;35:4171-4184.

[13] Schlapbach L., Züttel A. Hydrogen-storage materials for mobile applications. Nature 2001;414:353-358.

[14] Schulz R., Boily S., Zaluski L., Zaluska A., Tessier P., Ström-Olsen J.O. In: Proceedings of the International Conference on Composite Materials and Energy—ENERCOMP 95 (8–10 May 1995)—Innovations in Metallic Materials 1995:p. 529.

[15] Oelerich W., Klassen T., Bormann R. Metal oxides as catalysts for improved hydrogen sorption in nanocrystalline Mg-based materials. J. Alloys Compd. 2001;315:237-242.

[16] Barkhordarian G., Klassen T., Bormann R. Effect of Nb2O5 content on hydrogen reaction kinetics of Mg. J. Alloys Compd. 2004;364:242-246.

[17] Bogdanovic B., Schwickardi M. Ti-doped alkali metal aluminium hydrides as potential novel reversible hydrogen storage materials. J. Alloys Compd. 1997;253-254:1-9.

[18] Züttel A., Wenger P., Rentsch S., Sudan P., Mauron P., Emmenegger C. LiBH4 a new hydrogen storage material. J. Power Sources 2003;118:1-7.

[19] Barkhordarian G., Klassen T., Bormann R. Patent pending, German Pub. No: DE102004/061286, priority 2004.

[20] Barkhordarian G., Klassen T., Dornheim M., Bormann R. Unexpected kinetic effect of MgB2 in reactive hydride composites containing complex borohydrides. J. Alloys Compd. 2007;440:L18-L21.

[21] Dornheim M., Eigen N., Barkhordarian G., Klassen T., Bormann R. Tailoring Hydrogen Storage Materials Towards Application. Advanced Engineering Materials 2006;8:377-385.

[22] Bösenberg U., Doppiu S., Mosegaard L., Barkhordarian G., Eigen N., Borgschulte A., Jensen T.R., Cerenius Y., Gutfleisch O., Klassen T., Dornheim M., Bormann R. Hydrogen sorption properties of MgH2-LiBH4 composites. Acta Materialia 2007;55:3951-3958.

[23] Bogdanovic B., Brand R.A., Marjanovic A., Schwickardi M., Tölle J. Metal-doped sodium aluminium hydrides as potential new hydrogen storage materials. J. Alloys Compd. 2000;302:36-58.

[24] Eigen N., Keller C., Dornheim M., Klassen T., Bormann R. Industrial production of light metal hydrides for hydrogen storage. Scripta Mater. 2007;56:847-851.

[25] Eigen N., Gosch F., Dornheim M., Klassen T., Bormann R. Improved hydrogen sorption of sodium alanate by optimized processing. J. Alloys Compd. 2008;465:310-316.

[26] Eigen N., Kunowsky M., Klassen T., Bormann R. Synthesis of NaAlH4-based hydrogen storage material using milling under low pressure hydrogen atmosphere. J. Alloys Compd. 2007;430:350-355.

[27] Bouaricha S., Dodelet J.P., Guay D., Huot J., Schulz R. Activation characteristics of graphite modified hydrogen absorbing materials. J. Alloys Compd. 2001;325:245-251.

[28] Dal Toè S., Lo Russo S., Maddalena A., Principi G., Saber A., Sartori S., Spataru T. Hydrogen desorption from magnesium hydride-graphite nanocomposites produced by ball milling. Materials Science and Engineering B 2004;108:24-27.

[29] Imamura H., Sakasai N. Hydriding characteristics of Mg-based composites prepared using a ball mill. J. Alloys Compd. 1995;231:810-814.

[30] Imamura H., Sakasai N., Fujinaga T. Characterization and hydriding properties of Mg-graphite composites prepared by mechanical grinding as new hydrogen storage materials. J. Alloys Compd. 1997;253-254:34-37.

[31] Bellosta von Colbe J.M., Bogdanovic B., Felderhoff M., Pommerin A., Schuth F. Recording of hydrogen evolution--a way for controlling the doping process of sodium alanate by ball milling. J. Alloys Compd. 2004;370:104-109.

[32] Schulz R., Huot J., Boily S. Equipment fo gas titration and cycling of an absorbent or adsorbent material. Can. Patent.,Ser.-Nr. 2207149. 1999.

[33] Swagelok. Catalogue of Swagelok products compliant with the transportable pressure equipment directive (TPED). 2008. http://www.swagelok.com/downloads/webcatalogs/EN/MS-02-193-E.pdf; [viewed 10.11.2009]

[34] Lozano G.A. H2-Beladungsstation - Beschreibung, Bedienungsanleitung und Sicherheitskonzept. Geesthacht: GKSS Forschungszentrum - Intern, 2008.

[35] Lozano G.A., Eigen N., Keller C., Dornheim M., Bormann R. Effects of heat transfer on the sorption kinetics of complex hydride reacting systems. Int. J. Hydrogen Energy 2009;34:1896-1903.

[36] Lozano G.A., Na Ranong C., Bellosta von Colbe J.M., Bormann R., Fieg G., Hapke J., Dornheim M. Empirical kinetic model of sodium alanate reacting system (I). Hydrogen absorption. Int. J. Hydrogen Energy 2010;35:6763-6772.

[37] Lozano G.A., Na Ranong C., Bellosta von Colbe J.M., Bormann R., Fieg G., Hapke J., Dornheim M. Empirical kinetic model of sodium alanate reacting system (II). Hydrogen desorption. Int. J. Hydrogen Energy 2010;35:7539-7546.

[38] Pierson H.O. Handbook of carbon, graphite, diamond and fullerenes. New Jersey: Noyes publications, 1993.

[39] Perry R.H., Green D. Perry's Chemical Engineers' Handbook. 6th Edition. USA: McGraw-Hill, 1984.

[40] Wang K., Wu J.Y., Wang R.Z., Wang L.W. Effective thermal conductivity of expanded graphite-CaCl2 composite adsorbent for chemical adsorption chillers. Energy Conversion and Management 2006;47:1902-1912.

[41] Dedrick D.E., Kanouff M.P., Replogle B.C., Gross K.J. Thermal properties characterization of sodium alanates. J. Alloys Compd. 2005;389:299-305.

[42] Luo W., Gross K.J. A kinetics model of hydrogen absorption and desorption in Ti-doped NaAlH4. J. Alloys Compd. 2004;385:224-231.

[43] Tang X., Mosher D.A., Anton D.L. Practical sorption kinetics of TiCl3 catalyzed NaAlH4. Mater. Res. Soc. Symp. Proc. 2005;Vol 884E:GG4.4.

[44] Franzen J. Modellierung und Simulation eines Wasserstoffspeichers auf der Basis von Natriumalanat. VDI-Fortschrittsberichte, 6 (583), VDI-Verlag, Düsseldorf 2009.

[45] Rudman P.S. Hydriding and dehydriding kinetics. Journal of the Less Common Metals 1983;89:93-110.

[46] Barkhordarian G., Klassen T., Bormann R. Kinetic investigation of the effect of milling time on the hydrogen sorption reaction of magnesium catalyzed with different Nb2O5 contents. J. Alloys Compd. 2006;407:249-255.

[47] Davis J.R., editor. Stainless steels. Materials Park, Ohio: ASM International, 1994.

[48] Na Ranong C., Höhne M., Franzen J., Hapke J., Fieg G., Dornheim M., Eigen N., Bellosta von Colbe J.M., Metz O. Concept, Design and Manufacture of a Prototype Hydrogen Storage Tank Based on Sodium Alanate. Chemical Engineering & Technology 2009;32:1154-1163.

[49] Kircher O., Fichtner M. Hydrogen exchange kinetics in NaAlH4 catalyzed in different decomposition states. J. Appl. Phys. 2004;95:7748-7753.

[50] Brinks H.W., Jensen C.M., Srinivasan S.S., Hauback B.C., Blanchard D., Murphy K. Synchrotron X-ray and neutron diffraction studies of NaAlH4 containing Ti additives. J. Alloys Compd. 2004;376:215-221.

[51] Sandrock G., Gross K.J., Thomas G. Effect of Ti-catalyst content on the reversible hydrogen storage properties of the sodium alanates. J. Alloys Compd. 2002;339:299-308.

[52] Kircher O., Fichtner M. Kinetic studies of the decomposition of NaAlH4 doped with a Ti-based catalyst. J. Alloys Compd. 2005;404-406:339-342.

[53] Kiyobayashi T., Srinivasan S.S., Sun D., Jensen C.M. Kinetic Study and Determination of the Enthalpies of Activation of the Dehydrogenation of Titanium- and Zirconium-Doped NaAlH4 and Na3AlH6. J. Phys. Chem. A. 2003;107:7671-7674.

[54] Bellosta von Colbe J.M., Felderhoff M., Bogdanovic B., Schuth F., Weidenthaler C. One-step direct synthesis of a Ti-doped sodium alanate hydrogen storage material. Chemical Communications 2005;37:4732-4734.

[55] Züttel A. Demonstration eines Metallhydrid Speichers in einem mit Wasserstoff angetriebenen Pistenfahrzeug. Schluss Bericht 2004. Swiss Federal Office of Energy, Fribourg 2004.

[56] Friedrich B. Large-scale production and quality assurance of hydrogen storage (battery) alloys. J. Mater. Eng. Perform. 1994;3:37-46.

[57] Tölle J. Ti- oder Ti- und Fe- dotierte Natriumalanate als neue reversible Wasserstoffspeicermaterialien. Dissertation, Max-Planck-Institut für Kohlenforschung, Mülheim an der Ruhr 1998.

[58] VDI Wärmeatlas. 10th Edition. Düsseldorf: VDI Verlag, 2002.

[59] Na Ranong C., Höhne M., Franzen J., Hapke J., Fieg G., Dornheim M. Modellgestützte verfahrenstechnische Berechnung eines Metallhydridspeichers auf Natriumalanatbasis im Technikumsmaßstab. Chemie Ingenieur Technik 2009;81:645-654.

[60] Nield D.A., Bejan A. Convection in Porous Media. 2nd Edition. New York: Springer-Verlag, 1999.

[61] Botzung M., Chaudourne S., Gillia O., Perret C., Latroche M., Percheron-Guegan A., Marty P. Simulation and experimental validation of a hydrogen storage tank with metal hydrides. Int. J. Hydrogen Energy 2008;33:98-104.

[62] Marty P., Fourmigue J.F., de Rango P., Fruchart D., Charbonnier J. Numerical simulation of heat and mass transfer during the absorption of hydrogen in a magnesium hydride. Energy Conversion and Management 2006;47:3632-3643.

[63] Chaise A., Marty P., De Rango P., Fruchart D. A simple criterion for estimating the effect of pressure gradients during hydrogen absorption in a hydride reactor. Int. J. Heat Mass Transfer 2009;52:4564-4572.

[64] Incropera F.P., DeWitt D.P. Fundamentos de transferencia de calor. 4th Edition. México: Prentice Hall, 1999.

[65] Na Ranong C., Hapke J., Höhne M., Fieg G., Bellosta von Colbe J.M. Modelling and simulation of a large-scale metal-hydride storage tank on the basis of sodium alanate. 7th International Conference on Heat Transfer, Fluid Mechanics and Thermodynamics. Antalya, Turkey, 2010.

[66] Comsol Multiphysics Version 3.4. Computer Software, COMSOL AB. Copyright 1994-2007

[67] Höhne M. Simulation und Optimierung eines thermischen Energiespeichers auf Metallhydridbasis. VDI-Fortschrittsberichte, 3 (812), VDI-Verlag, Düsseldorf 2004.

[68] IUPAC. Compendium of Chemical Terminology, 2nd ed. (the "Gold Book"). Compiled by A. D. McNaught and A. Wilkinson. doi:10.1351/goldbook. Oxford: Blackwell Scientific Publications, 1997.

[69] Meyer D. Effekt der Kompaktierung auf das Wasserstoffspeicherverhalten von Natriumalanat. Bachelorarbeit, Helmut-Schmidt-Universität / Universität der Bundeswehr Hamburg, Hamburg 2009.

[70] German R.M. Powder metallurgy science. Princeton: Metal powder industries federation, 1984.

[71] von Zeppelin F., Hirscher M., Stanzick H., Banhart J. Desorption of hydrogen from blowing agents used for foaming metals. Composites Science and Technology 2003;63:2293-2300.

[72] AD 2000 Regelwerk. 5. Auflage. Berlin: Verband der TÜV e.V., 2008.

[73] Norm DIN 17458, Nahtlose kreisförmige Rohre aus austenitischen nichtrostenden Stählen für besondere Anforderungen.

[74] Rodríguez Sánchez A., Klein H.-P., Groll M. Expanded graphite as heat transfer matrix in metal hydride beds. Int. J. Hydrogen Energy 2003;28:515-527.

[75] Chaise A., de Rango P., Marty P., Fruchart D., Miraglia S., Olivès R., Garrier S. Enhancement of hydrogen sorption in magnesium hydride using expanded natural graphite. Int. J. Hydrogen Energy 2009;34:8589-8596.

[76] Klein H.-P., Groll M. Heat transfer characteristics of expanded graphite matrices in metal hydride beds. Int. J. Hydrogen Energy 2004;29:1503-1511.

[77] Kim K.J., Montoya B., Razani A., Lee K.H. Metal hydride compacts of improved thermal conductivity. Int. J. Hydrogen Energy 2001;26:609-613.

[78] ETHZ Merkblatt Batterien und Akkus. 2003. http://www2.ife.ee.ethz.ch/~rolfz/batak/Merkblatt_Batterien_und_Akkus.pdf; [viewed 23.06.2010]

[79] Johnson T.A., Dedrick D.E., Stephens R.D., Chan J.P. Sodium Alanate Hydrogen Storage Material. U.S. Patent.,Pub.-Nr. US 2007/0178042 A1. 2007.

[80] Gross K.J., Majzoub E., Thomas G.J., Sandrock G. Hydride development for hydrogen storage. Proceedings of 2002 U.S. DOE hydrogen program review (NREL/CP-610-32405). Golden, CO., 2002.

[81] Peters M., Leyens C. Titan und titanlegierungen. Weinheim: Wiley-VCH, 2002.

8 Appendix

8.1 Material balance and hydrogen capacity

The mass composition of the initial sodium alanate material in the desorbed state is based on the reaction in Eq. 8.1, which is expected to occur during milling (as prepared in this investigation). The results of the material balance are shown in Table 8.1, including the addition of 5 wt% of carbon and the excess of aluminium coming from the catalyst precursor. In the calculations for the material balance, the possible consumption of aluminium by the reaction with titanium was not considered.

$$1.08\,NaH + Al + 0.02(TiCl_3 + \tfrac{1}{3}AlCl_3) \rightarrow NaH + 1.0067Al + 0.08NaCl + 0.02Ti + 0.04H_2 \quad (8.1)$$

Table 8.1: Material balance of the initial sodium alanate material of this work in the desorbed state after milling, according to Eq. 8.1. Basis of calculation is 1 mol of NaH.

Compound	Molar mass [g mol^{-1}]	Amount [mol]	Mass [g]	Mass fraction [-]
NaH	24.00	1	24.00	0.402
Al	26.98	1	26.98	0.453
Inerts:				
Al (excess)	26.98	0.0067	0.18	0.003
NaCl	58.44	0.08	4.68	0.078
Ti	47.88	0.02	0.96	0.016
C (5 wt%)	12.01	0.237	2.85	0.048
Total Inerts	-	-	8.66	0.145
Total	-	-	59.64	1.000

The absorption equations of the sodium alanate material are written including inert solid material, Eqs. 8.2 and 8.3. Table 8.2 summarizes the hydrogen capacities of both hydrogenation steps according to the material balance presented in Table 8.1 and Eqs. 8.2 and 8.3.

$$NaH + Al + Inerts + \tfrac{1}{2}H_2 \leftrightarrow \tfrac{1}{3}Na_3AlH_6 + \tfrac{2}{3}Al + Inerts \quad (8.2)$$

$$\tfrac{1}{3}Na_3AlH_6 + \tfrac{2}{3}Al + Inerts + H_2 \leftrightarrow NaAlH_4 + Inerts \quad (8.3)$$

Table 8.2: Hydrogen capacities of the sodium alanate material of this work including inert material.

Step reaction	**H_2 absorbed [g]**	**H_2 capacity [wt%] (based on the desorbed state)**	**H_2 capacity [wt%] (based on the absorbed state)**
First step	1.01	1.69	1.67
Second step	2.02	3.33	3.22
Both Steps	3.03	5.08	4.89

8.2 Interface and diagrams of the tank station

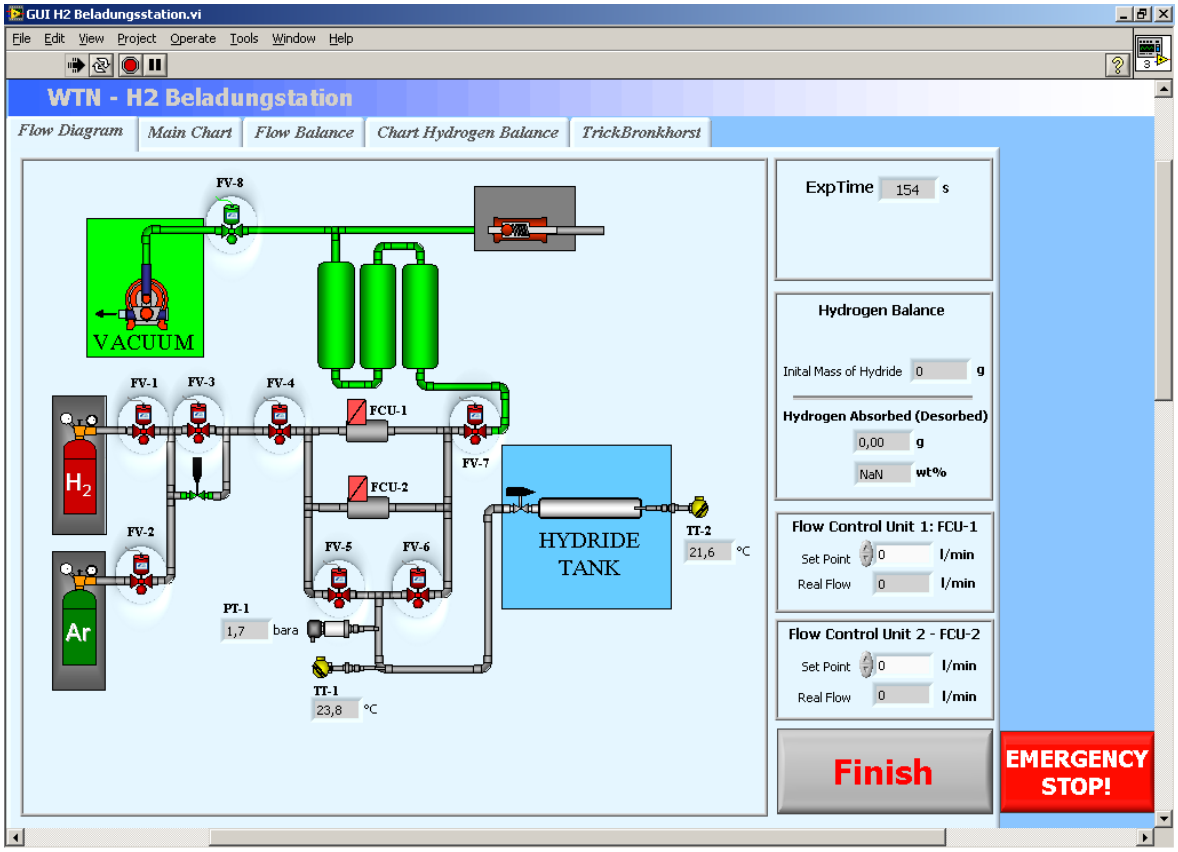

Figure 8.1: Snap-shot of the GUI (graphical user interface) of the software application of the hydrogen tank station.

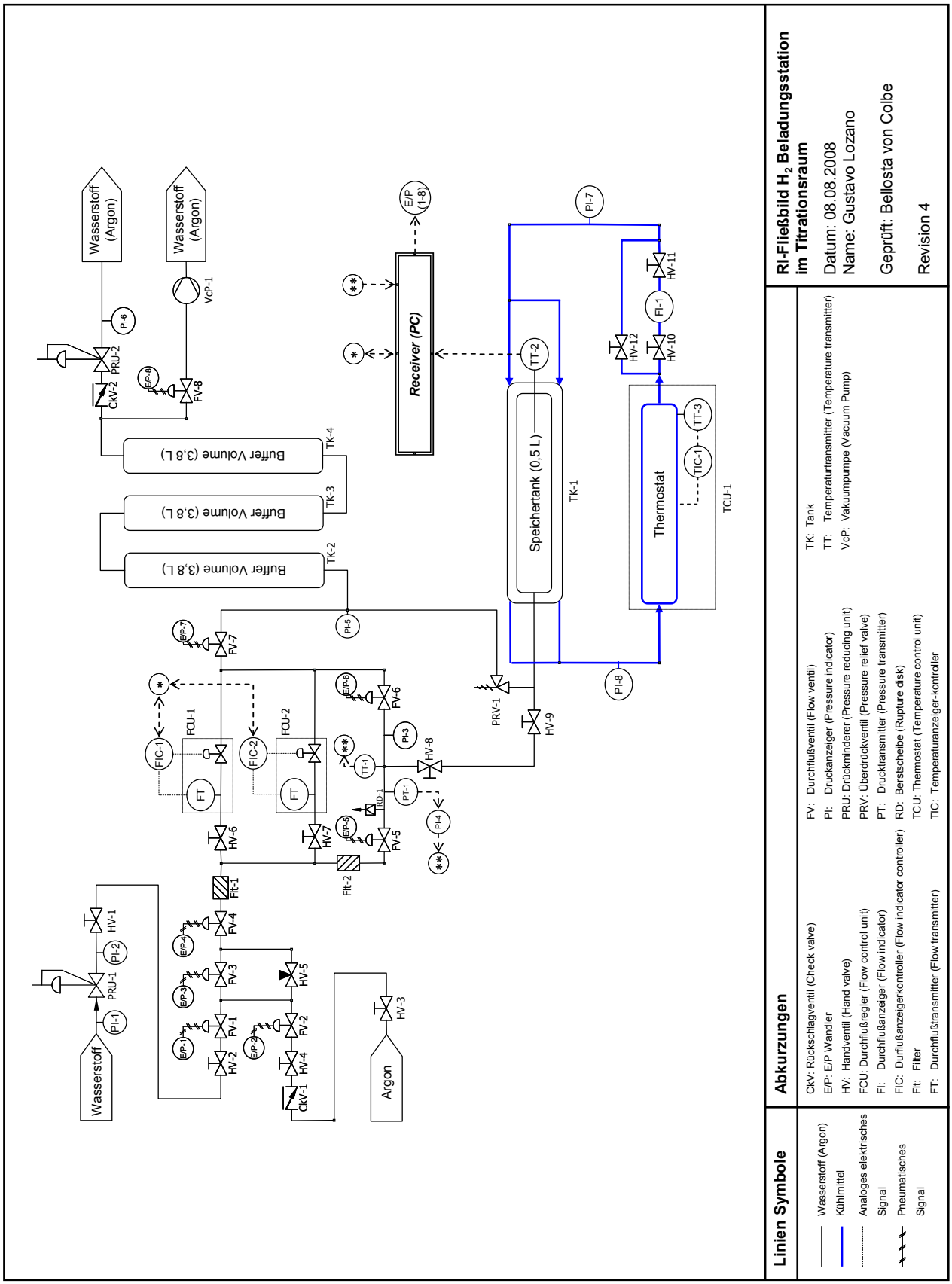

Figure 8.2: P&ID (piping and instrumentation diagram) of the hydrogen tank station.

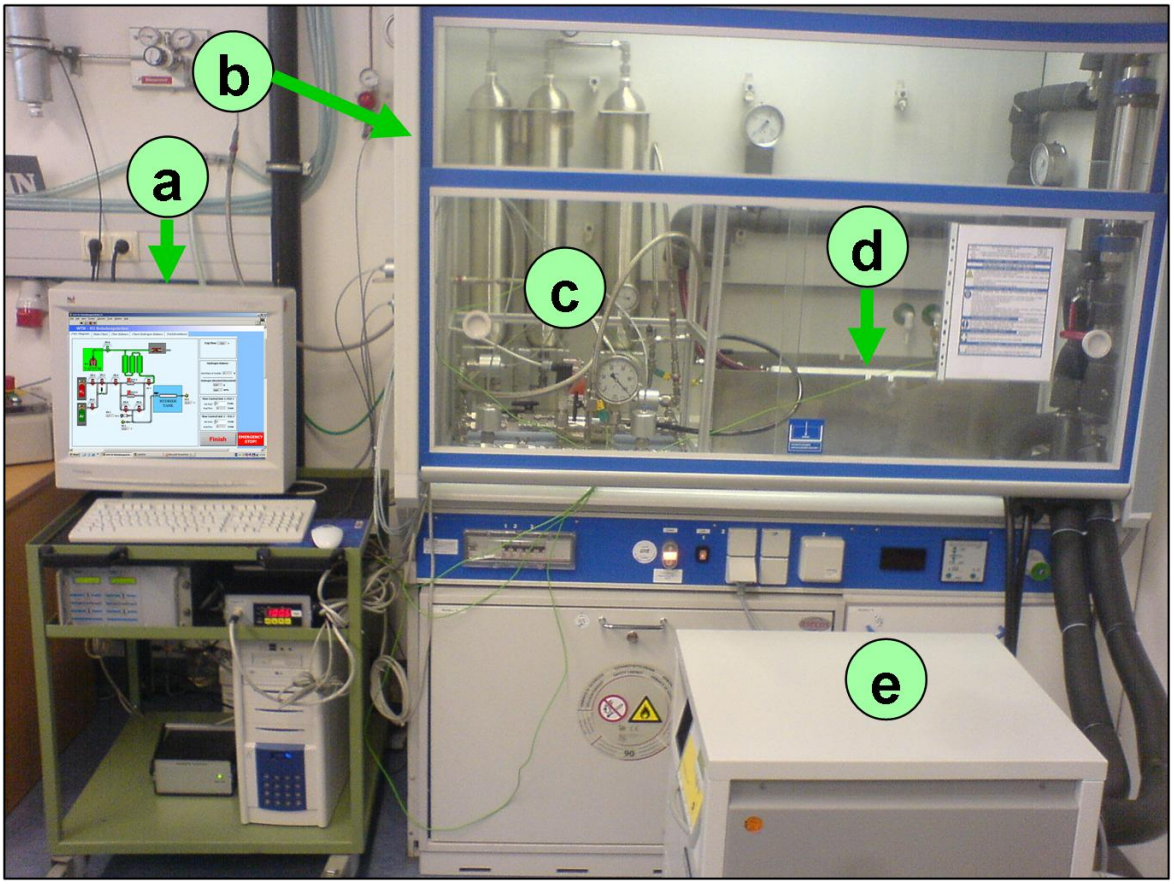

Figure 8.3: General view of the hydrogen tank station. Measurement, control, monitoring and regulation of the tank station were on-line performed by a computer-based application (a). For safety reasons the gas lines and accessories (c) as well as the storage tank (d) were placed inside a suction unit (b). A high temperature thermostat (e) pumped oil in an external circuit for heat management during the sorption measurements.

8.3 Error analysis for the estimation method of the effective thermal conductivity

The effective thermal conductivity of the hydride bed is estimated upon in-situ measurements in the thermocell (see subsection 3.1.3). The estimation is done using the following equation:

$$\lambda_{eff} = -\frac{\dot{q}\rho r^2}{4(T - T_c)} \tag{8.4}$$

Due to the propagation of error from the measured variables, the estimated thermal conductivity has an associated uncertainty. The propagated uncertainty (error) is calculated using the absolute error formula:

$$y = f(x_1, x_2, x_3, ...) \Rightarrow \Delta y = \left|\frac{\partial f}{\partial x_1}\Delta x_1\right| + \left|\frac{\partial f}{\partial x_2}\Delta x_2\right| + \left|\frac{\partial f}{\partial x_3}\Delta x_3\right| + ...$$

The formula is applied considering the errors due to the radius, the density of the hydride bed and that of the temperature measurements during the measurements:

$$\Delta\lambda_{eff} = \left|\frac{\dot{q}\rho r}{2(T - T_c)}\Delta r\right| + \left|\frac{\dot{q}r^2}{4(T - T_c)}\Delta\rho\right| + \left|\frac{\dot{q}\rho r^2}{4(T - T_c)^2}\Delta(T - T_c)\right| \tag{8.5}$$

The error of the radius comes from uncertainty of the position of the thermocouple inside the thermocell, around ±0.5 mm. The error of the bed density is around ±10 kg m^{-3}, based on several experimental measurements. The error in the temperature measurements is around ±0.12 K and the temperature difference ±0.25 K, based on the dispersion of experimental measurements.

The error of the estimation calculation depends on the experimental conditions. Direct inspection of Eq. 8.5 shows that the error depends strongly on the value of $(T - T_c)$. For instance, for small values of $(T - T_c)$, the error of the estimation method is extremely high, which is the case of hydride beds with high thermal conductivity.

9 Nomenclature

A	[s^{-1}]	pre-exponential factor of Arrhenius formula
c_1	[mm]	first additional thickness tolerance, see Eq. 5.1
c_2	[mm]	second additional thickness tolerance, see Eq. 5.1
c_p	[J kg^{-1} K^{-1}]	specific heat capacity at constant pressure
c_v	[J kg^{-1} K^{-1}]	specific heat capacity at constant volume
D_a	[mm]	external diameter of a tubular tank, see Eq. 5.1
D_i	[mm]	internal diameter of a tubular tank
E_a	[J mol^{-1}]	energy of activation
f	[-]	function of p and p_{eq} that acts as driving force for the hydrogen sorption reaction
g	[-]	function that defines the rate of reaction
k	[s^{-1}]	rate constant
K	[N mm^{-2}]	strength coefficient of the wall material, see Eq. 5.1.
L	[m]	characteristic length
ln	[l]	normal litre: a litre under normal conditions (1.01325 bar, 0 °C)
m	[kg]	mass
m	[K m^{-2}]	fitting coefficient for thermal conductivity estimations
$\dot{m}$	[kg s^{-1}]	mass flow
MW	[kg mol^{-1}]	molar mass
n	[m]	normal spatial vector
n	[-]	kinetic order of the JMA equation
p	[bar]	pressure
p_{eq}	[bar]	equilibrium pressure
p_{in}	[bar]	inlet pressure

Pe	[-]	Peclet number
$\dot{q}$	[W kg^{-1}]	heat generation per unit of mass
r	[m]	radius
r	[kg s^{-1}]	rate of reaction
r_{a1}	[kg s^{-1}]	net rate of the first absorption step
r_{a2}	[kg s^{-1}]	net rate of the second absorption step
r_{d1}	[kg s^{-1}]	net rate of the first desorption step
r_{d2}	[kg s^{-1}]	net rate of the second desorption step
r'	[kg m^{-3} s^{-1}]	hydrogen sorption rate per bulk volume of reacting material
r'_{a1}	[kg m^{-3} s^{-1}]	net rate of the first absorption step per bulk volume of reacting material
r'_{a2}	[kg m^{-3} s^{-1}]	net rate of the second absorption step per bulk volume of reacting material
r'_{d1}	[kg m^{-3} s^{-1}]	net rate of the first desorption step per bulk volume of reacting material
r'_{d2}	[kg m^{-3} s^{-1}]	net rate of the second desorption step per bulk volume of reacting material
r''	[mol H_2 kg^{-1} s^{-1}]	hydrogen sorption rate per mass of reacting material
R	8.314 [J mol^{-1} K^{-1}]	universal gas constant
R	[bar m^3 s kg^{-1}]	resistance to hydrogen sorption
s	[mm]	required wall thickness, see Eq. 5.1
S	[-]	design safety factor, see Eq. 5.1
S_I	[-]	mixture of 3 mol NaH, 3 mol Al, and 9/2 mol H_2
S_{II}	[-]	mixture of 1 mol Na_3AlH_6, 3 mol Al, and 3 mol H_2
S_{III}	[-]	3 mol $NaAlH_4$
SIM-1	[-]	simulation number 1 according to Table 4.6
SIM-2	[-]	simulation number 2 according to Table 4.6
SIM-3	[-]	simulation number 3 according to Table 4.6
t	[s]	time
T	[K]	temperature
T_C	[K]	temperature in the axis (centre) of a cylinder

T_{Opt}	[K]	optimal temperature
u	[m s^{-1}]	effective gas velocity
V	[m^3]	volume
w	[-]	mass of hydrogen per mass of material

Greek

α	[-]	transformed fraction
γ	[kg m^{-3}]	mass concentration
γ^0	[kg m^{-3}]	hydrogen-free mass concentration
ΔH_R	[J mol H_2^{-1}]	enthalpy of reaction per mol of hydrogen
ΔS_R	[J mol H_2^{-1} K^{-1}]	entropy of reaction per mol of hydrogen
ε	[-]	porosity of the hydride bed
κ	[m^2]	flow permeability of the hydride bed
λ	[W m^{-1} K^{-1}]	thermal conductivity
μ	[Pa s]	dynamic viscosity
ρ	[kg m^{-3}]	density
ρ^0	[kg m^{-3}]	hydrogen-free density
ρ_b	[kg m^{-3}]	bulk density (apparent density)
ρ_s	[kg m^{-3}]	solid density
υ	[-]	factor of the utilization of the allowable design stress, see Eq. 5.1

Subindixes

abs	absorption (hydrogenation)
b	hydride bed
des	desorption (dehydrogenation)
eff	effective
eq	thermodynamic equilibrium
g	gas phase

HT	heat transfer
$H_2 - T$	hydrogen transport
IK	intrinsic kinetics
min	minimum
max	maximum
s	solid phase
$sorp$	sorption (absorption and/or desorption)

Accents

$\bar{}$	mean value
$\dot{}$	change of a variable with respect to time
$\vec{}$	vector

Abbreviations

Ar	argon
CV	contracting volume model
CAD	computer aided design
EG	expanded graphite
H_2	molecular hydrogen
JMA	Johnson-Mehl-Avrami model
p-T	pressure-temperature
P&ID	piping and instrumentation diagram